QUANTUM MEASUREMENTS OF SPIN IN ALKALI ATOMS & BIO-MOLECULES

ARGYRIOS T. DELLIS

Dissertation Committee:

—————————————————————

Ioannis Kominis

—————————————————————

Dimitrios Charalambides

—————————————————————

Theodore Peter Rakitzis

University Of Crete, 2013

dedicated to Anna

ABSTRACT

This dissertation describes the results of the research work done by author at the Laboratory of Quantum Science and Technology.

In Part I we report on the experimental observation and theoretical justification of a novel effect, the transfer of spin noise from one atomic species to another, through the mechanism of spin exchange. Essentially, we extend the foundational studies of spin exchange into the deeper layer of quantum fluctuations. The signature of spin noise exchange is an increase of the total spin noise power at low magnetic fields where the two-species spin noise resonances overlap. We will demonstrate experimentally and prove theoretically that the total spin noise power of a two-species spin ensemble like ^{85}Rb - ^{87}Rb, exhibits a counter-intuitive dependence on the applied magnetic field. This is the experimental signature of spin noise exchange. This new effect is observable when the two atomic species have overlapping spin resonances.

Part II is about the dynamics of Radical Pair reactions. Radical Pair reactions were recently shown to represent a rich biophysical laboratory for the application of quantum measurement theory methods and concepts. We here propose a concrete experimental test that can clearly discriminate among the fundamental master equations currently attempting to describe the quantum dynamics of these reactions. The proposed measurement based on photon statistics of fluorescing radical pairs is shown to be molecular-model-independent and capable of elucidating the singlet–triplet decoherence inherent in the radical–ion-pair recombination process. Moreover, recent experiments have provided growing evidence for the Radical Pair magneto-reception mechanism, while recent theoretical advances have unraveled the quantum nature of Radical Pair reactions, which were shown to manifest a host of quantum-information-science concepts and effects, like quantum measurement, quantum jumps and the quantum Zeno effect. We here show that the quantum Zeno effect provides for the robustness of the avian compass mechanism, and immunizes its magnetic and angular sensitivity against the deleterious and molecule-specific exchange and dipolar interactions.

- Spin Noise Exchange in Coupled Alkali-Metal Vapors.
  A. T. Dellis, M. Loulakis and I. K. Kominis
  submitted (2013)

- Photon statistics as an experimental test discriminating between theories of spin-selective radical-ion-pair reactions.
  A. T. Dellis and I. K. Kominis
  Chem. Phys. Lett. 543, 170 (2012).

- The quantum Zeno effect immunizes the avian compass against the deleterious effects of exchange and dipolar interactions.
  A. T. Dellis and I. K. Kominis
  Biosystems 107, 153 (2012).

- Coherent Triplet Excitation Suppresses the Heading Error of the Avian Compass.
  G. E. Katsoprinakis, A. T. Dellis and I. K. Kominis
  New J. Phys. 12, 085016 (2010).

- Quantum random number generator based on spin noise.
  G. E. Katsoprinakis, M. Polis, A. Tavernarakis, A. T. Dellis, and I. K. Kominis
  Phys. Rev. A 77, 054101 (2008).

- Measurement of transverse spin-relaxation rates in a rubidium vapor by use of spin-noise spectroscopy.
  G. E. Katsoprinakis, A. T. Dellis and I. K. Kominis
  Phys. Rev. A 75, 042502 (2007).

Βρες χρόνο για δουλειά,
αυτό είναι το τίμημα της επιτυχίας.
Βρες χρόνο για σκέψη,
αυτό είναι η πηγή της δύναμης.

ΓΙΑΝΝΗΣ ΡΙΤΣΟΣ

ACKNOWLEDGMENTS

I would like to thank my supervisor Prof. Iannis Kominis. Our collaboration starts almost 10 years earlier when I started working with him as an undergraduate student and continued during my postgraduate studies in the Physics Department of the University of Crete. At that time despite the difficulties, we achived to build the first Magneto-Optical trap in Greece. Iannis' endless passion for studying Physics was stimulating for me and was the driving force in the Lab. I am grateful to his constant availability for discussions from which I gained a deeper understanding for the underlying physics. I cannot resist in mentioning his patience in my training and his efforts to encourage me at tough times. Once more I would like to thank Iannis for his help, guidance and supporting me by all means all these years. Without any doubt he is the person that influenced more than any other my development as a scientist and probably my future career.

Special thanks to my parents and sister for their unwavering belief to me. All these years my parents have devoted themselves to us and is beyond any doubt that without their help and support I would not have been able to accomplish my studies.

Finally, I am grateful to Anna. She is the person that was always there for me, supporting and encouraging me every single day.

CONTENTS

LIST OF FIGURES

NOMENCLATURE

A   Acceptor

D   Donor

ECDL   Extended Cavity diode Laser.

ISNP   Integrated Spin Noise Power

ME   Master Equation

MFE   Magnetic Field Effect

QE   Quantum Efficiency

QMME   Quantum Mechanical Master Equation

RP   Radical Pair

RPM   Radical Pair Mechanism

SNR   Signal to Noise Ratio

TME   Traditional Master Equation

Part I

SPIN NOISE

INTRODUCTION

Quantum noise in atomic systems is usually considered to pose an unavoidable fundamental limitation to the achievable measurement precision, leading to the so-called standard quantum limits. Spin noise, in particular, limits the attainable precision of measurements involving an ensemble of uncorrelated paramagnetic atoms as well as other two-level systems employed, for example, in atomic clocks. Furthermore, the understanding of spin noise of uncorrelated atomic ensembles is crucial for the realization of methods aimed at producing spin squeezing. For these reasons it appears essential to directly study spin noise and its various manifestations. However, contrary to what is commonly believed, not all noise signals are undesirable at experimental measurements. Spin noise is one of such signal. It refers to the spontaneous fluctuations on the mean value of the total spin of a system. Every spin system consists of a finite number of particles which are prone to interactions with the environment, no matter how well the system is prepared or isolated. It is thus expected that the magnetisation of such a system will exhibit random changes. Spin noise spectroscopy exploits these spontaneous fluctuations and relates them to the dynamics of the system under study. Nowadays spin noise is a well established spectroscopic tool and gains popularity as a method to acquire information for complex systems such as atomic gases and semiconductors. Historically the first reference on spin noise is in the famous paper of F. Bloch "Nuclear Induction"[5], where it was mentioned that, the inductive signal on a probe coil, from N nuclear spins in the absence of any orientation should be proportional to $\sqrt{N}$ due to incomplete cancellation, of statistical origin. The detection of nuclear spin noise was made in the middle 80s by Sleator et.al[50] at ^{4}He temperatures by detecting nuclear quadrupole resonance noise spectrum of a sample with a dc SQUID. Moreover nuclear spin noise imaging was demonstrated by Muller et.al[40].

Methods for detecting the magnetisation of a system were known since the middle of last century and were based on the interaction of a light beam with the spins of the system and the fact that the properties of light, such as the intensity and the polarization, are affected by the properties of the medium under study. The Faraday and the Voigt effect are still widely used for the detection of atomic magnetization. In the case of Faraday detection technique, the polarization plane of a linearly polarized light is rotated after interacting with a paramagnetic medium. The magnitude of rotation angle reveals information about the medium. In order to detect spontaneous fluctuations of the magnetization and thus for spin noise to reveal itself, all the other noise signals should be eliminated or at least should be of much smaller magnitude. This was the main obstacle that delayed the experimental observation of spin noise signals about 30 years since the first mention of Bloch. The advent of lasers and the the further development of noise limited polarimetric techniques, such as photon shot noise limited polarimeters and the production of sensitive and accurate detection systems made it possible to detect the first spin noise signals by Zapasskii[62] in the 70's. Although the experimental demonstration of spin spontaneous fluctuations, the field of spin noise spectroscopy remained practically inactive until the beginning of this century. Crooker[8] exploited the spin noise of N paramagnetic spins at thermal equilibrium in order to perform perturbation free magnetic resonance on samples of alkali-metal vapours. Since then, spin noise as a tool to reveal spectroscopic information in a non destructive way, has been frequently used [28, 63]. More recently spin noise spectroscopy was fruitfully applied to solid state systems[39]. In particular the authors of this work managed to measure the g-factor and the relaxation in n-GaAs, altought the signal to noise ratio was very small and the data accumulation time was several hours.

The spin-exchange interactions, are central to optical pumping of atomic vapors. Interestingly, even without externally manipulating atoms with light, incessant atomic collisions drive atomic spin interactions through H_{se}. These collisions act as minute quantum measurements, continuously redistributing the collective atomic spin along a given direction around the average value of zero. The frequency spectrum of such spontaneous spin fluctuations, also called *spin noise*, is centered around $f = 0$ and has a width on the order of the inverse of the spin coherence lifetime. The application of a static magnetic field shifts the spin noise spectrum to the respective Larmor frequency, rendering it easily observable amidst other noise sources. Ordinarily it would be expected that the total spin noise power would be a constant , irrespective of the magnetic field at which the measurement is performed, that is, irrespective on where along the frequency axis are the two spin resonances positioned. We are here going to show that this is not the case. We will demonstrate experimentally and prove theoretically that the total spin noise power of a two-species spin ensemble, like ^{85}Rb and ^{87}Rb, exhibits a counter-intuitive dependence on the applied magnetic field. This is the experimental signature of spin noise exchange. This new effect is observable when the two atomic species have overlapping spin resonances

BACKGROUND THEORY

2.1 INTRODUCTION

Alkali atoms are used in a wide range of experiments, especially in atomic physics. They are a convenient choice because:

- Their wavelength is in the near infrared or visible and is compatible with the emission spectrum of inexpensive commercial powerful diode lasers

- Their electronic structure is quite simple and theoretical models can be used to support experimental results. More specific alkali atoms can be described as having one unpaired electron. Their ground state has no orbital angular momentum (L = 0), whereas the first two excited states have L = 1.

- The properties of all the alkali-metal atoms have been extensively studied and the values of parameters such as lifetimes and oscillator strengths are known with great accuracy.

- The density of the vapors can be easily controlled with simple equipments.

In this chapter we will briefly discuss some properties of the alkali-metal atoms, especially of Rubidium, which are going to be used in this thesis.

2.2 ATOMIC ENERGY LEVELS

The ground electronic state of Rubidium, as a typical alkali-metal atom, is $^2S_{1/2}$ i.e has no orbital angular momentum. The lowest excited energy state has unit orbital angular momentum. Due to the spin-orbit interaction ($\mathbf{H} = \mathbf{L} \cdot \mathbf{S}$) this energy state is split into two different states. The state with the lowest energy has total angular momentum $J = 1/2$ and the other state has $J = 3/2$. All the isotopes of the alkali-metal atoms have non-zero nuclear spins. In the case of Rubidium the two dominant isotopes in nature ^{85}Rb and ^{87}Rb have nuclear spins 5/2 and 3/2. respectively. The coupling of the total angular momentum ($\mathbf{J}$) with the nuclear spin ($\mathbf{I}$) described by the Hamiltonian $\mathbf{H_{hfs}} = \mathbf{A_{hf}} \cdot \mathbf{I} \cdot \mathbf{J}$[1] results in a further split of the energy levels, the hyperfine structure. These splittings have been measured with tremendous precision[2]. The energy level structure of Rubidium is shown in Fig.A.1.1

2.3 EVOLUTION IN A MAGNETIC FIELD

The the evolution of the alkali-metal atom is described by the master equation (with $\hbar = 1$):

$$\frac{d\rho}{dt} = -\imath\left[H,\rho\right] \tag{1}$$

where H is the Hamiltonian of describing the interactions of the atoms with the surrounding system and the applied electromagnetic fields.

---

[1] A_{hf} is the hyperfine interaction tensor
[2] the ground state hyperfine energy split of ^{133}Cs is used in atomic clocks as the international frequency standard[43]

2.3.1 *Hamiltonian*

2.3.1.1 *Hyperfine interaction*

All the isotopes of the alkali-metal atoms have non zero nuclear spin. The hyperfine structure is the result of the interaction of the dipole and quadrapole moment of the nucleus with the orbital motion and the electric field gradients in the distribution of the electronic charge respectively. The Hamiltonian describing the hyperfine interaction for the ground state (L = 0) of the atom is:

$$H_{hfs} = A^{\{g\}} \mathbf{I} \cdot \mathbf{S} \tag{2}$$

while for the excited states (L = 1) is:

$$
\begin{aligned}
H_{hfs} &= A^{\{e\}} \mathbf{I} \cdot \mathbf{S} + \\
&+ B^{\{e\}} \frac{3(\mathbf{I} \cdot \mathbf{J})^2 + (3/2)(\mathbf{I} \cdot \mathbf{J}) - I(I+1)J(J+1)}{2I(2I-1)(2J-1)}
\end{aligned}
\tag{3}
$$

$A^{\{g\}}$ and $A^{\{e\}}$ are the coupling coefficients for the magnetic dipole interaction for the ground and the excited states respectively and $B^{\{e\}}$ is the magnetic quadrapole coupling coefficient.

2.3.1.2 *External magnetic fields*

In the classical case, the interaction between a magnetic field and a charged particle of angular momentum $\mathbf{L}$ is given by:

$$H_B = -\mu_L \cdot \mathbf{B} \tag{4}$$

where $\mu_L = q/(2mc)\mathbf{L}$ is the magnetic dipole moment. Generalizing the above in the quantum mechanical case the magnetic dipole moment of the total electronic angular momentum (J = L + S) is given by:

$$\mu_J = g_J \frac{q}{(2mc)} \mathbf{J} \quad \left(g_J = 1 + \frac{J(J+1) + S(S+1) + L(L+1)}{2J(J+1)}\right) \tag{5}$$

and the magnetic dipole moment of the total angular momentum ($\mathbf{F} = \mathbf{J} + \mathbf{I}$) of the atom is given by:

$$\mu_F = g_F \frac{q}{(2mc)} \mathbf{F} \quad \left(g_F = g_J \frac{F(F+1) + J(J+1) + I(I+1)}{2F(F+1)}\right) \tag{6}$$

When the applied magnetic field it relatively low compared to the hyperfine energy splitting and F is a good quantum number the energy scales linearly with the magnetic field and Eq.4 we can be written in the form:

$$H_B = \gamma \hbar m_F |\mathbf{B}| \quad \left(\gamma = (g_F \frac{\mu_B}{\hbar})/\hbar\right) \tag{7}$$

For the case of ^{87}Rb and F = 2, $\gamma = 0.701\,\mathrm{MHz/G}$ and for ^{85}Rb and F=3, $\gamma = 0.466\,\mathrm{MHz/G}$. When the magnetic field is large enough compared to the hyperfine splitting and F ceases to be a good quantum number the energy of the levels is given by the Breit-Rabi[7]:

$$
\begin{aligned}
E_{|J=1/2,m_J;I,m_I\rangle} &= \frac{\Delta E_{hfs}}{2(2I+1)} \\
&+ g_I \mu_B (m_I \pm 1/2) B \\
&\pm \frac{\Delta E_{hfs}}{2} \left(1 + \frac{4(m_I \pm 1/2)}{2I+1} \frac{(g_J - g_I)\mu_B B}{\Delta_{hfs}} + \left(\frac{(g_J - g_I)\mu_B B}{\Delta_{hfs}}\right)^2\right)^2
\end{aligned}
\tag{8}
$$

where Δ_{hfs} is the hyperfine splitting

The polarization of an atomic ensemble can be changed by various mechanisms. These relaxation mechanisms affect the mean value of the angular momentum along the quantization axis[3] (diagonal elements of the density matrix) and the coherences between states (non diagonal elements of the density matrix). The rate at which the mean value of the angular momentum approaches a steady state value is known as T_1^{-1} and the rate at which coherences between states vanish is known as T_2^{-1}. The most important relaxation mechanisms going to be described in the rest of this section.

T_2^{-1} is the rate at which coherences decay. T_1^{-1} is the rate at which population decay

2.4.1 Diffusional Motion

The evolution of the density matrix will not only be time dependent but in general will depend on the location. In this general situation another term, describing the diffusional motion should be added in the master equation describing the evolution of the density matrix:

$$(\frac{d\rho}{dt})_{DM} = D\nabla^2\rho \tag{9}$$

where D is the diffusion constant, which depends on the pressure and temperature of the specific buffer-gas. The diffusion constant is related to the mean free path (λ_f) and the mean atomic velocity ($\bar{u}$) via $D = \lambda_f \bar{u}/3$, but in practice it is experimentally determined and expressed relatively to the 760Torr pressure at 0°C

$$D = D_0 \frac{760}{P} \left(\frac{T}{T_o}\right)^{3/2} \quad \text{(units of P: Torr, } T_o=424K\text{)} \tag{10}$$

N$_2$	He	Ne
0.33	0.54	0.31

Table 1: Diffusion Constants for Rb[20]. D_0 is expressed in cm^2sec^{-2}

2.4.1.1 Wall relaxation

When an atom hits the wall of the cell it is absorbed by the wall material and after some time it escapes back to the vapor. During the time is absorbed, the atoms interact with the environment of the wall and its polarization may change. The solution of the diffusion equation (Eq.9) will give the diffusional damping rate which depends on the cell geometry through the boundary conditions used to solve Eq.9. Usually the cells used in this kind of experiments are cylindrical or spherical:

Collisions of the atoms with the containers walls result in depolarization.

$$(T_d)^{-1} = \left(\frac{\pi^2}{l^2} + \frac{2.405^2}{r^2}\right) D \quad \text{(cylindrical cell of radius r andlength l)} \tag{11}$$

$$(T_d)^{-1} = \left(\frac{\pi^2}{r^2}\right) D \quad \text{(spherical cell of radius r)} \tag{12}$$

2.4.1.2 Transit time relaxation

A similar relaxation mechanism exists if the diameter of the laser beam used to probe the polarization of the atoms is smaller compared to the dimensions of the cell. The process at which a polarized atom, initially inside the the volume defined by the probe beam, diffuses to the not illuminated area is equal to lossing polarization. The

The process at which a polarized atoms, initially inside the the volume defined by the probe beam, diffuses to the not illuminated area is equal to depolarization.

---

[3] The quantization axis usually lies along the direction of the applied magnetic field.

rate of polarization loss due to the transition of the atom to the non-illuminated area is described by[22]:

$$(T_{tr})^{-1} = \left(\frac{2.405^2}{r^2}\right) D \left(\frac{1}{1 + K/p}\right) \qquad (13)$$

p is the pressure of the buffer-gas and K is the Knudsen coefficient defined as $K = c\lambda_f p/r$. Here c is a constant, λ_f is the mean free path and r is the radius of the laser beam.

2.4.1.3

2.4.2 *Spin Destruction Collisions*

Spin destruction collision between alkali atoms bo not preserve the electronic spin

Another very important mechanism responsible for spin relaxation originates from the collisions between alkali atoms of the same or different isotopic weight, or between alkali atoms and much heavier noble gas atoms. In general the relaxation rate due to spin destruction is given by:

$$(T_{sd})^{-1} = n\sigma\overline{u} \qquad (14)$$

where n is the density of the perturbing gas, σ is the collisional cross section and $\overline{u}$ is the relative thermal velocity[4]

2.4.2.1 *Alkali-Alkali collisions*
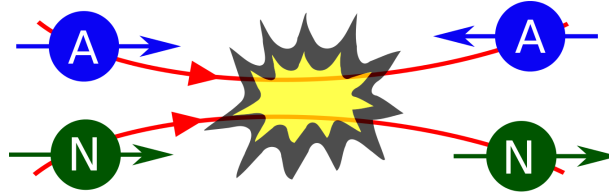
Figure 2.4.1: Spin-destruction collisions between an alkali atom and a noble gas atom. The same picture is valid for alkali-alkali collisions.

Spin destruction collision between alkali atoms do not preserve the electronic spin and can be described by an interaction of the form[5] (Fig. 2.4.1):

$$A_1 (\uparrow) + A_2 (\uparrow) \longrightarrow A_1 (\uparrow) + A_2 (\downarrow) \qquad (15)$$
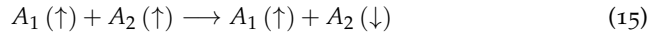
The spin destruction collisional cross section for Rubidium atoms is $\sigma_{SD}^{self} = 1.6 \times 10^{-17} cm^2$

2.4.2.2

2.4.3 *Spin-Ecxhange collisions*

When two atoms collide spin polarizations of one may be transfered to the other. At this type of collisions the total spin angular momentum is conserved.

Contrary to the spin-destruction collisions which do not preserve the total spin angular momentum, a different mechanism for polarization relaxation occurs when two atoms collide and spin polarizations of one is transfered to the other (Fig.2.4.2). At this type of collisions the total spin angular momentum is conserved. As mentioned for the case of spin-destruction collisions the alkali-atoms may collide with atoms of the same or different isotopic weight or with noble gas atoms.

---

4 $\overline{u} = \sqrt{\frac{8k_B T}{\pi M}}$, with $M^{-1} = m_1^{-1} + m_2^{-1}$

5 The angular momentum is transfered to the rotational angular momentum of the colliding alkali atoms and is believed to stem from the spin-axis interaction of the form [?]: $V = \frac{2}{3}\lambda\mathbf{S} \cdot \left(3\widehat{\mathbf{R}}\widehat{\mathbf{R}} - \mathbf{1}\right) \cdot \mathbf{S}$
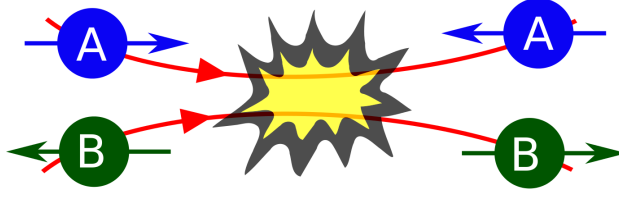
Figure 2.4.2: Spin-exchange collisions between two atoms. The total electronic spin is conserved.

2.4.3.1 *Alkali-Alkali Spin Exchange collisions:*

When the two alkali atoms collide a dimmer molecule is formed. The spin state of this new molecule may be in a singlet state[6] or in a triplet state[7]. The large splitting of the singlet and triplet potential causes the atoms to rotate about each other many times during the collision [57], but since the spin exchange interaction $V_{SE} = \eta \mathbf{S_1} \cdot \mathbf{S_2}$ commutes with the total spin $\mathbf{S} = \mathbf{S_1} + \mathbf{S_2}$, the total spin angular momentum is preserved. To sum up, the effect of spin exchange collisions is the redistribution of the total angular momentum between the ground state sub-levels (Fig.2.4.3). It has been shown [15] that the rate of spin polarization transfer due to spin exchange from alkali-atoms of species i to alkali atoms of species j is given by:

$$(T_{ex,ij})^{-1} = \left[A_j\right] \sigma_{SE} \bar{u} \tag{16}$$

where $\left[A_j\right]$ is the number density of the perturbing gas, σ_{SE} is the spin exchange cross section and $\bar{u}$ is the relative thermal velocity.
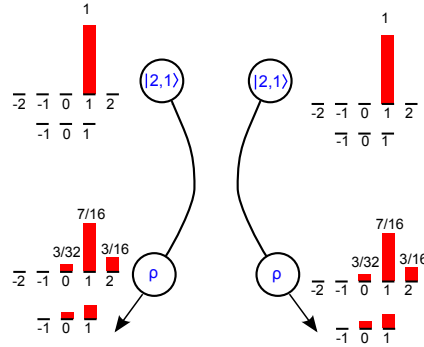
Figure 2.4.3: Alkali-Alkali spin exchange collision. Although the population of the ground state sub-levels is redistributed after collision, the spin angular momentum is conserved. (figure reproduced from [57]).

2.4.4 *Total Relaxation Rate*

In the experiment that will be described later, the goal is to measure the spin noise transfer from one kind of rubidium atoms to the other, due to spin exchange collisions. In order to achieve this, an essential step is to minimize the contribution of all the other mechanisms to the total relaxation rate. The total rate is

$$(T_{tot})^{-1} = (T_{SE})^{-1} + (T_{SD})^{-1} + (T_{tr})^{-1} \tag{17}$$

- The spin exchange relaxation rate is given by Eq.16. It depends on the spin exchange cross section. For Rubidium atoms the cross section is $\sigma_{SE}^{self} = 2 \times$

---

6 the spins of the two atoms are anti-parallel ($S_{total} = 0$)

7 the spins of the two atoms are parallel ($S_{total} = 0$)

10^{-14}cm^2. At temperature of interested, i.e T = 110°C, the spin exchange relaxation rate is $(T_{SE})^{-1} = 1.2$kHz.

- The transit time broadening can be estimated from Eq.13. In our case for a cylindrical cell of length 10cm and an elliptical probe beam of mean radius $\sqrt{r_1 r_2} = 0.15$ cm the transit time broadening was faound to be $(T_{tr})^{-1} \approx 80$Hz.

- The relaxation rate due to spin destruction collisions depends on the collisional cross section. For Rubidium atoms alkali-alkali cross section $\sigma_{SD}^{self} = 1 \times 10^{-17}$cm^2 and for Rubidium-N$_2$ collisions the cross section is $\sigma_{SD,N_2} = 1 \times 10^{-22}$cm^2. Due to the fact that the spin destruction cross sections are much smaller than the spin exchange cross section, the contribution of spin destruction to the total relaxation rate can be safely omitted.

Taking into account that all the other relaxation rates are much smaller than the spin exchange rate, the total relaxation rate can be approached to be equal to the spin exchange rate

$$(T_{tot})^{-1} \simeq (T_{SE})^{-1} \qquad (18)$$

Depolarization may be caused by the absorption of a photon which interrupts the coherent evolution

There exist an other source of relaxation caused by the absorption of a photon by an atom. In this way the coherent evolution of the atom is interrupted, resulting in the broadening of the spin resonance signal. To verify that this mechanism is negligible we did the following measurement. The width of the spin noise resonance was measured for several laser powers. If the contribution of optical absorption to the overall relaxation rate is significant then the width of the spin resonance should scale proportional to the laser power. By extrapolating the results to zero laser power we can estimate the spin exchange relaxation rate

Figure 2.4.4: Measured spin-noise resonance full widths (FWHM) versus probe laser power. The measurement was performed at 112°C and the spin noise resonance of ^{85}Rb was set to 22kHz.

According to this measurement the relaxation rate due to photon absorption was about 46 Hz/mW and the spin exchange relaxation rate was found to be 1.07kHz very close to the theoretical prediction.

THEORY OF SPIN NOISE

The evolution of the ground state of the alkali atoms is generally described by the a Liouville equation of the form:

$$\frac{d\rho}{dt} = -i\left[H,\rho\right] + \mathfrak{L}\left[\rho\right] \tag{19}$$

where H is the Hamiltonian unitary operator and the part $\mathfrak{L}\left[\rho\right]$ accounts for all the other physical mechanism such as atomic collisions and loss mechanisms. The complete form of the last part of Eq.19 is complicated and difficult to solve analyticaly, for the interested reader the full form can be found in[2]. The complete dynamics of the atomic ground state evolution can be described in a simplified way. As Bloch suggested[5], it is enough to remember that the expectation value of any operator evolves in time in exactly the same way as a classical quantity. Moreover the magnetization (**P**) of an ensemble of spins subjected in a magnetic field (**B**) precesses around the axis of the applied magnetic field. The precessive motion is described by:

the magnetization of an ensemble of spins subjected in a magnetic field precesses around the axis of the applied magnetic field

$$\frac{d\boldsymbol{P}}{dt} = \mathrm{g}\left(\boldsymbol{P} \times \boldsymbol{B}\right) \tag{20}$$

in order to take into account the relaxation mechanisms (described by the rates $(\mathrm{T}_1)^{-1}$ and $(\mathrm{T}_2)^{-1}$) Bloch added the terms $-\boldsymbol{P}_t(\mathrm{T}_2)^{-1}$ and $-\boldsymbol{P}_p(\mathrm{T}_1)^{-1}$ to Eq.20[1]. Thus the complete formula describing the time evolution of the ground state magnetization is

$$\frac{d\boldsymbol{P}}{dt} = \mathrm{g}\left(\boldsymbol{P} \times \boldsymbol{B}\right) - (T_2)^{-1}\boldsymbol{P}_t - (T_1)^{-1}\boldsymbol{P}_p \tag{21}$$

3.1 FLUCTUATION AND DISSIPATION

The fluctuation - dissipation theorem states that the decay of a system in thermodynamic equilibrium is related to the statistical fluctuations of the system. As already has been mentioned the atoms inside the cell are performing a diffusive motion. The result of this motion is the continuous collisions between atoms of the same or different species and with the walls of the container. These collisions result in the redistribution of the collective atomic spins and thus to loss of magnetization. A widely common example of the fluctuation - dissipation theorem is the Brownian motion of particles described by Einstein. In this study, Einstein (and o few years later Langevin) suggested that the viscous drag and the velocity fluctuations are complementary effects originating from the collisions of the Brownian particle with the molecules of the fluid

In the case of the alkali atoms studied here, the complete equation describing the evolution of the atomic magnetization should also take into account the collisions between particles which are manifested as random fluctuations of the system's polarization. This equation is given if we write the Bloch equations in Ito's[13] form:

$$\frac{d\boldsymbol{P}}{dt} = -D\boldsymbol{P}dt + dF \tag{22}$$

where D is an operator that accounts for the unitary evolution and for the losses of the system, and dF describes the spontaneous fluctuations.

---

1 if a process generating polarisation along the $\hat{\boldsymbol{p}}$ direction at rate R_p exists the term $\mathrm{R}_\mathrm{p}\hat{\boldsymbol{p}}$ should be added.

In order to proceed to a theoretical analysis of the system under study, it is essential once more to remind some experimental details.

- First of all the systems under study constituted of either one cell containing both Rubidium isotopes, or two cells back to back each containing one of the two isotopes.

- The system was heated to 110°C

- All the cells were containing Nitrogen as buffer - gas.

- The sample is unpolarized, i.e $\langle P \rangle = 0$

- The samples are placed inside a homogeneous magnetic field pointing at the z-axis, which in perpendicular to the direction of propagation of the light

- The detected signal from the optical polarimeter depends on the transverse components of the polarization, i.e on P_x and P_y

The final form of the equation describing the dynamics of the atomic magnetization is:

$$
\begin{aligned}
dP^A &= g_A(P^A \times B)dt - (\frac{1}{T_2^A} + \frac{1}{T_{se}^{AB}})P_t^A dt - \frac{1}{T_1^A}P_p^A dt \\
&+ \frac{1}{T_{se}^{AB}}P^B dt + d\xi_1
\end{aligned}
\tag{23}
$$

$$
\begin{aligned}
dP^B &= g_B(P^B \times B)dt - (\frac{1}{T_2^B} + \frac{1}{T_{se}^{BA}})P_t^B dt - \frac{1}{T_1^A}P_p^B dt \\
&+ \frac{1}{T_{se}^{BA}}P^A dt + d\xi_2
\end{aligned}
\tag{24}
$$

where the indexes A and B refer to the ^{87}Rb and ^{85}Rb respectively. It should be noted that the above system of differential equations contains six unknown parameters $\{P_x^A, P_y^A, P_z^A\}$ and $\{P_x^B, P_y^B, P_z^B\}$. A major simplification is made if we notice that for the specific experimental configuration, in which the magnetic field is vertical to the laser beam, the evolution of the magnetization component parallel to the magnetic field is completely independent of the evolution of the transverse magnetization. Moreover the detected signal depends only to the transverse component. The evolution of the transverse component is given by:

$$
\begin{aligned}
dP_t^A &= g_A(P_t^A \times B)dt - (\frac{1}{T_2^A} + \frac{1}{T_{se}^{AB}})P_t^A dt \\
&+ \frac{1}{T_{se}^{AB}}P_t^B dt + d\xi_1
\end{aligned}
\tag{25}
$$

$$
\begin{aligned}
dP_t^B &= g_B(P_t^B \times B)dt - (\frac{1}{T_2^B} + \frac{1}{T_{se}^{BA}})P_t^B dt \\
&+ \frac{1}{T_{se}^{BA}}P_t^B dt + d\xi_2
\end{aligned}
$$

The rate at which spin polarization is transferred from atom of species A to species B is denoted by $(T_{se}^{AB})^{-1} = \sigma_{SE}^{self}\bar{u}n_B$, and all the other rates of polarization loss for species A are denoted by $(T_2^A)^{-1}$. In general $(T_2^A)^{-1}$ is sum of contributions of:

1. spin exchange collisions between alkali atoms of the same species

2. spin exchange collisions between alkali atoms and noble gas atoms

3. spin destruction collisions between alkali-alkali atoms and alkali-noble gas atoms
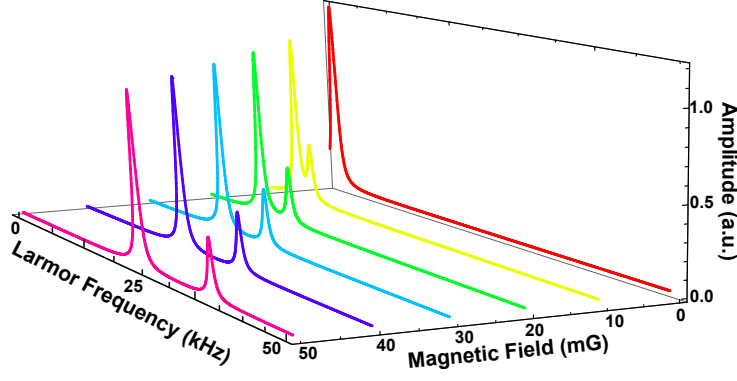
Figure 3.2.1: Power Spectral Density of Spin Noise. Eq.30 is plotted for magnetic fields ranging from dc to 50 mG.

The spin destruction cross section between Rubidium atoms is $\sigma_{SE}^{self} = 2 \times 10^{-14}\,\mathrm{cm}^{-2}$, while the spin destruction cross sections between Rb atoms and between $\mathrm{Rb} - \mathrm{N_2}$ is $\sigma_{SD}^{self} = 1 \times 10^{-17}\,\mathrm{cm}^{-2}$ and $\sigma_{SD,N_2}^{self} = 1 \times 10^{-23}\,\mathrm{cm}^{-2}$ respectively. It thus reasonable to exclude all the other relaxation rates from $(T_2^A)^{-1}$ rather than spin exchange $(T_2^A)^{-1} = \sigma_{SE}^{self}\bar{u}n_A$. It is convenient to introduce the the 2-element column vector $\boldsymbol{P} = \{P_A, P_B\}^T$ with $P_i = P_{i,x} + iP_{i,y}$ in order to simplify the system of differential equations Eq.25.

spin exchange rate is the dominant relaxation mechanism

$$dP = -APdt + \Xi dW \qquad (26)$$

where the decay matrix $\boldsymbol{A}$ is:

$$A = \begin{pmatrix} \Gamma + i\omega_1 & \gamma_{SE}^{AB} \\ \gamma_{SE}^{BA} & \Gamma + i\omega_2 \end{pmatrix} \qquad (27)$$

Ξ is a diagonal matrix representing the fluctuations of the system

$$\Xi = \begin{pmatrix} \sqrt{\Gamma/N_1} & 0 \\ 0 & \sqrt{\Gamma/N_2} \end{pmatrix} \qquad (28)$$

with being N_j is the total number of atoms probed by the laser beam. The vector $dW = \{dW_1, dW_2\}^T$ describes two independent Wiener processes with zero mean and variance dt. The power spectrum of the magnetization is given by[14]:

$$\boldsymbol{P_{PSD}}(\omega) = \frac{1}{2\pi}(A - i\omega)^{-1} \cdot \Xi \cdot \Xi^T \cdot (A^\dagger + i\omega)^{-1} \qquad (29)$$

The expectation value of spins equals the atomic number density times the expectation value of polarisation, the spin noise power spectrum is given by:

$$\begin{aligned} S(\omega) \quad = \quad & n_A^2 \left([\boldsymbol{P_{PSD}}(\omega)]_{11} + [\boldsymbol{P_{PSD}}(-\omega)]_{11}\right) \\ + \quad & n_B^2 \left([\boldsymbol{P_{PSD}}(\omega)]_{22} + [\boldsymbol{P_{PSD}}(\text{-}\omega)]_{22}\right) \quad \text{\small (units: 1/Hz)} \end{aligned} \qquad (30)$$

where $[\boldsymbol{P_{PSD}}(\omega)]_{jj}$ is the diagonal element of the matrix $\boldsymbol{P_{PSD}}(\omega)$ given by Eq.29. In Eq.30 we have also taken into account that when measuring the power spectrum of a signal in an instrument like a FFT spectrum analyzer, the signal at negative frequencies is mirrored at the positive frequencies The total spin noise power under the curve given by Eq.30 is given by the integral

$$SNP = \int_0^\infty S(\omega)d\omega \qquad (31)$$

the dependance of the Spin Noise Power for applied magnetic fields ranging from 0 to 50mG is shown in Fig.3.2.2 The total area under the spin noise power spectral
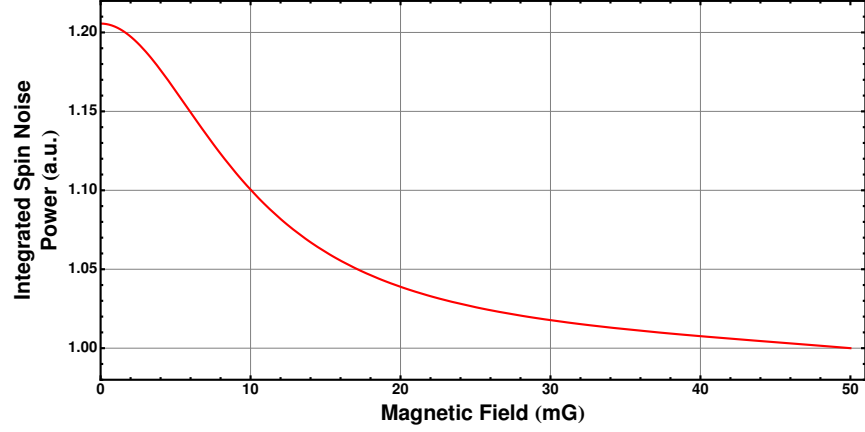
Figure 3.2.2: Dependence of the Integrated Spin Noise Power (Eq.31) from the applied magnetic field. The externally aplied magnetic field is up to 50mG. For the simulation the temperature of the cell was taken to be 115°C, the length of the cell 10cm, the cross section of the probe beam was $(1.15 \times 1.8)\text{mm}^2$ and the pressure of N_2 buffer gas was 100Torr .

One would expect that ISNP woulf remain constant when the magnetic field is changed

distribution, i.e the Integrated Spin Noise Power (ISNP) is the total spin variance. Ordinarily it would be expected that this would be a constant, irrespective of the magnetic field at which the measurement is performed, that is, irrespective on where along the frequency axis are the two spin resonances positioned. In Fig.3.2.2 we show that this is not the case. The fluctuation of the atomic polarization are measured by a balanced polarimeter. The signal at the output of the balanced polarimeter is given by

$$(\delta u_{ASN})^2 = (2GP)^2 (\delta\phi_{ASN})^2 \quad \text{(units: V}^2_{\text{rms}}\text{/Hz)} \tag{32}$$

where $(\delta\phi_{ASN})^2$ is the power spectrum of the rotation angle fluctuations given by

$$(\delta\phi_{ASN})^2 = (\theta_1)^2 S(\omega) \quad \text{(units: rad}^2\text{/Hz)} \tag{33}$$

with θ_1 being the Faraday rotation per atom given by Eq.41.

3.3 EXPLANATION OF THE EFFECT

The physical origin of the observed effect is this: the fluctuation term in the polarization of each atom (last term in Eqs.25) has a band-limited frequency spectrum of width equal to the total relaxation rate Γ. In the rotating frame of atom 1 the transverse spin of atom 2 precesses at the frequency $\delta\omega = \Omega_1 - \Omega_2$. If $\delta\omega \gg \Gamma$, in other words if the two spin noise resonances are far apart, the spin polarization of atom 2 seen in the rotating frame of atom 1 averages out to zero within the spin-exchange time of about $1/\Gamma$. If, however, $\delta\omega \leq \Gamma$, then the noise polarization of atom 2, transferred to 1, is seen as another band-limited noise term (of frequency width Γ) adding up to the fluctuation term dW_1 of atom 1. In particular, if the density $n_2 < n_1$, then the noise polarization of atom 2, on the order of $\delta P_2 \approx 1/\sqrt{n_2}$ is larger than the noise polarization of atom 1, on the order of $\delta P_1 \approx 1/\sqrt{n_1}$. Hence if the rate of polarization transfer from atom 2 to 1 is γ_{12} , while the rate of polarization decay is Γ, the spin polarization transferred from 2 to 1 will be on the order of $\delta P_{12} \approx (\gamma_{12}/\Gamma)(1/\sqrt{n_2})$. Hence the spin noise power of atoms 1 will be higher than the no-transfer value of $n_1^2 P_1^2 \approx n_1$ by the amount $n_1^2 \delta P_{12}^2$. The spin noise power of atoms 2 will be proportional to $n_2^2 P_2^2$, since the transfer from 1 is in this case ($n_2 < n_1$) less important. Hence the total spin noise power will be $n_1^2 \delta P_1^2 + n_2^2 \delta P_2^2 + n_1 \delta P_{12} \approx n_1 + n_2 + (\gamma_{12}/\Gamma)(n_1/n_2)$. Since $\gamma_{12} \propto n_2$ and $\Gamma \propto (n_1 + n_2)$, the relative spin noise power in excess of $n_1 + n_2$ is $n_1^2 n_2/(n_1 + n_2)$.

14
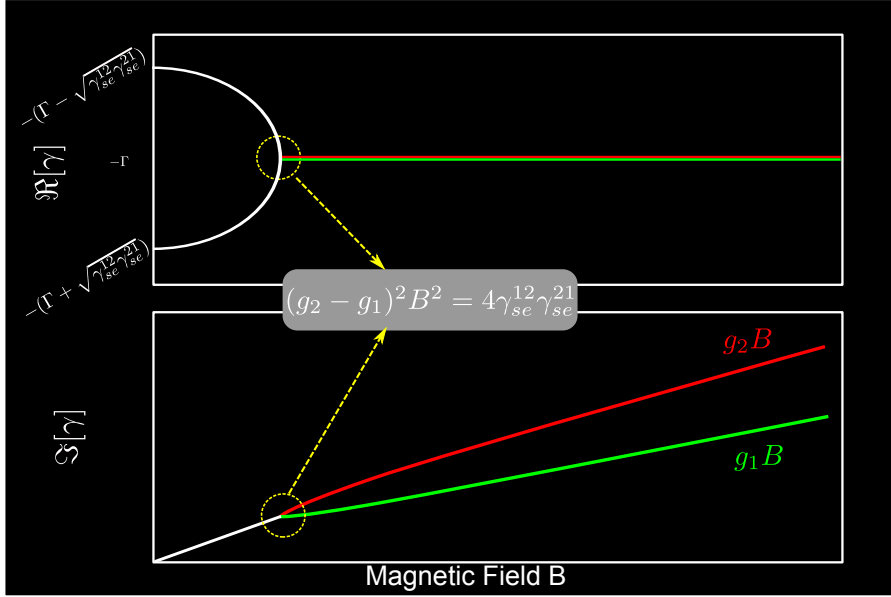
Figure 3.3.1: (Upper) Real and **(Lower)** imaginary part of the eigenvalues of the decay matrix A as a function of the magnetic field. At high magnetic fields the two rubidium isotopes precess at their respective Larmor frequencies, and their transverse spins decay at the same rate Γ. At low magnetic fields the spins are coupled by spin-exchange collisions and precess at a common frequency, while there are two decay rates. The transition between the two regimes happens at a few mG. This is reminiscent of the analogous phenomenon of a single atomic species at much lower magnetic fields on the order of μG.

For this particular case, where $n_1/n_2 \approx 3$, it follows that the excess spin noise power at low fields is 15% higher than at high fields, in good agreement with the exact value of 22%.

The low-field increase of the total spin noise power signifies a "phase transition" analogous to the suppression of spin exchange relaxation in a single species atomic vapor[1, 32, 19]. This is shown in Fig.3.3.1, where we plot the real and imaginary part of the eigenvalues, γ, of the decay matrix A, which are $\gamma = -\Gamma + i(\omega_1+\omega_2)/2 \pm \sqrt{\gamma_{12}\gamma_{21}-(\omega_1-\omega_2)^2/4}$. At high fields the spins of the two isotopes precess at their Larmor frequency ω_1 and ω_2, while they decay at the common rate Γ. However, at low fields the spin-exchange coupling forces them to precess at a common Larmor frequency $(\omega_1+\omega_2)/2$, while there are two decay rates, a fast decay rate $\gamma_{fast} = \Gamma + \sqrt{\gamma_{se}^{12}\gamma_{se}^{21}}$ and a slow decay rate $\gamma_{fast} = \Gamma - \sqrt{\gamma_{se}^{12}\gamma_{se}^{21}}$. The transition between the two regimes takes place at a field B_0 satisfying the equation $(g_1-g_2)^2 B_0^2 = 4\sqrt{\gamma_{se}^{12}\gamma_{se}^{21}}$ se for the experiment's temperature is $B_0 \approx 4$mG.

15

In this section we are going to briefly discuss the interaction of light and matter. In particular we will focus on the effect of the medium on the polarisation properties of light. This effect is known as Faraday rotation and it is used in order to extract information about system by observing the polarization change of a probe beam. A detailed analysis is beyond the scope of this thesis, thus we are going to summarise and reproduce theoretical results described analyzed in various scientific articles. The interested read may refer to [18, 55] for more detailed and complete theoretical analysis

3.4.1 *Hamiltonian*

The time evolution of a quantum mechanical system, in our case the ground state of the alkali atom, is described by the Liouville-von Neumann equation:

$$\frac{d\rho}{dt} = \frac{-\imath}{\hbar}\left[H, \rho\right] \tag{34}$$

The Hamiltonian H is useful to be decomposed in two parts [18]

$$H = H_0 + \delta H \tag{35}$$

with H_0 describing the ground state Hamiltonian of the alkali metal atom in the absence of light (i.e when an external magnetic field is applied). The effective Hamiltonian δH describes the interaction with monochromatic light and can be written as [21]:

$$\delta H = -\mathbf{E}^\star \cdot \ddot{\alpha} \cdot \mathbf{E} \tag{36}$$

where $\ddot{\alpha}$ is the atomic polarizability and $\mathbf{E}$ is the electric field.

3.4.2 *Polarizability and Faraday Rotaion*

The polarizability tensor $\ddot{\alpha}$ can be decomposed into a scalar, vector and rank two spherical tensors[18]:

$$\ddot{\alpha} = \sum_{L=0}^{2} \alpha^L = \alpha^{(0)} \oplus \alpha^{(1)} \oplus \alpha^{(2)} \tag{37}$$

As explained in [18] and [55] the rank-2 operator is identically zero as long as the hyperfine splitting separation of the excited states are neglected ($\alpha^{(2)} \approx 0$).

The angle of rotation of the polariation plane of linearly polarized light due to the interaction with the medium is given by [20]:

$$\theta = 2\pi \frac{\omega}{c} \frac{N}{V} \Re\left\{a_{gt}\right\} \langle \hat{\mathbf{n}} \cdot \mathbf{S} \rangle \, l \tag{38}$$

where N/V is the density of the alkali metal vapor, $\hat{\mathbf{n}}$ is the unit vector in the direction of light propagation, a_{gt} is the gyrotropic part of the polarizability defined as:

$$a_{gt} = \frac{11 - 4J_e(J_e + 1)}{4} a^{(0)} \tag{39}$$

and l is the length of the sample. In the case of a single atom confined in a cylindrical cell of length l interacting with laser beam of area A_{laser} the rotation angle of the polarization plane will be:

$$\theta_1 = \frac{11 - 4J_e(J_e + 1)}{16} \frac{r_e c f_{osc}}{A_{laser}\Gamma} \frac{\delta}{\delta^2 + (1/2\pi)^2} \tag{40}$$

where we have substituted $V = A_{laser}l$ and $\langle \hat{\mathbf{n}} \cdot \mathbf{S} \rangle = 1/2$. As already mentioned in the case of large detunings the rotation angle scales as δ^{-1}:

$$\theta_1 = \frac{11 - 4J_e(J_e + 1)}{16} \frac{r_e c f_{osc}}{A_{laser}\Gamma} \frac{1}{\delta} \tag{41}$$

3.4.2.1 Cross Section of Optical Absorption

In the same way we can calculate the absorption cross section. The detailed calculation is done in [55] and here the result is reproduced:

$$\sigma = \frac{r_e c f_{osc}}{4\pi\Gamma} \frac{1}{\delta^2 + (1/2\pi)^2} \left(1 + \frac{11 - 4J_e(J_e + 1)}{4}\right) \tag{42}$$

Thus the intensity of the light field experiences attenuation when it passes through a sample of density $[A] = \frac{N}{V}$ and length dl and it is described by:

$$dI(l) = -[A]\sigma I dl \tag{43}$$

4

EXPERIMENTAL SETUP

4.1 INTRODUCTION

In this chapter we will give the details of the experimental setup. We will describe all the individual parts used to construct the setup of this experiment, and in particular we will describe in depth the use of some equipment and instruments. Then we will describe the experimental setup used for the measurement of atomic spin noise and the procedure followed to collect the experimental data.

4.2 LASER AND DETECTORS

4.2.1 *Extended Cavity Diode Laser*

Diode lasers are widely used in physics and particular in atomic physics experiments [60]. They are preferred instead of other types of laser sources because of their spectral properties and ease of use. Diode lasers have narrow spectrum, their central wavelength can be easily tuned and the output power and wavelength can be easily manipulated (e.g amplitude modulation, laser frequency scanning). Moreover

Diode laser are widely used in atomic physics due to their excellent properties
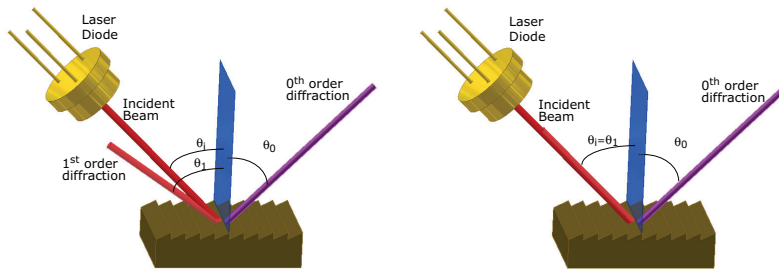
(a) Principle of diffraction from a grating. The beam coming from the laser diode impinges on a diffraction grating and is analysed to sever other beams according to the diffraction equation.

(b) In Littrow configuration the angle between the laser diode and the diffraction grating is changed so that the 1 st order of diffraction is back reflected to the laser diode.

Figure 4.2.1: Diffraction from a grating.

because of their widespread use (basically in optical storage devices) they provide an excellent value for money solution. To operate a laser diode one just needs to connect the diode to a current source. Additionally a thermoelectric element such as a peltier can be used to control the temperature of the diode. By changing the current and the temperature, the output power and wavelength can be tuned. Although the spectrum of laser diodes is quite narrow, on the order of a few GHz, in some cases narrower spectra is demanded. To satisfy this requirement a more sophisticated setup can be implemented. In this setup the laser diode is coupled to a diffraction grating. The grating acts as a wavelength filter providing optical feedback to the laser diode and forces it to oscillate to the desired mode. This type of setup is called Extended (or External) Cavity Diode Laser (ECDL). In the most popular Littrow configuration [3] the first order diffraction is coupled directly into the

Diffraction gratings act as wavelength filters providing optical feedback to the laser diode and forcing it to oscillate to the desired mode

diode and the zeroth order diffraction is used as the output beam (Fig.4.2.1.2). The diffraction of the grating is described by the following equation:

$$\sin(\theta_m) + \sin(\theta_i) = N\, m\, \lambda \tag{44}$$

where θ_i is the angle of the incident beam, θ_m is the angle of the m-th order diffraction, N is the lines per mm of the grating and λ is the wavelength. In Littrow configuration where $\theta_i = \theta_m$, Eq.44 is simplified to

$$m\, \lambda = \frac{2}{N} \sin(\theta_i) \tag{45}$$

It is thus possible to tune the wavelength of the laser by changing the angle between the incident beam and the normal to the grating. In the experiment performed for the
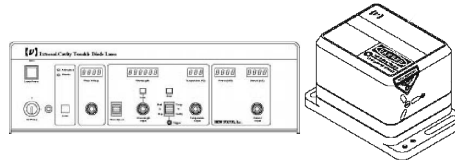
Figure 4.2.2: Laser Head and controller.

purpose of this thesis, we used several ECDLs, home made and commercials, while trying to optimize the experimental setup. After considering the needs in power and wavelength stability we ended up with a commercial ECDL from New Focus. The specific ECDL is capable of giving several mW of power and the wavelength is stable enough. Furthermore the wavelength can be locked to any desired value if a laser frequency locking technique is used.

4.2.1.1 Beam profile

In our analysis, discussed later, it is essential to know the profile of the beam. There exist several methods in order to measure the geometrical characteristics of a beam. We measured the profile of the laser beam by using a CCD camera[1]. The beam was impinging vertically on the CCD sensor and in order not to saturate the sensor, a neutral density filter was used. The image taken from the CCD camera was analysed and the dimensions of the beam profile could be extracted. Following this procedure we found that the beam used had an elliptical profile of dimensions 1.8mm × 1.15mm.

The beam's dimensions were measured by recording the profile in a CCD camera.

4.2.2 Photo-Detectors

Figure 4.2.4: Photodiode

Low noise, switchable gain photo-diodes were used to measure the laser signal

An essential part of experiments in atomic optics is the photo-detectors. The detectors used were silicon detectors designed for detection of light signals over 350 to 1100 nm wavelength range. When a laser beam strikes the detector's area, the photons excite electrons, a mechanism known as photoelectric effect, and a current is produced. The photo-detector used for the purpose of this experimental measurement was reversed biased PIN photodiode. A low noise, switchable gain trans-impedance amplifier was integrated to the photo-diode converting the current of electrons to voltage drop.

4.3 MAGNETIC SHIELD

A magnetic shield is used to isolate the samples from stray magnetic fields

This experiment requires low magnetic fields ranging from dc to a few mG. In order

---

1 Thorlabs DC210 640 × 480 pixels

20
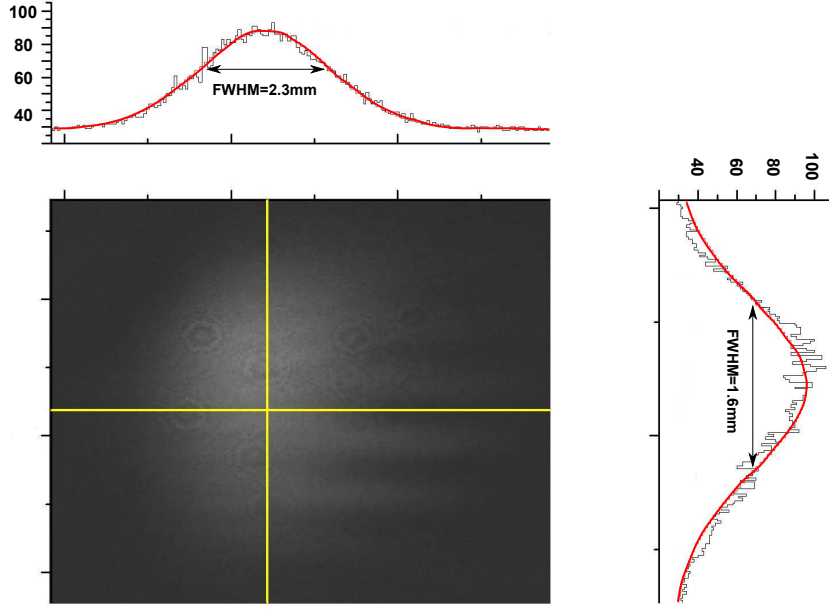
Figure 4.2.3: Profile of the probe laser beam.

PDA36A settings	
Responsivity:	0.5A/W
20 dB gain:	1.5104V/A
Bandwidth:	1MHz
NEP:	$2.34 \times 10^{-12} \mathrm{W}/\sqrt{\mathrm{Hz}}$

Table 2: setting of the photodiodes used to measure spin noise signal

to shield the atomic sample under study from the Earth's magnetic field (500mG) and from any stray external magnetic fields all the atomic samples were placed inside a magnetic shield which was constructed of 5 co-axial cylinders. Each cylindrical layer was made of Mu-metal having specific thickness. The magnetic shielding factor S is defined as the ratio of the applied field in the absence of the magnetic shield to the field measured inside the shield.

$$S = \frac{B_{ext}}{B_{int}} \tag{46}$$

For a cylindrical magnetic shield of one layer the field distribution is shown in Fig? and the shielding factor for this geometry is given by[51]:

$$S = \frac{\mu t}{2R} \tag{47}$$

where t is the thickness of the material and R is the radius of the cylinder. When the shield comprises more than one cylindrical layers, then the shielding factor is given by [11]:

$$S_{tot} = S_n \prod_{i=1}^{n-1} S_i \left[1 - \left(\frac{R_{i+1}}{R_i} \right)^2 \right] \tag{48}$$

(a) transverse configuration   **(b)** longitudinal configuration
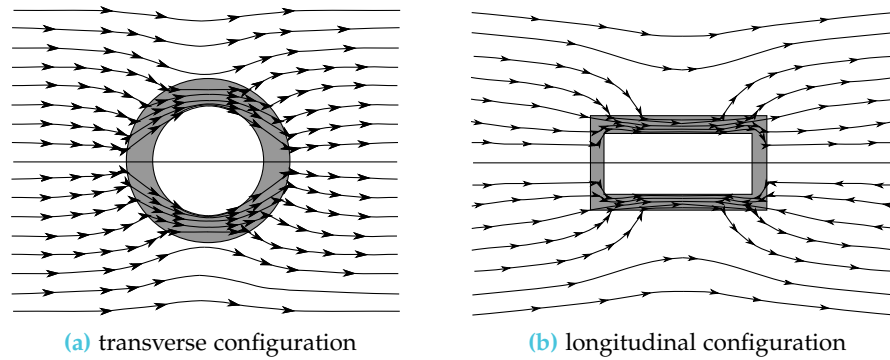
Figure 4.3.1: Magnetic lines distribution for a single layer of magnetic shielding (figure reproduced from [51]).

A set of 5 coils can generate magnetic fields on demand

Although the shielding factor is very high[2] the remaining field may still be undesirable. For zeroing the remaining fields the application of external fields of equal size but of opposite direction is required. A set of magnetic coils placed in the inner layer of the magnetic shield provides the desired magnetic fields. These coils can generate 3 vertical homogeneous magnetic fields and 5 independent magnetic gradients. The same set of coils can be used not only for canceling but also for applying magnetic fields in the three dimensional space [3]. These coils (Fig.4.3.2) designed by us [10] were controlled by a commercial power supply or by a multichannel computer controlled function generator[4].
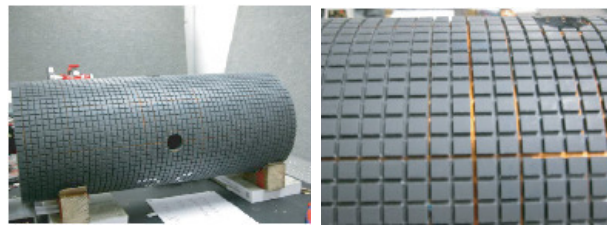
(a) All the coils are wired on the outer shell of a plastic cylinder. **(b)** Part of a magnetic coil embeded on the plastic cylinder

Figure 4.3.2: Apparatus of the magnetic coils used to apply any type of desired magnetic field..

4.4 CELL HEATING OVEN

An oven made of high temperature plastic was used to heat the atomic samples

Rubidium alkali metals used for this experiment are inside a glass cell in solid phase. In order to observe the desired effect it is necessary to create a specific vapor pressure. To achieve that the cell must be heated. The setup used for heating is more or less standard in this kind of experiments. The cell is placed inside a box which is made of high temperature plastic capable of sustaining temperatures above $100°$ Celcium. The space inside the oven is filled with hot air heated by an in-line heater.

---

2 this type of shield is capable of attenuating the external field by 4 orders of magnitude

3 this is done in the case of a spin precessing about a magnetic field at Larmor frequency

4 the multichannel function generator was designed and manufactured by the electronics workshop at I.E.S.L - F.o.R.T.H

Although the idea is pretty simple a few details should be taken into account. First of all the hot air should not interact with the probe laser beam, otherwise the intensity and polarization of the beam might arbitrarily change. This could produce noise, especially at low frequencies. Secondly the temperature of the cell should remain stable during the experimental measurement or else the vapor pressure and density would change. This latter requirement is satisfied by continuously monitoring temperature of the cell by a RTD sensing element and controlling the current of the in-line heater with a PID controller. The first requirement is fulfilled by designing a special oven like the one shown in Fig.4.4.1 It should be noted here that all the
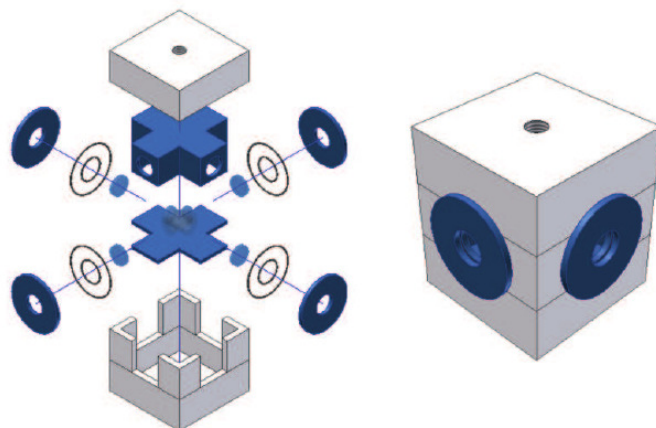
Figure 4.4.1: Oven used to heat the alkali metal vapor cell. The space where the cell is placed, is isolated form the hot air flow. (figure reproduced from [29])

parts of the oven where glued and sealed with high temperature silicone, thus we avoided using metallic screws which could produce magnetic inhomogeneities. Also the tubes used to guide the air to the oven were made from high temperature plastic for the same reason.

4.5 BALANCED POLARIMETER

The balanced polarimeter is a device used to measure the angle of rotation caused to the polarization plane of a linearly polarized light passing through a medium. A polarizing beam splitter (PBS) cube analyzes the beam to two other having orthogonal polarizations. The intensity of each beam is measured by a photo-detector. In the ab-
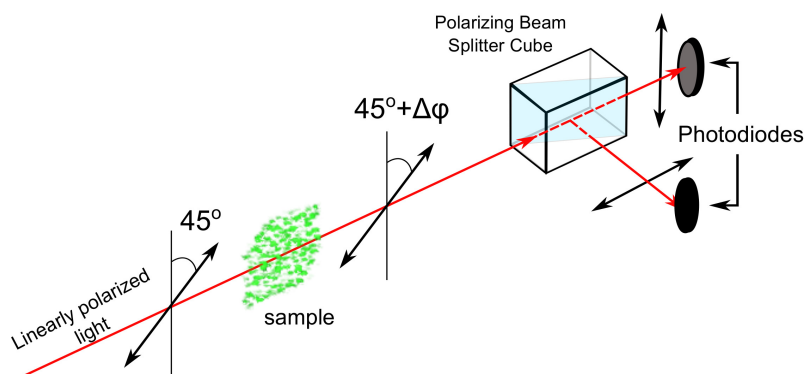
Figure 4.5.1: Balanced Polarimeter.

sence of optically anisotropic medium, the angle between the axis of the polarimeter and the polarization plane of the light is $45°$ and the laser power at the two branches

are equal. When the medium under study is placed in the path of the light it causes an extra rotation $\Delta\phi$ to the polarization vector. The intensity of light impinging on each photo-detector according to Fig.4.5.1 and assuming that $\Delta\phi$ is small[5] is:

$$P_{\parallel} = \left(\frac{P_\circ}{2}\right)(1 + 2\Delta\phi) \tag{49}$$

$$P_{\perp} = \left(\frac{P_\circ}{2}\right)(1 - 2\Delta\phi)$$

where $P_\circ$ is the value of the power of light, measured just before the PBS cube. The value of $P_\circ$ is about 1.0 mW just before the polarizing beam splitter cube. The photons impinge on the detectors and are transformed to electric current. The relation describing this transformation is $i = rP$ with r being the responsivity ($r \approx 0.5$ A/W) of the specific photo-detector. The signals at the outputs of the photo-detectors are subtracted and the remaining signal is proportional to the rotation caused from the medium under study:

In balanced polarimetry the medium under study rotates the plane of polarization of the laser beam

$$\Delta i = 2i_0\Delta\phi \tag{50}$$

The home made balanced polarimeter used for measuring spin fluctuations the photo-diodes used had integrated transimpedance amplifiers with variable gain which was set to $1.5 \times 10^4$V/A and was not changed during the experiment. The output voltage of each photo-diode was connected to the inputs of a low noise differential preamplifier, which did the subtraction and amplified the signal 100 times. At the last level, the output of the preamplifier was connected to the spectrum analyzer. The signal observed at the spectral analyzer is given by:

$$\Delta v = 2GP\Delta\phi \tag{51}$$

where G is the factor accounting for the conversion of laser power to voltage $G = (0.5$A/W$) \times (1.5 \times 10^4 \times$ V/A$) \times 100 = 750 V/mW)$.

PHOTON SHOT NOISE: No matter how carefully is the polarimeter constructed and if all the noise sources contributing to the uncertainty of $\Delta\phi$ are eliminated, there is still a noise source increasing the uncertainty of the measured rotation angle. The origin of this noise is fundamental and cannot be further reduced. It is associated with the randomness of arrivals of photons to the detectors and is known as photon shot noise. Consider a laser beam linearly polarized at $45°$ with respect of the polar-

Figure 4.5.2: Typical setup to measure photon shot noise

Photon Shot Noise is a fundamental noise source and cannot be eliminated

izing beam splitter cube. At the output of the cube the power of each beam will be $P_i = (P_0/2)$. Each beam strikes on the semi-conductive area of the photo-diode and excites electrons, creating electron current. The probability at which one photon creates one free electron is the quantum efficiency (QE) of the photo-diode. Although QE is a measure of the detectors efficiency a more experimental parameter is commonly used: the responsivity ($\mathcal{R}$) is a measure of the detectors gain and is given in A/W. QE and R are related by:

$$Q.E = \mathcal{R}\frac{hc}{e\lambda} \tag{52}$$

---

5 if $\Delta\phi \to 0$ then $\sin(\Delta\phi) \simeq \Delta\phi$

In order to model the noise at the output of each photo-diode we assume that the mean electron current of each photo-diode is $i_j = \langle i_j \rangle$ ($j = 1, 2$) and experiences random fluctuation $\delta i_j = \sqrt{\langle i_j^2 \rangle - \langle i_j \rangle^2}$. The electron current at each photo-diode is

$$\langle i_{e,j} \rangle = e(QE) \frac{\langle N_{ph,j} \rangle}{T} \tag{53}$$

and the noise due to fluctuations at the number of photons will be

$$\delta i_{e,j} = e(QE) \frac{\delta N_{ph,j}}{T_{acq}} \tag{54}$$

where T_{acq} is the acquisition time. T_{acq} also defines the bandwidth which is $\mathrm{BW} = 1/T_{\mathrm{acq}}$. The total noise when the signals of the two detectors are subtracted is

$$\delta i_e = \sqrt{\delta i_{e,1}^2 + \delta i_{e,2}^2} \tag{55}$$

Since photon shot noise (δN_{ph}) is a stochastic variable having Poisson distribution its expected value and its variance will be equal ($\delta N_{ph}^2 = N$). Taking into account that the total number of photons is conserved ($\langle N_{ph} \rangle = \langle N_{ph,1} \rangle + \langle N_{ph,2} \rangle$)

$$\delta i_e = \frac{e(QE)}{T_{acq}} \sqrt{\langle N_{ph} \rangle} \tag{56}$$

The number of photons is related to the power by: $P = \frac{hc}{\lambda T_{acq}} \langle N_{ph} \rangle$. Finally it is straight forward to show that the power spectrum of the detected voltage signal ($(\delta V)^2$), i.e at the output of the differential preamplifier is

$$(\delta V)^2 = 2G^2 \frac{hc/\lambda}{QE} P \quad \text{\small (units: V}_{\mathrm{rms}}^2/\mathrm{Hz)} \tag{57}$$

The factor 2 is because the one sided spectrum is observed in an instrument like a spectrum analyzer. Moreover since expectation values ($\langle \Psi \rangle = T^{-1} \int_0^T \Psi dt$) over a time interval are used, the calculated value of the power spectrum will be in rms.Polarimeter Noise

MEASUREMENTS: In order to measure the contribution of photon shot noise to the total noise level of the polarimeter we did the following: We saved several power spectra, each for a different laser power[6]. According to Eq.57 if photon shot noise was the only noise source, then the power spectral density of the measured signal should be proportional to the laser power.

Photon Shot Noise is proportional to the square root of laser power

From the measurement shown in Fig.4.5.3 it is seen that the signal of the polarimeter is close to the theoretical prediction, especially for low laser power.

4.6 ATOMIC SAMPLES

The atomic samples used for the purposes of this thesis are Rubidium vapors. Two different systems are studied. In the first system a cylindrical glass cell of 10 cm length and 2.5 cm diameter contains Rubidium of natural abundance ($\sim 72\%$ ^{85}Rb and $\sim 28\%$ ^{87}Rb) and. In the second system two glass cells each of 5 cm length and 2.5 cm are placed back to back. All cells are filled with 100Torr of Nitrogen.

4.7 OTHER EQUIPMENT

Besides the above instruments used to perform the experiment described in this thesis many other complementary instruments were used. The most important of them are:

---

6 Each power spectrum consisted of 2500 averages.
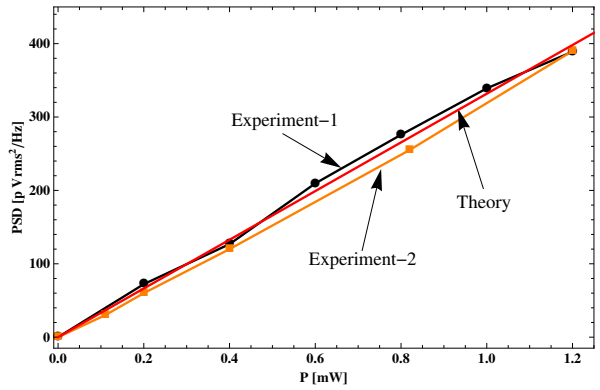
Figure 4.5.3: Measurement of photon shot noise level. The green line is the theoretical prediction.
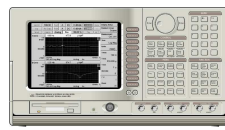
Figure 4.7.1: Spectrum Analyzer

FFT SPECTRUM ANALYZER The FFT analyzer used, was the SR785 Dynamic Signal Analyzer by *Standford Research Systems*. Its bandwidth is from DC to102.4kHz. The signal acquired is digitized by a 16bits Analog to Digital converted with a sampling[7] rate of 262kHz. For the experiment presented in this thesis, the measurement bandwidth was set to 50 kHz and the frequency resolution for 800 FFT lines was equal to $62.5 Hz$. More specifically the settings of the spectrum analyzer used for this experiment are shown in Table **??**

SRS-785 settings			
Frequency settings		*Measurement settings*	
Start Frequency:	0 Hz		
Bandwidth	50 kHz	Measurement group: FFT	
Line-width:	62.5 Hz	Measurement: Power Spectrum	
Acquisition Time:	16 ms	Units: PSD, dB	
FFT lines:	800		
Window:	BMH		
Averaging settings		*Input settings*	
Average Type:	Linear-Fixed Length	Input Mode:	A, Ground
Number of Averages:	100	Coupling:	AC
Display Average:	RMS averaging	Input Range:	-20 dB
Time Record Increment:	100		

Table 3: spectrum analyser settings

---

7 according to Nyquist's theorem the sampling rate should be at least two times larger than the hist frequency of the measured signal

DIFFERENTIAL PREAMPLIFIER: In order to subtract the signals coming from the two photo-diodes of the polarimeter, we use a differential pre-amplifier. The outputs of the photo-diodes are connected to the two high-impedance inputs of the pre-amplifier and the difference signal can be amplified before coupling the out-

Figure 4.7.2: Differential Preamplifier

put to the input of the spectrum analyzer. Besides the subtraction the pre-amplifier can be used to filter the output signal by using the the two integrated signal filters.

SR560 settings

Filter settings	Input settings	Gain settings
Cutoff: 100Hz	Coupling:AC	Gain Mode: 2×10^2
High Pass: 6bB	Ground	Dynamic Reserve
		Gain: 10^2

DAQ SYSTEMS AND LABVIEW: Because of the large amount of data acquired and due to the long time duration of the experiment, it was decided that it would be appropriate that most of the experimental procedure should be computer controlled. For this reason all the signals necessary for the data analysis were connected to Data-Acquisition (DAQ) cards and saved to a computer. The signals from all sensors were connected to the *NI USB-6259 BNC* multifunction data acquisition (DAQ) module. The same card was also used to provide signal in order to control instruments. A typical example is the procedure used to keep the laser wavelength stable. A wavelength meter used to read the laser optical frequency was connected via USB-port to the computer. The value of the laser optical frequency was read using a data acquisition software and was compared to the desired optical frequency. The output of the DAQ-card provided a signal proportional to the difference of the actual and the set frequency which was used to control the grating of the laser and thus fine tune the laser wavelength. Moreover the SRS785 spectrum analyzer was connected to a PCI-GPIB card and the signal of the spectrum analyzer was monitored and saved to the same computer station. The software used to program the DAQ cards and synchronize the acquisition procedure was *NI-LabView*.

WAVELENGTH METER: The monitoring of the optical frequency of the laser is done by a Fizeau-based interferometer. The laser light is coupled to a solid state Fizeau interferometer and the interference pattern is projected onto a CCD photodiode arrays. The software compares the real time pattern with a pre-recorded calibration pattern and calculates the optical frequency. The wavelength meter used in this experiment had accuracy of about 50MHz

FLUXGATE MAGNETOMETER: Sometimes it was necessary to know the absolute value of the magnetic field inside the magnetic shield. For example before placing the oven with the samples inside the magnetic shield we followed a procedure in order to zero the remaining magnetisation of the shielding layers. We used a type of magnetic sensor the fluxgate magnetometer. The sensor used, was a three - axis sensor[8] capable of measuring magnetic fields at three vertical axis simultaneously. The principle of operation of the fluxgate magnetometer relays on the change of magnetic flux in the magnetic core of the sensor which is measured by an sensing coil. At the specific magne-

Figure 4.7.3: Fluxgate manetometer

---

8 Bartington Mag-03MC

tometer 0.1 volts at the output of each sensor result at 1μT and according to the manufacturer the noise level of the fluxgate sensor is $8pT_{rms}/\sqrt{Hz}$.

In this section we present the complete setup (Fig.4.8.1) arising by integrating the individual parts described previously. The laser beam is provided by the ECDL and the power measured just before the magnetic shield is about 3mW. At the output of the laser, an optical isolator (O.I) is placed to prevent back-reflections to the laser diode. The linear polarizer at the output of the O.I ensures that the polarization of the laser beam is linear. Additionally the beam passes through a second linear polarizer (L.P). A beam splitter (B.S) placed before the L.P reflects a small fraction of the beam~10 % which is used to continually monitor to the optical frequency and the power by using a wavelength-meter (W.M) and a photodiode respectively. Another B.S is placed just after the L.P and the intensity of the laser of the reflected beam is recorder by a photo-diode (P.D). Thereafter the laser beam passes through the oven which contains the cells with the atomic vapors. The atomic samples (inset of Fig.4.8.1) may be on the same cylindrical cell[9], or in two different cells which are placed back to back[10]. After interacting with the atoms, the laser beam is partially reflected to a photo-diode for monitoring the intensity fluctuations, and the transmitted part is directed to the polarimeter. Due to reflections on the windows of the oven and of the cell, the power of the laser is decreased and just before the entrance of the polarimeter it was measured to be about 1.1 mW. As already explained, the polarimeter consists of a $\lambda/2$ retardation plate, a polarizing beam splitter cube (PBSC) and two photo-diodes[11]. The photo-diodes come with integrated transimpedance amplifiers of variable gain[12]. The signals from the two photo-diodes was connected to the inputs of the differential preamplifier and subtracted. The subtracted signal is at the same time amplified with an amplification factor 100. Finally the subtracted signal is connected to FFT spectrum analyzer[13] and the power spectrum of the signal is recorded. The signal at the output of the differential amplifier will be the sum of the spin noise signal, the photon shot noise and the electronic noise. The photon shot noise is given by Eq.(57), the electronic shot noise is the signal measured at the spectrum analyzer when the laser light is blocked and is the sum of the photo-diodes dark current the differential preamplifer's electronic noise and the spectrum analyzer's electronic noise. The spin noise signal will be given by Eq.32. Thus the total recorder signal will be:

Signal coming from subtracting the two PDs outputs is analyzed in a FFT spectrum analyzer and the power spectrum is recorded

$$(S_{total})^2 = (\delta u_{ASN})^2 + (\delta u_{PSN})^2 + (\delta u_{EN})^2 \quad \text{(units: V}^2_{\text{rms}}/\text{Hz)} \tag{58}$$

It is essential in every experimental measurement that the signal under study should be higher than the background signal. In our experiment the signal to noise ratio *SNR* is defined as

$$SNR = \frac{(S_{total})^2}{(\delta u_{PSN})^2 + (\delta u_{EN})^2}$$

is about $SNR = 3$. The *SNR* can reach higher values by increasing the power of the laser beam, or be reducing its diameter, but then the total relaxation rate will not anymore be spin exchange dominated and the phenomenon of spin noise exchange will be masked.

Figure 4.8.1: Experimental schematic of the spin noise measurement. For the actual measurement we used a 10 cm long cell with rubidium of natural abundance. In a second, consistency-check measurement we use two cells back-to-back, each 5 cm long and having isotopically enriched rubidium. The laser beam after interacting with the alkali vapors is guided to a balanced polarimeter and the power spectrum of the signal is recorded to a FFT spectrum analyzer. A computer controlled D.A.Q system monitors all the relevant experimental parameters and also controls the magnetic fields.
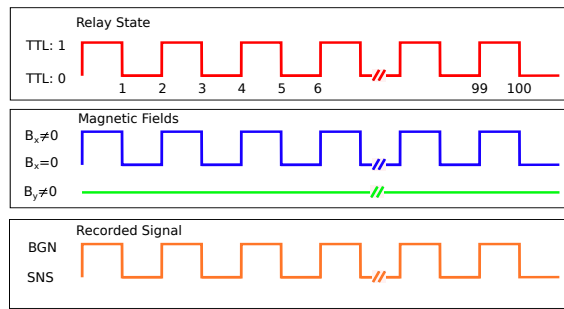
Figure 4.8.2: Schematic depicting the data acquisition progress. A TTL pulse controls the state of relay switching the magnetic field along the x-axis. When the relay state is 0 the spin noise signal is recorded, whereas when then TTL state is 1 the background signal is recorded.

4.8.1 *Spin Noise Acquisition:*

As described previously, the spectrum analyzer is connected and controlled from a computer via a PCI-GPIB card. When the experiment is running the S.A records the power spectrum which consists of 100 averages and transmits the data of the averaged spectrum to the computer. This is a single run of the experiment. In total a complete measurement set consists of 50 runs recording the spin noise signal and 50 runs recording the background signal, i.e the power spectrum in the absence of spin noise. The background signal was measured by applying a large magnetic field in order to shift centers of the spin noise resonance peaks out of the detection bandwidth which in our case was 50 kHz. In Fig.4.8.2 a graphical sketch of the time evolution of the data acquisition is shown.

The acquisition procedure is computer controlled. The PSD in the absense of spin noise is subtracted from spin noise PSD

4.8.2 *Magnetic Field control:*

Power supplies capable of providing electric current up to $3A$ were connected to the magnetic coils. Although there were 8 magnetic coils available, three producing spatially homogeneous magnetic fields and five coils producing spatial gradient fields, only three coils were used in order to generate homogeneously fields along the x, y and z axes. The magnetic field along the y-axis was tuned from $0mG$ to $50mG$ which corresponds to larmor precession from $0kHz$ to $30kHz$.

The magnetic field along the x-axis was always set to 300mG, i.e the larmor precession frequency was about $150kHz$. Because the range of frequencies recorded by the spectrum analyzer was chosen to span from $0Hz$ up to $50kHz$, when the field along the x-axis was applied, the spin noise resonances were outside the recorded frequency range, and thus only the background level of the spin noise signal was recorded. The third coil generating a magnetic field along the z-axis was used in order to zero the remain field in this direction. The
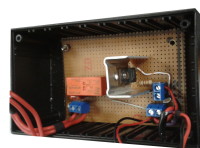
Figure 4.8.3: Relay controlling the current of the B_X coil.

---

9   the cell is manufactured from *Triad Technology inc.* and has $1in$ diameter and $10cm$ length. It contains both Rb isotopes at natural abundance, and $100Torr$ Nitrogen

10 each of the two cells is manufactured from *Triad Technology inc.* and has 1in diameter and 5cm length. Each cell contains only one of the two Rb isotopes, and 100Torr Nitrogen

11 Thorlabs PDA36-A

12 the responsivity of the photo-diodes is r $\sim 0.5\,\mathrm{A/W}$ and the gain was set to g $= 1.5 \times 104\,\mathrm{V/A}$

13 SRS-785

power supply of the B_y coil was always switched on and the current of the B_x coil was controlled by a mechanical relay-switch. A TTL pulse (provided from the DAQ module's signal output) could change on demand the state of the relay. In this way the magnetic field of the B_x coil was non-zero only when we wanted to record the background signal.

4.8.3 *Laser Parameters Acquisition:*
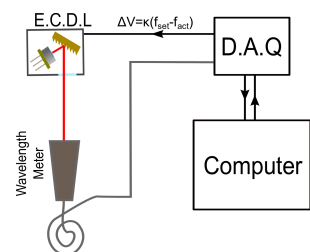
Figure 4.8.4: Schematic shown the laser frequency locking setup.

Simultaneously to acquisition of the polarimeter signal, the power intensity and frequency of the laser are also recorded. This step is necessary because changes on the intensity and frequency affect the detected spin noise signal as will be explained later. The signals of photo-diodes P.D-3 and P.D-4 are connected to the DAQ module and recorder over the whole time of the experiment. Changes on the intensity due to the current biasing the diode or due to improper optical coupling of the light diffracted from the diffraction-grating to the laser diode, would be detected from PD-3. Changes on the intensity originating from the heating oven are measured from P.D-4[14]. The wavelength meter is also connected (via standard USB port) to the computer and the frequency of the laser is also monitored.

All the essential parameters are monitor. Moreover the laser frequency is stabilized by a feedback circuit.

LASER FREQUENCY LOCK: The optical frequency of the laser is prone to changes caused by mechanical vibrations and temperature changes. In order to avoid changes on the spin noise signal due to variations of the optical frequency, a feedback scheme is used. The value of the frequency f_{act} is compared with the desired (f_{set}) value. A voltage proportional to the difference of the two values is connected to the inputs of the laser controlling the position of the diffraction grating by a piezoelectric transducer.

---

14 If hot air leaks to the area where the cell is placed, then gradients of the temperature may result to changes of the refractive index seen by the laser

DATA ANALYSIS

5.1 INTRODUCTION

As already has been mentioned a complete measurement constituted of 100 runs.Each run was the average of 100 power spectra. The 50 runs were measurements of the atomic spin noise signal and the other 50 were for the background signal (Fig.4.8.2). The spin noise signal was recorder for two different atomic samples. In the first case a cell was containing Rubidium atoms of natural abundance. In the second case two cells were placed back to back and each cell was containing only one of the aforementioned Rubidium isotopes. In total the spin noise signal (and the background signal) was measured for six different magnetic fields. The experiment was repeated 6 times for the case of the single cell and three times for the case of two cells. The analysis of the data was performed in *Mathematica*. The same algorithm was used for the analysis of all the all the experimental data.

5.2 ANALYSIS

The signal was recorded at the FFT spectrum analyzer. After units restoration[1], the background spectrum was subtracted from the spin noise spectrum in order to remove the contributions of the photon shot noise end electronic noise from the signal under study. The "background free" spin noise power spectra are going to be integrated in order to investigate the dependence of the integrated spin noise power to the magnetic field. In order to calculate the integrated spin noise power (ISNP) two
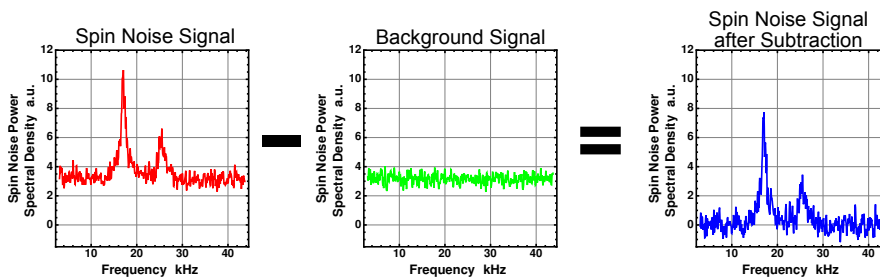
Figure 5.2.1: On the left the signal resulting from averaging 100 spectra is shown. The two resonances at 17 kHz and 25 kHz for ^{85}Rb and ^{87}Rb respectively are clearly distinguishable. The middle signal also results from averaging 100 spectra but the resonance peaks are shifted away from the recorded frequency span. On the right the result of the subtraction of the two signals is shown.

methods are used. In the first method we apply a fit algorith to in order to find an analytic expression for the power spectrum and then calculate the integral of this function. In the second method we numerically integrate the acquired data.

5.2.1 *Non Linear Fit*

The 50 power spectra are averaged to produce a single spectrum. Effectively this power spectrum consists of $100 \times 50 = 5000$ averages. The averaged spectrum is fit-

---

1 The recorded signal was in units of $^{dB_{rms}}$/Hz. In order to convert the units to V^2_{rms}/Hz the following transformation has to be done: $V_{PSD} = 10^{V_{dB}/10}$
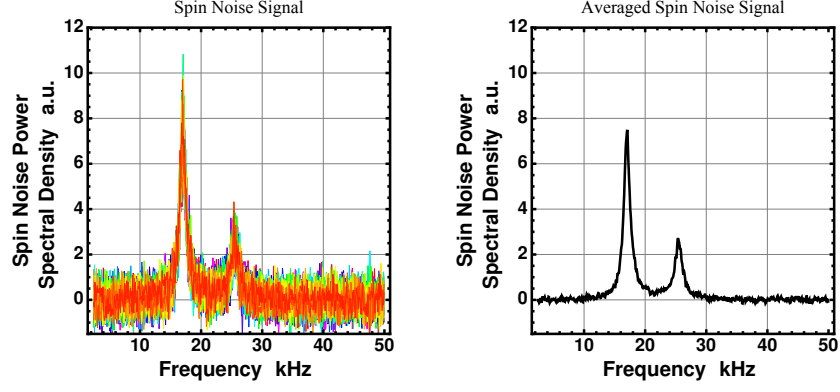
Figure 5.2.2: **Left:** In this plot 50 power spectra are shown together. Each one of the 50 PSDs is constructed after averaging 100 spectra.
Right: Averaging the 50 PSDs shown at the left results in a power spectrum where the noise fluctuations are definitely reduced. This power spectrum is used in order to apply the non linear fit algorithm.

ted with a Lorentzian line-shape. Since all the recorded spectra consist of two peaks, one from ^{85}Rb and one from ^{87}Rb, the fitting function would be the sum of one or two Lorentzians with different centers depending whether or not the peaks are distinguishable or not. The general form of the function used for the fit is

$$F(f) = y_0 + \sum_{i=1}^{2} A_i \frac{1}{4(\frac{f-f_i}{w_i})^2 + 1} + \sum_{i=1}^{2} A_i \frac{1}{4(\frac{-f-f_i}{w_i})^2 + 1} \tag{59}$$

A_i is the amplitude of the ith Lorentzian, f_i is the center and w_i is the full width at half maximum ($i = 1$ for ^{85}Rb and 2 for ^{87}Rb). The last term of Eq.(59) takes into account the mirroring of the negative frequencies into the positive axis. The Integrated Spin Noise Power is calculated by integrating Eq.(59) after subtracting the constant term y_0

$$ISNP \quad = \quad \int (F(f) - y_0) df \tag{60}$$

A_i and w_i are estimated within an error given by a the fit algorithm. Thus the $ISNP$ will be estimated within an error which is given by

$$\delta ISNP \quad = \quad \sqrt{\sum_{i=1}^{2} A_i w_i \pi \left[\left(\frac{\delta A_i}{A_i} \right)^2 + \left(\frac{\delta w_i}{w_i} \right)^2 \right]} \tag{61}$$

For the calculation of the fit we only used data from frequency bins above a cut-off level (about 1.5 kHz) to suppress contamination from 1/f noise.

COMBINING EXPERIMENTAL RUNS   As mentioned previously three runs of the experiment were performed for the cell with both isotopes and three runs for the case when two cells back to back were used. Since each run is statistically independent from the others the combined result will be the sum of the weighted means, normalized by the sum of the weightings [23]:

$$ISNP_{\text{comb}} \quad = \quad \frac{\sum_{i=1}^{3} ISNP_i}{\sum_{i=1}^{3} b_i} \tag{62}$$

$$b_i \quad = \quad \frac{1}{(\delta ISNP_i)^2}$$

34

and the error of the ISNP resulting from the combination of the three runs will be:

$$\delta ISNP_{comb} \quad = \quad \left(\frac{1}{\sum_i (\delta ISNP_i)^2} \right)^{-1/2} \tag{63}$$

BIAS CORRECTION   In order to correct for the overestimation coming from the $1/f$-noise we numerically simulated spin noise spectra having the same signal-to-noise ratio as the real data and we fit them starting from the same cut-off frequency. The integrals of these spectra are known, so we could infer the statistical error and possible bias of the integral computed from the fitted Lorentzian. It turned out that the latter overestimates the true integral by 4-5% at the lowest two magnetic fields, where part of the Lorentzian line shape is hidden in the $1/f$ noise tail, thus not available to fit. Since the correction factor for every one of the three independent measurement sets was calculated we corrected the ISNP of the fit with this factor.

The combined result of all the runs is shown in Fig.5.2.3. In this figure the results are normalized by the value of their ISNP at the highest magnetic field, i.e at 50 mG. The error bars are calculated from Eq.61 and Eq.63 and is about 2%. It is clearly observed that the total spin noise power increases by about 20% at low magnetic fields where the two magnetic resonance lines overlap.
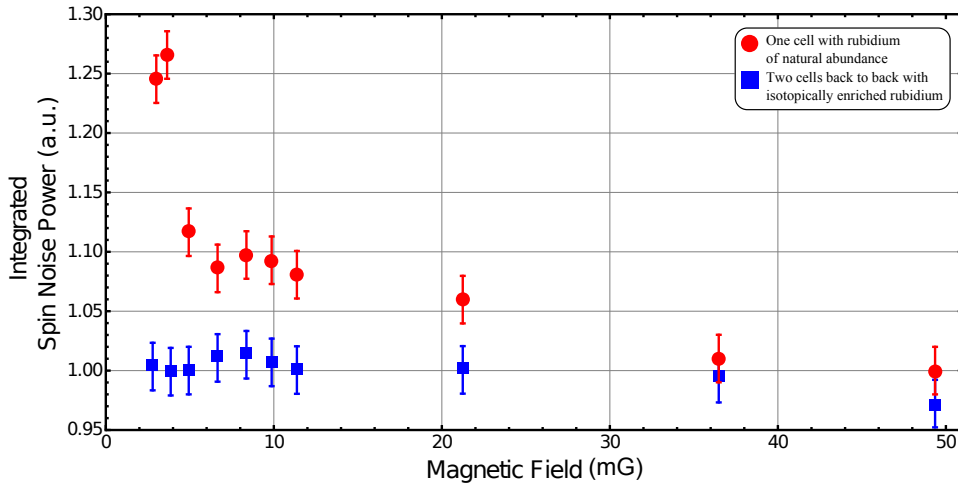
Figure 5.2.3: Integrated Spin Noise Power calculated by integrating the power spectrum of Spin Noise Signal calculated from the non linear fit. Red line is for the case that both rubidium isotopes are enclosed on the same cell. Blue line is for the case that two cells, each containing only one of the rubidium isotopes are placed back to back

5.2.2 *Numerical Integral*

The second method for calculating the ISNP is to numerically integrate the acquired data. Unfortunately as the Larmor precession approaches 0 Hz the contribution of the $1/f$ noise dominates the Spin Noise signal. Even after subtracting the background signal from the spin noise signal (as shown in Fig.5.2.1) at low frequencies signal coming from the $1/f$-noise is not eliminated and is superimposed to the spin noise signal (Fig.5.2.4). On the other hand at larger frequencies where the cental frequencies of the resonance lines are far way from the $1/f$-noise the method of the numerical integration will give a trusted result. In order to be able to numerical integrate all the acquired data we used the following procedure. In the first step the 50 power spectra (each consisting from 100 averages) were averaged to get a spectrum like the one shown in Fig.5.2.2. Then if the central frequency of the spin noise resonance line
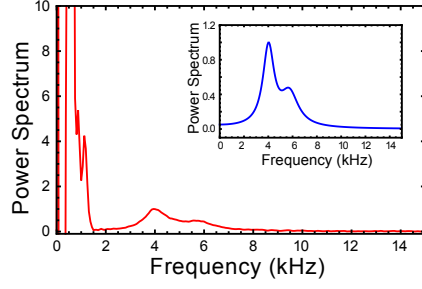
Figure 5.2.4: The contribution of the $1/f$-noise distorts the signal, especially when the centers of the spin noise resonance is at low frequencies ($<$ 2 kHz). **Inset:** Power spectrum given from Lorentzian fit
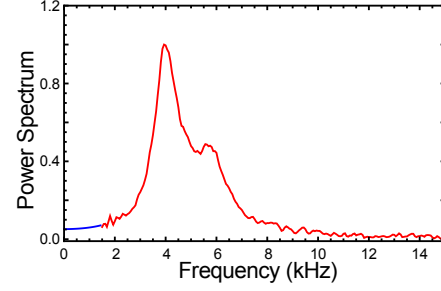
Figure 5.2.5: Spin Noise power spectrum after replacing low frequency data-points ($<$ 1.5 kHz) with those calculated from Lorentzian fit

was near to the 1/f-noise we used the result of the non linear fit of the previous method and we replaced the experimental data up to ~ 1.5 kHz with data obtained from the fit Fig.5.2.5. Lastly the hybrid power spectrum was numerically integrated. The INSP from this method is shown in Fig.

ERROR OF NUMERICAL INTEGRATION   The error of the numerical integral is dominated by the fluctuations of the power spectrum. The signal originates from random fluctuations on the orientation of the electronic spin. It is thus expected that in every realization of the measurement the signal will differ. Moreover as already mentioned the signal of the polarimeter has contributions from the photon shot noise and the electronic noise. Both these terms are random signals whose power spectra have a constant offset and fluctuations which depend on the measurement time. So even if photon shot noise and electronic noise are subtracted from the original signal the fluctuations, which are uncorrelated in every realization, remain. The obtained spin noise signal will then have superimposed on it the fluctuations of the electronic noise and the photon shot noise.

STATISTICAL ERROR   In order to estimate the error of the numerical integration we should know the precision at which we have calculated the mean value of the integral. As already have been described the Integrated Area is calculated after numerically integrating the average of the 50 power spectra. To estimate the error, the numerical integral of every single spectrum is calculated and then the histogram of these 50 values is plotted. Since variation of the integrated signal is due to random errors, the histogram will be described by a normal distribution with center at the mean value (μ) of the integrated signal and width equal to the standard deviation (σ). The value that best describes the uncertainty on the location of the calculated mean value is the standard error:

$$\sigma_\mu = \frac{\sigma}{\sqrt{N}} \tag{64}$$

where N is the number of repeated measurements.

5.2.2.1 *Total Error of the numerical integration*

As mentioned in this section, in order to calculate the numerical integral we replaced the acquired data in every spectrum up to 2.5kHz. In order to estimate the total error we should count in the errors from both contributions. I the two methods that are
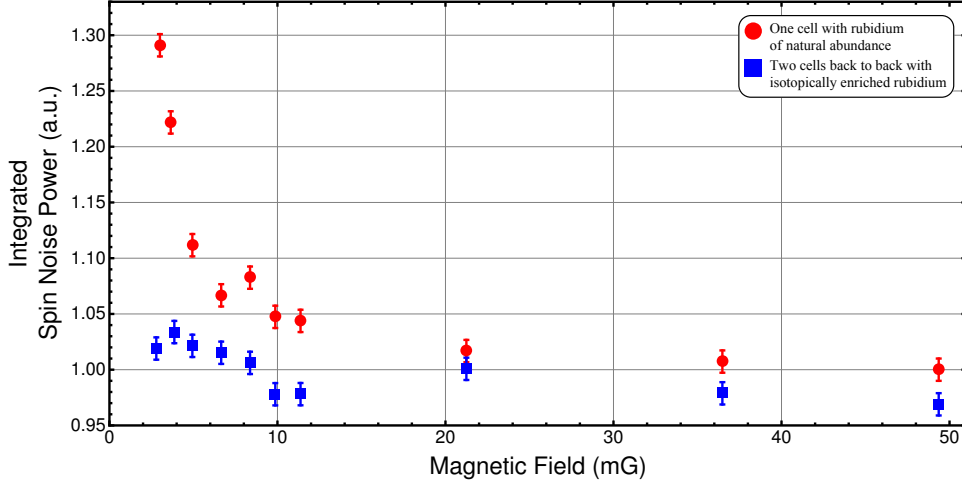
Figure 5.2.6: Integrated Spin Noise Power obtained by numerical integration of the experimental data. Red line is for the case that both rubidium isotopes are enclosed on the same cell. Blue line is for the case that two cells, each containing only one of the rubidium isotopes are placed back to back. For both traces the integral is calculated
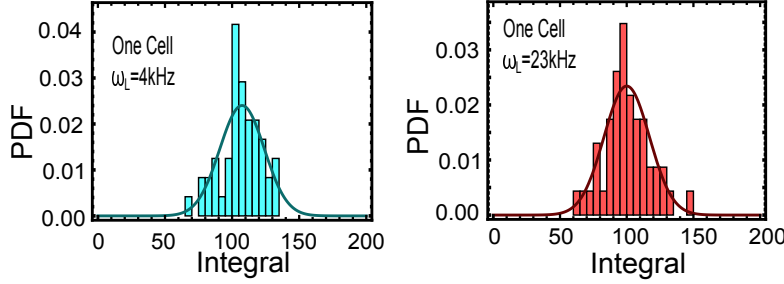
(a) Histogram of the integrated signal, in the case of one cell, for two different magnetic fields
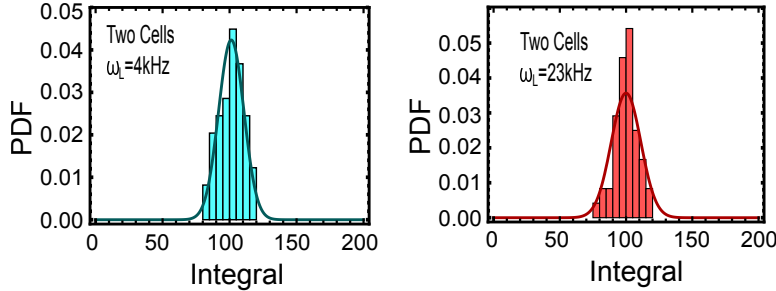
(b) Histogram of the integrated signal, in the case of two cells, for two different magnetic fields

Figure 5.2.7: Histograms of the integrated signal

combined where uncorrelated the total error would be the square root of the sum of the squares of the two errors. Since the two methods are correlated the appropriate formula for estimating the total error is:

$$\delta ISNP_{num} = (\delta S_{numerical}) \qquad (65)$$

$\delta S_{numerical}$ is the statistical error calculated from the histograms.

5.2.3 *Experiment and theory comparisson*

According to the theoretical model developed in Chapter 3 it is expected that the ISNP will increase as the spin noise resonances of the two Rubidium isotopes overlap. In Fig.5.2.8 the results obtained by the method of the non linear fit are represented

Figure 5.2.8: Integrated Spin Noise Power obtained by integrating the experimental data with the method of the non-linear fit described previously. When the two isotopes are separated and placed in different cells (blue squares) the ISNP remains constant. In the case that both isotopes are in the same cell (red dots) the ISNP decreases with increasing the magnetic field.
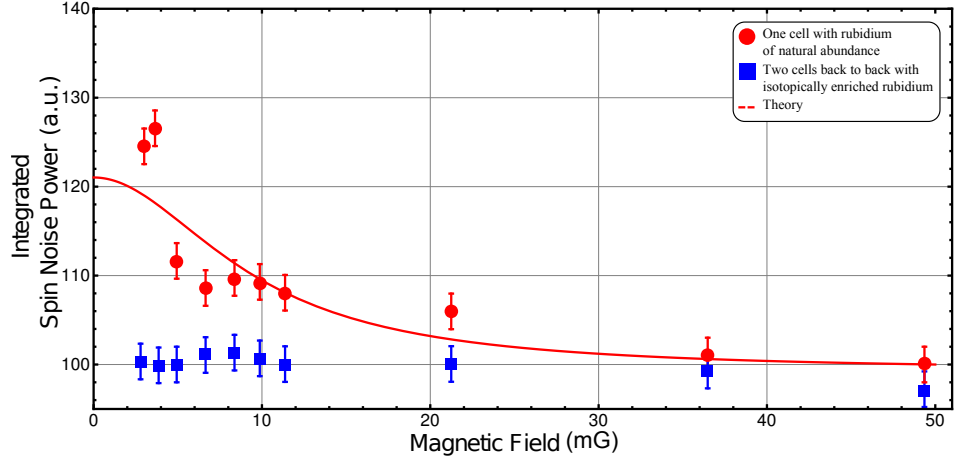
in the same plot with the theoretical model. When both isotopes were contained in the same cell it is more than clear that the ISNP increases as the applied magnetic field decreases. On the contrary, when the isotopes are separated and are contained in different cell then the ISNP remains constant irrespective of the magnetic field at which the measurement is performed. In order to evaluate the theoretical prediction we set the temperature equal to $105\,^{\circ}\mathrm{C}$. This temperature is inferred from the spin noise resonance width and it is the rubidium density corresponding to this temperature that we used in the theoretical prediction despite the fact that the indication of the RTD sensing element was $112\,^{\circ}\mathrm{C}$. The difference between the measured value of the temperature and the one calculated from the resonance width is due to inhomogeneities in temperature inside the oven. More over the probe laser power and detuning were $P = 1.5\,\mathrm{mW}$ and $\delta = 43\,\mathrm{GHz}$ respectively while the linewidth of the optical line is about $4\,\mathrm{GHz}$.

5.3 CONCLUSIONS

Concluding, we have experimentally demonstrated for the first time the transfer of quantum fluctuations of the collective spin from one atomic species to another. The signature for spin noise exchange is a counter-intuitive increase in the total spin noise power, fully accounted for by the coupled-spins Bloch equations including stochastic fluctuations. Although we demonstrated the phenomenon using a thermal spin state (i.e. an unpolarized spin ensemble), the exact same phenomenon would occur, albeit harder to observe, in a maximally polarized spin ensemble in the so called coherent spin state[46]. Our findings could have wide ranging impact, from spintronic devices to hydrogen-deuterium spin-exchange collisions in astrophysical environments.

Part II

BIOMOLECULES

Quantum mechanical phenomena in biological systems have been identified and are believed to underly the mechanisms of photosynthesis and magnetic sensation. Major concepts of quantum mechanics such as entanglement and coherence have already been observed and studied in the laboratory. It is thus a logical consequence to wonder about the existence of non-trivial quantum phenomena in natural systems. At first sight one might think biological systems such as macromolecules and living organisms on the one hand and well prepared and isolated systems on the other have nothing in common. Low temperatures, ultra high vacuum and the absolute control of the system was a prerequisite in order to observe the quantum mechanical aspect of matter. All these constraints are far beyond the "wet and messy" environment most biological organism face. It is the interaction of the system with the noisy environment that tends to destroy coherence. Thus if any quantum mechanical effects should exist in nature, an optimization between quantum dynamics and environmental noise is necessary. Experimental results in recent years suggest that quantum processes exist in the natural life. Evidence for quantum effects have been found in photosynthesis and in the route that energy follows from antennae molecules to reaction centers. Moreover tunneling effects are well known in enzyme catalyzed reactions and a recent theory of olfaction states that smell is the result of biochemical sensing molecular vibrations. The last few years new experimental facts about avian magneto-reception have resurged attraction about the physical mechanism underlying the ability of animals to sense geomagnetic fields.

It was in the middle of the 19th century when von Middendorf[56] first proposed that birds may use the geomagnetic field in order to orient and navigate. Since then there have been various hypotheses about the navigation mechanism birds utilize. Birds might rely on different cues in order to successfully reach their destination. Homing pigeons memorize visual landmarks which provide them guidance along their route[4]. Migratory songbirds use the direction of light cues such as stars, Sun or Moon to navigate. Even in low irradiation conditions, birds can indicate the position of the Sun[38] by detecting polarized light. Other studies on avian navigation mechanisms suggest that birds use auditory[17] or olfactory cues[58].

Magnetic compass on migratory birds, fish and other animals has been demonstrated. Two types of magnetic compasses have been identified. The first is similar to the usual technical compass used by humans and is named polarity compass. This type of compass can distinguish between magnetic North and South. The other type is the inclination compass, which cannot distinguish magnetic North from South but obtains directional information by interpreting the inclination of the magnetic field lines. The inclination compass is believed to be used by avians.

In particular the biophysical mechanism of the avian compass remains still unclear. Today two main theoretical models try to explain the magneto-reception mechanism. The first model is based on magnetized crystals which change the direction of their magnetization when interacting with the geomagnetic[41] field. These assumptions is supported by recent discoveries of magnetite (Fe_3O_4) particles in the upper beak of pigeons. These particles which act as small magnets can affect the signal carried by the opthalmic nerve, thus providing information for the magnetic field. The second and probably the most widely accepted theoretical model is based on the response of photo-activated chemical reactions to magnetic field. Radical pairs are a kind of such molecules whose fate is strongly determined by the surrounding magnetic field. They were proposed as magneto-receptors by Schulten [47].

QUANTUM DYNAMICS OF RADICAL PAIR REACTIONS

INTRODUCTION

Nowadays it is well known that the fate of a chemical reaction can be altered by the application of a magnetic field. Magnetic Field Effects (MFEs) are known to occure in a variety of ranges from a few μT up to a few Tesla [45]. MFEs were first observed in 1960s by Johnson [25] in the intensity of triplet-exciton annihilation luminescence in anthracene crystals. At the same time several other groups observed anomalous lineshapes and enchanced instensities in EPR signals, effects known as Chemically Induced Dynamic Electron or Nuclear Polarization (CIDEP or CIDNP respectively). All these unusual at that time phenomena could be explained by the so called Radical Pair Mechanism (RPM). Although the theoretical description of the Radical Pair dynamics exist since the 70's its underlying quantum dynamics have been questioned, leading to an intense scientific debate. In this chapter we will describe the dynamics of this kind of reactions and we will give the full master equation describing the quantum dynamics of the spin correlated Radical Pairs.

6.1 RADICAL PAIR MECHANISM

Radical Pairs (RPs) are created (Fig.6.1.1)from molecular dyad precursors by absorption of a photon and subsequent transfer of an electron from the one molecule, noted as Donor (D) to the other molecule, noted as Acceptor (A). Because of angular mo-
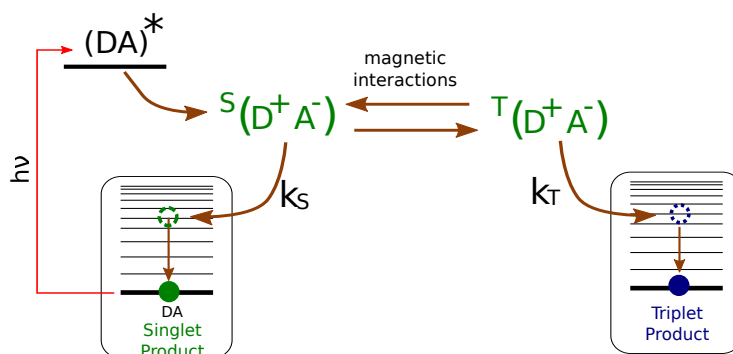
Photon absorption by the neutral molecular precursor and subsequent electron transfer creates the spin correlated radical pair.

Figure 6.1.1: Dynamics of the spin correlated RPs. The dyad precursor absorbs a photon. Electron transfer from the Donor molecule to the Acceptor molecule creates a spin correlated radical pair. The initial state of the RP is such that spin angular momentum in conserved. Due to magnetic interaction the state of the RP is inter-converted between Singlet and Triplet state. The coherent interconversion is interrupted from the recombination process, when the electron from the Acceptor is back transferred to the Donor and a neutral molecule is produced.

mentum conservation, the electronic spin of the RP is in the same state with the precursor. RPs can also be created from random encounters of free radical, but in this way the two spins are uncorrelated, contrary to the previous case of intermolecular electron transfer. In order to visualize the evolution of the RP spin state it is customary to represent the two electronic spins with vectors. The initial state of

the RPs may be Singlet[1] or Triplet[2]. The interaction of the RP with its surrounding magnetic environment or with externally applied fields, causes the electronic spin to evolve in time and therefore the RP state may change from Singlet to Triplet and vice versa. The magnetic environment main consist of the nuclear spins present in the side of the Donor or Acceptor. The evolution of the RP state is of major importance in spin chemistry since it determines the fate of chemical reactions. Two main mechanisms drive the evolution of the spins. The first originates from the hyperfine coupling of the electronic spins with the surrounding nuclei and the second due to different gyro-magnetic ratios of the two electrons. Moreover the evolution of the spins is governed by the recombination dynamics, that is the back electron transfer and the creation of neutral products. The production of neutral chemical products is determined by the state of the total electronic spin prior to recombination. If the RP

$$S=0 \qquad T_+=+1 \qquad T_-=-1 \qquad T_0=0$$
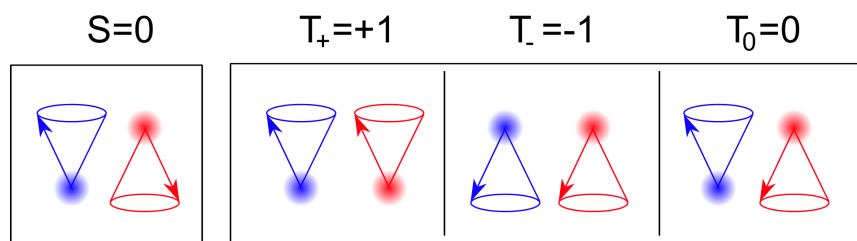
Figure 6.1.2: Vector Model of spin correlated RPs. In the left box the Singlet State (S = 0) is depicted while in the right box the three projections of the Triplet State (T = 1) along the quantization axis are shown.

was in the singlet (triplet) state then due to spin angular momentum conservation the products will also have spin S = 0 (S = 1). All the above are described by the schematic of Fig.6.1.1

The total quantum state state of the RP is described by a density matrix ρ containing the electronic and nuclear spin degrees of freedom. The general form of the Master Equation (ME) is

$$\frac{d\rho}{dt} = -i\,[H, \rho] + \mathcal{L}\,[\rho] \tag{66}$$

H, is the Hamiltonian describing the unitary evolution of the system due to the magnetic interactions and $\mathcal{L}\,[\rho]$ is the super-operator accounting for the recombination dynamics and any other relaxation processes.

6.2   THE HYPERFINE MECHANISM

In natural systems such as RPs the electrons are not isolated, they interact with a number of atoms like ^{1}H, ^{14}N, ^{1}D having non zero nuclear spins. Each unpaired electron is coupled with the nuclear spins by the hyperfine interaction. A simple way to understand the singlet-triplet mixing process is the vector model shown in Fig.6.2.1 [47]. The nuclear spins can thus be treated as classical vectors and each unpaired electron precesses around the local magnetic field produced by the neighboring nuclei. If each of the two electronic spins couples to a different magnetic environment then the local magnetic field produced by the hyperfine interactions is different and each spin will precess around at a different Larmor frequency. The Hamiltonian which describes the hyperfine interactions is

---

1 Singlet is the state at which the total electronic spin is zero (S = 0). In Dirac notation it is expressed as $|S\rangle = 1/\sqrt{2}\,(|\uparrow\downarrow\rangle - |\downarrow\uparrow\rangle)$
2 Triplet is the state at which the total electronic spin is zero (S = 1). The triplet state has three projections along the quantization axis defined, usually, by the magnetic fields axis. In Dirac notation it is expressed as $|T_0\rangle = 1/\sqrt{2}\,(|\uparrow\downarrow\rangle + |\downarrow\uparrow\rangle)$, $|T_+\rangle = |\uparrow\uparrow\rangle$ and $|T_-\rangle = |\downarrow\downarrow\rangle$
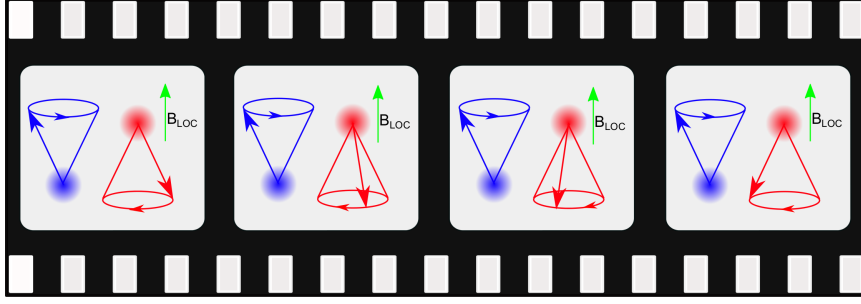
Figure 6.2.1: Evolution of the total spin of the RP due to the hyperfine interaction of the electronic spins with the adjacent nuclei. The electronic spin on the right(red) presses around the magnetic field produced by the nearby nuclei In this figure only the right(red) radical is surrounded with nuclear spins which produce a local magnetic field B_{LOC}.

$$H_{HFC} = \left(\sum_k \mathbf{I}_k \cdot \alpha_k \cdot \mathbf{S}_1 \right) + \left(\sum_m \mathbf{I}_m \cdot \alpha_m \cdot \mathbf{S}_2 \right) \tag{67}$$

where $\alpha_k (\alpha_m)$ is the hyperfine coupling tensor and the sum over k(m) represent the contributions of all the nearby nuclear spins of the Donor (sum over k) and the acceptor (sum over m). The hyperfine coupling tensor is usually described by a 3×3 matrix, but in this work we only consider hyperfine coupling tensors with zero of diagonal elements. Thus α_k is given by:

$$a_k = diag\{a_{xx}, a_{yy}, a_{zz}\} \tag{68}$$

In the case of isotropic hyperfine coupling tensor ($\alpha_{xx} = \alpha_{yy} = \alpha_{zz} = \alpha$), one more simplification is possible. As shown in [48] Eq.67 can be replaced by

$$H_{HFC} = \left(\bar{\alpha}_1 \sum_k \mathbf{I}_k \cdot \mathbf{S}_1 \right) + \left(\bar{\alpha}_2 \sum_k \mathbf{I}_k \cdot \mathbf{S_2} \right) \tag{69}$$

In this equation (Eq.69) the hyperfine coupling constant α (Eq.69) is the effective hyperfine coupling constant

$$\bar{\alpha} = \sqrt{\frac{4}{3} \sum_i \bar{\alpha_i^2} I_i (I_i + 1)} \tag{70}$$

and comes from the ensemble averaging of N random vectors of length $\alpha_i \sqrt{I_i(I_i + 1)}$.

6.3 ZEEMAN INTERACTION AND THE δG MECHANISM

The interaction of the unpaired electron of each RP with an externally applied magnetic field is described by the Zeeman interaction. The relevant Hamiltonian term is[3]

$$H_Z = \mu_B \mathbf{B} \cdot (g_1 \cdot \mathbf{S}_1 + g_2 \cdot \mathbf{S}_2) \tag{71}$$

In the general case the g-factor, is a tensor described by a 3×3 matrix. The same simplification done for the hyperfine interaction, is also done here, i.e the g-tensor is a diagonal matrix and moreover it is isotropic

$$g_k = diag\{g_{xx}, g_{yy}, g_{zz}\} = g \tag{72}$$

Usually the difference in the g-factors ($\Delta g = g_2 - g_1$) is on the order of 10^{-3} or less. In this case the Larmor frequencies the two electronic spins are practically equal.

---

[3] the magnetic field also couples to the nuclear spin, but since the nuclear gyromagnetic ration is much smaller then the electronic it can be safelly omitted.

The difference in the g−factors of the electronic spin induces Singlet-Triplet interconversion, which is observable at high magnetic fields

45

Henceforth since MFE in RPs are studied in low magnetic fields and the two spins precess with practically the same frequency, no significant Singlet - Triplet mixing is expected. In order for efficient Singlet Triplet mixing to occur the Larmor frequencies of the two spins should differ significantly. This is the case in high magnetic fields because the difference in precession frequencies is proportional to the magnetic field strength $\Delta\omega = \Delta g \mu_B / \hbar$.

6.4 EXCHANGE INTERACTION

The spin exchange interaction shifts the energy degeneracy of the singlet and triplet levels and thus affects the interconversion dynamics

The full treatment of RP dynamics requires the that one should take into account the electron exchange interaction. The spin exchange Hamiltonian in described by

$$H_{EX} = J \left(\frac{1}{2} + 2\mathbf{S}_1 \cdot \mathbf{S}_2 \right) \tag{73}$$

the parameter J represents the coupling and is a function of the inter-radical separation ($J = J_0 e^{-r/r_0}$). The exchange interaction is crucial in RP dynamics because it determines the energy separation between the Singlet and Triplet states and thus it affects the possibility of Singlet-Triplet mixing.

TOTAL HAMILTONIAN   The total interaction describing the dynamics of the RP will be the sum of the hyperfine interaction Hamiltonian, the Zeeman Hamiltonian and the spin exchange Hamiltonian:

$$H_{mag} = H_{HFC} + H_Z + H_{EX} \tag{74}$$

6.5 RECOMBINATION DYNAMICS

Since the advent of Spin Chemistry the dynamics of the RP reactions are described by a semi-classical master equation

The evolution of the spin state of the radical pair was described, since the origin of spin chemistry, by the following master equation which hereafter will be called traditional [16] (TME)

$$\frac{d\rho}{dt} = -i\left[H_{mag}, \rho\right] - \frac{k_S}{2}\left(\rho \cdot Q_S + Q_S \cdot \rho\right) - \frac{k_T}{2}\left(\rho \cdot Q_T + Q_T \cdot \rho\right) \tag{75}$$

The form of this equation is compatible with that of Eq.66 and $\mathcal{L}\left[\rho\right] = -\frac{k_S}{2}\left(\rho \cdot Q_S + Q_S \cdot \rho\right) - \frac{k_T}{2}\left(\rho \cdot Q_T + Q_T \cdot \rho\right)$. The parameters k_S and k_T are the rates at which recombination events occur. The operators Q_S and Q_T are projection operators onto the Singlet and Triplet state respectively and are given by

$$Q_S = \frac{1}{4}\mathbb{1} - \mathbf{S}_1 \cdot \mathbf{S}_2 \tag{76}$$

$$Q_T = \frac{3}{4}\mathbb{1} + \mathbf{S}_1 \cdot \mathbf{S}_2 \tag{77}$$

It should be noted that $Q_s + Q_T = 1$ which means that the RP is either on the Singlet or the Triplet State before a recombination event occurs.

DIMENSIONS OF THE HILBERT SPACE   The dimensions of the density matrix and in general of any operator acting in the RP spin space are determined by the spin multiplicity of the two electrons and the multiplicity of the nuclear spin at the site of the donor and the acceptor:

$$\begin{aligned} dim\left[\mathcal{O}\right] &= (2\frac{1}{2} + 1) \times (2\frac{1}{2} + 1) \times \\ &\times \prod_k (2I_{D,k} + 1) \times \prod_m (2I_{A,m} + 1) \end{aligned} \tag{78}$$

with $I_{D,k}$ and $I_{A,m}$ being the the kth and m^{th} nuclear spin residing at the donor and acceptor molecule respectively. Usually it is good enough an approxiamtion to consider that only one nuclear spin exists near each molecule.

Although the traditional ME successfully described RP reactions, it recently became clear that in masks quantum coherence effects. The first fully quantum mechanical treatment of RR reactions and specifically of the recombination dynamics was done by [30]. In the following we will reproduce the derivation of the Quantum Mechanical Master Equation (QMME) as was given in [30, 33].

The Traditional ME masks the quantum mechanical effects which are revealed in modern experiments
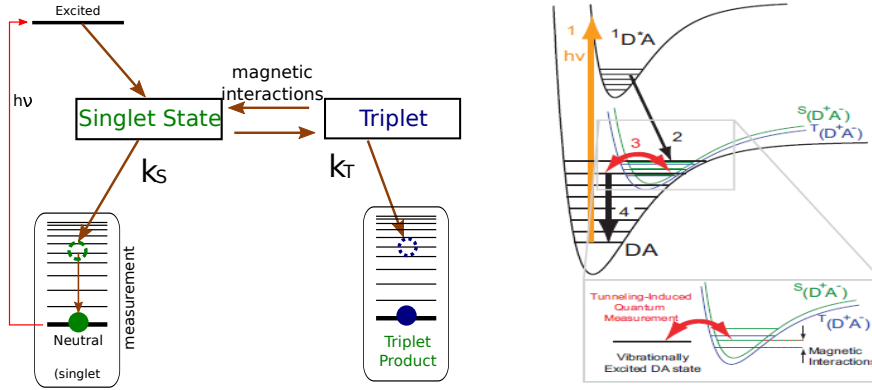
Figure 6.5.1: Left: A schematic of the RP reaction dynamics. A photon excites the neutral molecular with subsequent electron transfer from the donor molecule to the acceptor. The magnetic interaction of the unpaired electrons with the nuclear spins and the external magnetic fields bring about the coherent Singlet Triplet mixing
Right: Level structure and recombination dynamics of the RP taking place in four steps: (1) photoexcitation, (2) radical-ion-pair creation, (3) tunneling-induced quantum measurement of the pair's spin state and (4) final decay to the ground state. Only the singlet reservoir of vibrationally excited states of the neutral molecule DA is shown for simplicity. Another such reservoir exists for the triplet chemical products.

The molecule is excited by absorbing a photon. Subsequent the electron transfer creates the radical pair. In the schematic shown in Fig.6.5.1 the RP is created in the Singlet state. This state is not an eigenstate of the Hamiltonian of Eq:74 and therefore Singlet Triplet mixing occurs. A tunneling event into a vibrational excited state of the neutral molecule terminates the coherent procedure. The recombined molecule then decays to the ground state and new photon initiated RP reaction begins. RP in the Singlet state will tunnel to the reservoir of singlet excited vibrational states, the same holds for the RPs in the Triplet state. The annihilation (creation) operator for the Singlet and Triplet state are $\alpha(\alpha^\dagger)$ and $b(b^\dagger)$ respectively and the corresponding Hamiltonian is

A tunneling event into a vibrational excited state of the neutral molecule terminates the coherent procedure and creates a neutral molecule.

$$H_{res} = \sum_\alpha \omega_\alpha \alpha\alpha^\dagger + \sum_b \omega_b bb^\dagger \tag{79}$$

The Hamiltonian of the RP in Singlet Triplet subspace, that is prior to recombination is

$$H_{RP} = cc^\dagger(\epsilon + H_{mag}) \tag{80}$$

where ϵ is the energy of the RP with respect to the ground state of the neutral atom, H_{mag} is the magnetic Hamiltonian given in Eq.74 and c ($c^\dagger$) is the annihilation (creation) operator of the unpaired electron. When $\langle cc^\dagger \rangle = 1$ the RP is still in the Singlet Triplet subspace, whereas when $\langle cc^\dagger \rangle = 0$ the RP has recombined. At last the tunneling Hamiltonian is

$$H_{tun} = \sum T_\alpha c\alpha^\dagger Q_S + \sum T_b cb^\dagger Q_T + c.c \tag{81}$$

The first term means that if the RP is in the Singlet State it can recombine reducing the RP occupation number to zero and creating an occupied vibrational state. Similar

is the explanation for the second term. After applying second order perturbation theory (the interested reader may refer to [30] for an analytical description of the procedure) th ME equation describing the evolution of the RP reads

$$\frac{d\rho}{dt} = -i\left[H_{mag}, \rho\right] - \frac{k_S + k_T}{2}\mathcal{D}\left[Q_S\right]\rho \tag{82}$$

$$\mathcal{D}\left[\mathcal{O}\right]\rho = \rho\mathcal{O} + \mathcal{O}\rho - 2\mathcal{O}\rho\mathcal{O}^\dagger \tag{83}$$

The resulting ME (Eq.82) is in the Lindblad form as it should since a fully quantum mechanical treatment was followed. Thus it should be emphasized that the recombination process is indeed a quantum measurement process continuously interrogating the RPs spin state. This ME (Eq.82) correctly describes the evolution of the RP until it reacts. This is certified by the fact that Eq.82 is trace preserving[4]. But one needs to model the chemical reaction i.e the disappearance of the RP and the creation of the neutral molecule. In a time interval dt the RPs having recombined from the Singlet channel will be $dn_S = k_S dt Tr\left\{\rho Q_S\right\}$ and the RPs having recombined from the Triplet channel will be $dn_T = k_T dt Tr\left\{\rho Q_T\right\}$. The observation of dn_S singlet products does not mean that the RP was in the singlet state prior the recombination event. It could have been as well to a linear combination of the Singlet and triplet state $|\psi\rangle = \alpha|S\rangle + \beta|T\rangle$. This state is described by the density matrix $\rho = |\psi\rangle\langle\psi| = |\alpha|^2|S\rangle\langle S| + |\beta|^2|T\rangle\langle T| + \alpha\beta^*|S\rangle\langle T| + \alpha^*\beta|T\rangle\langle S|$. To correctly account for the reaction kinetics and correctly update the density matrix of the remaining RP Kominis (REF) defined a measure of coherence

$$p_c = \frac{Tr\left\{\rho_{ST}\rho_{TS}\right\}}{Tr\left\{\rho_{SS}\right\}Tr\left\{\rho_{TT}\right\}} \tag{84}$$

$$\rho_{AB} = Q_A\rho Q_B$$

When the RP is in a maximally coherent state, $p_c = 1$ and in the other extreme case of minimum coherence $p_c = 0$. If the state of the RP at time t was ρ_t, then at time $t + dt$ it will be $\rho_{t+dt} = \rho_t + d\rho$. At [33] it was shown that $d\rho$ depends on the state of the RP at time t. For the general case it was shown that the master equation describing the spin selective recombination dynamics are

$$\frac{d\rho}{dt} = \left(\frac{d\rho}{dt}\right)_{nr} -(1 - p_c)\left(k_S Q_S\rho Q_S + k_T Q_T\rho Q_T\right)$$
$$-p_c\left(k_S Tr\left\{Q_S\rho\right\} + k_T Tr\left\{Q_T\rho\right\}\right)\frac{\rho}{Tr\left\{\rho\right\}} \tag{85}$$

where $\left(\frac{d\rho}{dt}\right)_{nr}$ is given by Eq.82

6.5.2 *Other proposed Master Equations*

The theoretical work of [30] and [33] have triggered a still ongoing debate about the proper description and theoretical framework of RPs evolution and recombination dynamics

1. In order of appearance Jones & Hore [26] have produced a different ME for ρ, conjecture to follow from quantum measurement theory. This equations reads

$$\frac{d\rho}{dt} = -i\left[H_{mag}, \rho\right] -k_S\left(\rho Q_S + Q_S\rho - Q_S\rho Q_S\right)$$
$$-k_T\left(\rho Q_T + Q_T\rho - Q_T\rho Q_T\right) \tag{86}$$

2. Shushin [49] argued that the decoherence induced by the quantum measurement and the quantum dynamics of the RP reactions are not a new concept and that are already included in the Bloch-Redfield theory of relaxation. Thus no new concept from quantum measurement theory is needed.

---

4 It is very interesting to note that Haberkorn found a similar result and described this case as *relaxation without reaction*

3. Ivanov *et. al.* [24] and Purtov [42] derive the Traditional ME of RP reactions from first principle assuming that the RP quantum state and the neutral product quantum state are eigenstates of the same Hamiltonian and that transitions are induced between them by some perturbation.

6.6 PRODUCT YIELD

What is usually observed and measured in RP reactions is the number of neutral molecules having recombined from the singlet or the triplet state. The percentage of RPs recombined from the singlet recombination channel in a time interval and accumulated in the ground state of the same spin multiplicity is the Single Yield and is defined as:

Yield is the number of recombined RPs accumulated in the ground state of the molecule

$$Y_S = \int_0^\infty k_S \langle Q_S \rangle_t \, dt \tag{87}$$

where $\langle Q_S \rangle_t = \mathrm{Tr} \{ \rho(t) \cdot Q_S \}$ and $\rho(t)$ is given by Eq.85. The Triplet Yield Y_S is defined in a similar way

$$Y_T = \int_0^\infty k_T \langle Q_T \rangle_t \, dt \tag{88}$$

EXPERIMENTAL PROPOSAL FOR THE DISCRIMINATION AMONG THEORIES OF SPIN SELECTIVE RADICAL PAIR REACTIONS

7.1 INTRODUCTION

The master equation describing the reaction dynamics of the RPs has to be able to reproduce:

- the unitary evolution of ρ due to the magnetic interactions within the RPs
- the loss of RPs due to the recombination reaction leading to the creation of neutral products and
- the state change of unrecombined RPs

The perplexity of the combined presence of all those phenomena is partly the reason behind the ongoing debate on the particular form of this master equation. The current standing of this debate is the following. Kominis derived [30] a master equation for the unrecombined RPs and put forward a master equation [33] for the reaction term (ii). Another master equation was introduced by Jones and Hore [26], while several authors [24, 42, 49] argued in favor of the traditional master equation of spin chemistry. So the same physical system is currently described by three theories. This situation is clearly unsatisfactory, and although theoretical arguments could in principle point to the fundamentally correct theory [34, 27, 31], the need for an experiment with discriminatory power is obvious. We will here propose exactly such an experiment. In this chapter we propose a concrete experimental test that can clearly discriminate among the fundamental master equations currently attempting to describe the quantum dynamics of these reactions. The proposed measurement based on photon statistics of fluorescing radical pairs is shown to be molecular-model-independent and capable of elucidating the Singlet–Triplet decoherence inherent in the RP recombination process.

7.2 STRESSING THE FUNDAMENTAL DIFFERENCES BETWEEN PROPOSED THEORETICAL MODELS

It would be very useful in order to present our arguments to stress the fundamental differences between the three proposed theoretical models aiming to describe the dynamics of the RP reactions. First of all we can rewrite all three different MEs in such a way that a straight forward comparison is available.

$$\frac{d\rho}{dt} = -i\left[H_m, \rho\right] - \frac{k_S - k_T}{2}\mathcal{D}\left[Q_S\right]\rho$$
$$\qquad -\left[\left(k_S - k_T\right)Q_S\rho Q_S + k_T\rho\right] \quad \text{(Traditional ME)} \tag{89}$$

$$\frac{d\rho}{dt} = -i\left[H_m, \rho\right] - \left(k_S + k_T\right)\mathcal{D}\left[Q_S\right]\rho$$
$$\qquad -\left[\left(k_S - k_T\right)Q_S\rho Q_S + k_T\left(\rho - \mathcal{D}\left[Q_S\right]\rho\right)\right] \quad \text{(Jones \& Hore ME)} \tag{90}$$

$$\frac{d\rho}{dt} = -i\left[H_m, \rho\right] - \frac{k_S + k_T}{2}\mathcal{D}\left[Q_S\right]\rho$$
$$\qquad -\left(1 - p_c\right)\left[\left(k_S - k_T\right)Q_S\rho Q_S + k_T\left(\rho - \mathcal{D}\left[Q_S\right]\rho\right)\right]$$
$$\qquad -p_c\left[\left(k_S - k_T\right)\frac{\langle Q_S \rangle}{N_{RP}} - k_T\right]\rho \quad \text{(Kominis ME)} \tag{91}$$

where $\mathcal{D}\left[Q_S\right]\rho = \rho Q_S + Q_S\rho - 2Q_S\rho Q_S$ and $N_{RP} = Tr\left\{\rho\right\}$ is the population of the unrecombined RPs. From the above equations it is obvious that one can find certain regimes of parameters that all the equations give qualitatively equal results. For example when $k_T = 0$ then the "Traditional" and the "Jones & Hore" ME are the same,

there are certain regimes of parameters that all the equations give qualitatively same results

except that the rate multiplying the first term is different. Similarly when $k_S = k_T$ the "Jones & Hore" and the "Kominis" MEs have a similar forms, except that some multiplication factors are again different. One can make several theoretical arguments in favor of the one or the other master equation and in principle these arguments may point to the fundamental correct theory. In the rest of this section we will stress some of these arguments. Nevertheless it is obvious that there is an indispensable need for an experiment that could clearly discriminate between theories

7.2.1 *The Jones & Hore Theory fails to describe Single Molecule Experiments*

The philosophy under the derivation of the Jones & Hore theory is that the detection of a particular reaction product during the time interval dt, affects the evolution of the quantum state of the remaining unrecombined molecules. Specifically if $k_T dt$ molecules react and produce triplet products this will have an impact on the unrecombined molecules by projecting them to a more singlet state because the density matrix acquires the term $k_T Q_S \rho Q_T$. In other words the authors treat the recombined products and the RPs in the singlet triplet subspace as being in an entangled state. This is not the case because in RP reactions the quantum measurement performed by the reservoirs is internal in each molecule and cannot affect the entire population of RPs.

7.2.2 *Conceptual problems in Traditional Master Equation*

The physical background under the Traditional ME as has been shown by Ivanov [24] and Purtov [42] is that the state of the RPs prior to recombination and the state of the neutral products are eigenstates of the same Hamiltonian and that transitions are induced by a perturbation. This statements can be rephrased that RP in the Singlet Triplet subspace and the reaction products are in quantum superposition, despite the fact that the chemical reaction is irreversible.

7.3 PROPOSED EXPERIMENT

There is need for an experiment able to clearly prove the validity of the proposed MEs

an experiment able to measure the decoherence rate induced by interrogating the RP's state by the singlet or triplet reservoir could in principle be a useful tool

An experiment able to clearly distinguish among the valid theoretical model is indistinguishable. In the majority of the experiments done so far, the measured quantity is proportional to the probability of finding the RP in the Singlet ($\langle Q_S \rangle$) or Tiplet state ($\langle Q_T \rangle$). It is easily to prove that this quantity is different depending on the ME being used to evaluate the result. However in practice it would be difficult for an experiment to discern the absolute differenced in the singlet (or triplet) probability or in the magnetic field effect (MFE) signal. To overcome this problem the measured quantity should give clear results. Such a quantity is the singlet triplet coherence. In all three ME the mechanism leading to decoherence and the rate at which coherence is reduced are completely different. In the Jones & Hore ME the decoherence rate is twice as that predicted by the Kominis ME. We note here that the term describing the decoherence is $\mathcal{D}[Q_S]\rho = Q_S\rho + \rho Q_S - 2Q_S\rho Q_S$. Thus an experimental measurement able to measure the decoherence rate induced by interrogating the RP's state by the singlet or triplet reservoir could in principle be a useful tool. The time evolution of the probability of finding a RP in the triplet state a time t is depicted in Fig.7.3.1 As expected this probability is not constant but oscillates in time. This is a characteristic of the singlet triplet interconversion induced by the hyperfine interactions are due to the Δg mechanism as described in previous chapter. The simulation considered here was done assuming that both RP were surrounded by the same environment of nuclear spins and thus the only mechanism respnsible for singlet triplet mixing is the Δg mechanism. Moreover besides the coherence mixing what one can observe is the recombination dynamics. Thus in addition to the oscillations a continuous decrease in the amplitude of the probability is also shown. In Fig.7.3.1
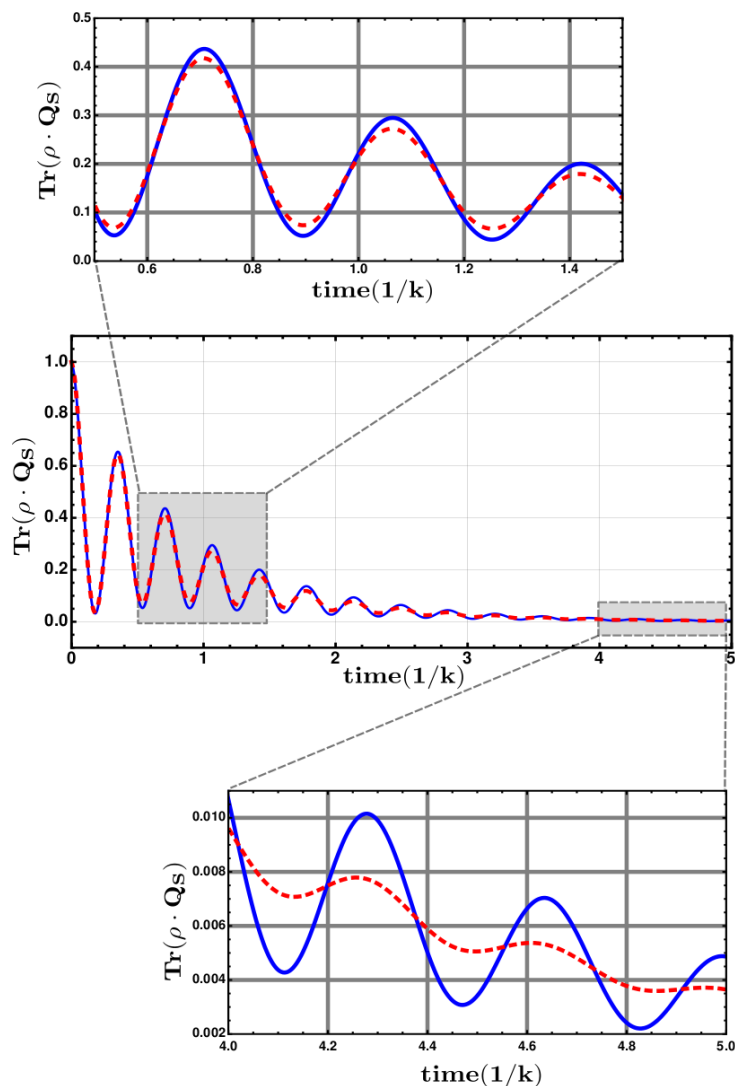
Figure 7.3.1: Time evolution of the singlet probability, $\langle Q_S \rangle$ for the radical pairs, calculated with the Kominis ME (blue line) and with the Jones & Hore ME (red dashed line) for $B = 5 \times 10^3 G$, $k_S = k_T = 2.5$MHz, $\Delta g = 10^{-3}$ and without any hyperfine coupling interactions. It is clearly shown that although the absolute value of $\langle Q_S \rangle$ is almost identical in both simulations, the slope of $\langle Q_S \rangle$ which is a measure of the singlet triplet coherence is dramatically different and the decay rate predicted by Jones & Hore ME is almost twice as the decay rate predicted by Komins ME

we simulate the reaction dynamics by using two different ME: (i) the one proposed by Kominis and (ii) the one proposed by Jones & Hore. This is done in order to emphasize that although the different models may give different absolute values the quantitative behavior of the $\langle Q_S \rangle$ is similar and thus it is difficult to make any claim about the validity of a ME. On the other hand what is clearly visible from Fig.7.3.1 is that the slope $d\langle Q_S \rangle/dt$ is completely different in this example. Obviously the slope $d\langle Q_S \rangle/dt$ is maximum between the peaks and troughs $\langle Q_S \rangle$. At these points, where the slope is maximized, the state of the RP is characterized by maximum coherence. The source of quantum coherence is the first term of Eq.89-91. On the other hand the term accounting for the decoherence is the second term of the same set of equations

and at least for Eq.90 and Eq.91 it is clear the decoherence rate is double in the first case than in the second.

7.3.1 *RP model considered*

The RP model considered for the simulation of the experiment is shown in Fig.7.3.2. As usual the neutral atom in the ground state absorbs a photon and through subsequent electron transfer a RP at the Singlet electron state is produced. The Singlet-Triplet mixing is induced by the Δg mechanism. In our model we consider RPs with different g-factors and we apply a high magnetic fields such that the the Singlet Triplet mixing is dominated by the difference at g-factors. Thus we can safely omit the hyperfine coupling contribution to the interconversion procedure. We are assuming that each recombination event is accompanied by an emission of a photon (Fig.7.3.2) The probability to observe n_t photons in the time interval between
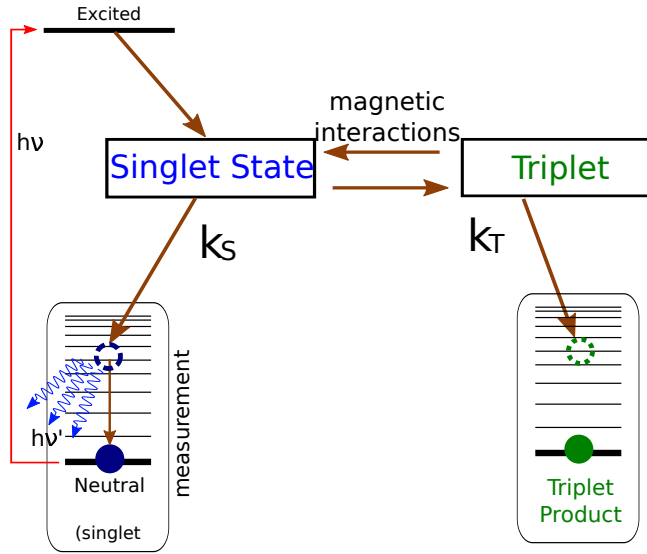
Figure 7.3.2: Radical-pair system considered for the simulation of the proposed experiment. Photo-excitation of a donor-acceptor molecule DA followed by charge-transfer creates a radical-ion-pair.The Zeeman interaction of the two unpaired electrons with the external magnetic field and due to the Δg mechanism induce a coherent singlet-triplet conversion, ceased by the spin-selective charge recombination, which transforms singlet (triplet) radical-ion pairs into singlet (triplet) neutral products at a rate k_S (k_T). The neutral product of the singlet state occupies an excited state of the reservoir and then by photon emission it returns to ground neutral state.

$\{t, t + dt\}$ is given by the Poisson distribution and has a mean value $N_t = k_s dt \langle Q_S \rangle$[1]. The detection of photons is a stochastic process, described by Poisson statistics and what we are interested in is the difference of two Poisson processes at subsequent time intervals $\{t, t + dt\}$ and $\{t + dt, t + 2dt\}$ having meas values

$$
\begin{aligned}
N_t &= k_S dt \langle Q_S \rangle_t \\
N_{t+dt} &= k_S dt \langle Q_S \rangle_{t+dt}
\end{aligned}
$$

---

1 a reasonable assumption to make is that the the emission of the photon, determined by the life time of the neutral molecule in the excited vibrational state, is much faster than the recombination rate $\Gamma \gg k$

The difference of two such processes follows the Skellam distribution. According to the Skellam distribution the probability that $n_t - n_{t+dt} = \delta n$ is given by

$$F(\delta n; N_t, N_{t+dt}) = e^{N_t + N_{t+dt}} \left(\frac{N_t}{N_{t+dt}} \right)^{k/2} I_{|k|} \left(2\sqrt{N_t N_{t+dt}} \right) \qquad (92)$$

$I_{|k|}$ is the modified Bessel function of the first kind. In the Skellam distribution the mean is given by

$$mean = N_t - N_{t+dt} \qquad (93)$$

and the uncertainty in the estimation of the mean is given by variance defined by

$$var = N_t + N_{t+dt} \qquad (94)$$

The measure quantity in our proposal is the mean value, normalized by the probability of detecting n_t photo-counts at time t. Thus the detected signal and the respective uncertainty are

$$\mu = \frac{N_t - N_{t+dt}}{N_t} \qquad (95)$$

$$\sigma = \frac{\sqrt{N_t + N_{t+dt}}}{N_t} \approx \sqrt{\frac{2}{N_t}} \qquad (96)$$

the simplification at the second line of Eqs.95 is done because the mean values N_t and N_{t+dt} are almost equal ($N_t + N_{t+dt} \approx N_t$).

What is the physical meaning of μ and its decay? It is easily seen from Eq.95 that the $\mu = d \langle Q_S \rangle_t / \langle Q_S \rangle_t$, where $d \langle Q_S \rangle_t = \langle Q_S \rangle_{t+dt} - \langle Q_S \rangle_t$. Obviously μ is maximum when the slope $d \langle Q_S \rangle_t / dt$ is maximum. This property makes μ a proper measure of singlet triplet coherence. In Fig.7.3.3 we plot the value of μ versus time according to the three frequencies. In the same figure the value of σ is also calculated. The uncertainty σ in the measured quantity should be much lower than the value of the quantity itself in order to allow a statistical meaningful comparison between the data and the theoretical expectation. The simulations were done assuming that the magnetic field was large enough so that only the Δg mechanism is responsible for Singlet Triplet interconversion. We also neglected any other interactions such as spin exchange and dipolar interactions. The Hamiltonian of the system is thus $H = \omega_1 S_{1z} + \omega_2 S_{2z}$ where the the larmor frequencies ω_j are not equal due to the difference in the g-factors. In this example under study we took $\Delta g = 2 \times 10^{-3}$ and $\omega_1 \approx \omega_2 = (4 \times 10^3)k$.

μ is proportional to $d \langle Q_S \rangle_t / dt$ and thus is a proper measure of singlet triplet coherence.

7.3.2 *Loss of Singlet Triplet coherence*

The ME of Jones & Hore is given in Eq.90. This equation follows from the one Kominis derived (Eq.91) by setting $p_c = 0$ and doubling the Singlet Triplet decoherence rate $((k_S + k_T)/2)$. The fact that the quantity $Q_S \rho + \rho Q_S - 2Q_S \rho Q_S$ represents Singlet - Triplet coherence can be easily shown rather generally. Multiplying ρ from left and right by $\mathbb{1} = Q_S + Q_T$ it follows that ρ can be written as $\rho = \bar{\rho} + \tilde{\rho}$, where $\bar{\rho} = Q_S \rho Q_S + Q_T \rho Q_T$ is the incoherent and $\tilde{\rho} = Q_S \rho Q_T + Q_T \rho Q_S$ is the coherent part of ρ. It is easily seen that $Q_S \rho + \rho Q_S - 2Q_S \rho Q_S = \tilde{\rho}$, proving the above claim. The magnetic Hamiltonian is the generator of Singlet - Triplet coherence. The steady state S–T coherence is determined by its generation rate through H and its dissipation rate through the second term in the master Eqs(91,90). Because Singlet - Triplet coherence decays at double the rate in the Jones & Hore theory than in Kominis' theory, it is seen that the steady state of Singlet - Triplet coherence (oscillation amplitude of l) quickly approaches zero in the former, and a non-zero value in the latter.

Singlet - Triplet coherence decays at double the rate in the Jones & Hore theory than in Kominis' theory

7.3.3 *Experimental Implementation*

The proposed experiment can be realized in RPs at which quantum beats arising form the coherent oscillation between the singlet and triplet states can be observed,
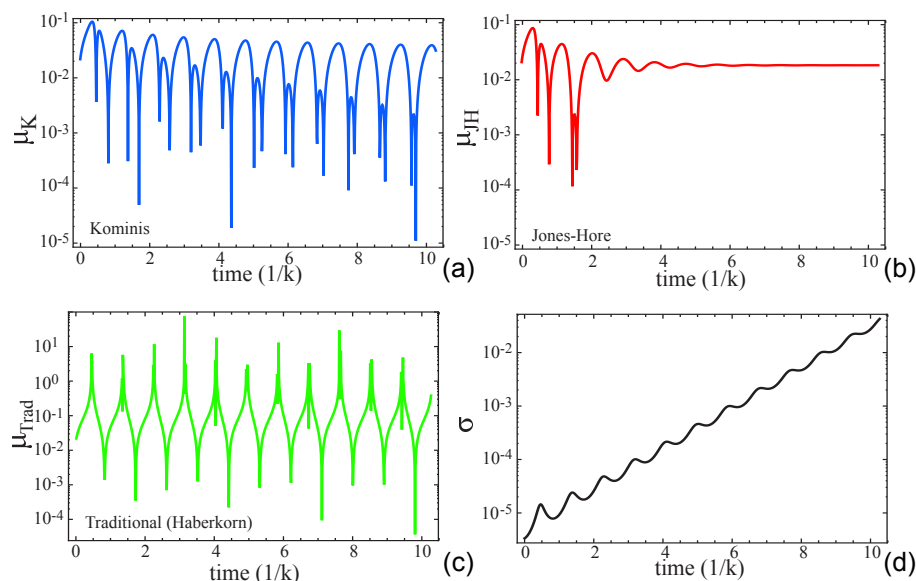
Figure 7.3.3: We numerically integrate the three master equations for a magnetic Hamiltonian of the form $H = \omega_1 S_{1z} + \omega_2 S_{2z}$. The two Larmor frequencies are proportional to the respective g-factors, and we took $\Delta g = 2 \times 10^{-3}$, and $\omega_1 \approx \omega_2 = (4 \times 10^3)k$, whereas $\omega_1 - \omega = 8k$. We plot μ, for the (a) Kominis, (b) the Jones–Hore and (c) the traditional (Haberkorn) theory. For σ, the statistical error plotted in (d), to be small enough to allow a statistically meaningful comparison between data and theoretical expectation, we chose an initial number of RPs 10^{13} and we calculate the expected photon counts in a time interval Δt from $N_t = k_S \int_t^{t+\Delta t} \langle Q_S \rangle \, dt$, where $\Delta t = 0.006/k$.

as for example in transient-EPR experiments [35]. Interestingly, RPs which also recombine with a concomitant photon emission or even absorption have been extensively studied e.g. by Molin [37], although these studies have the additional complication of RP diffusion, absent from the simple model of a fixed dyad considered here. An additional complication is the decay rate of the fluorescing exciplex mentioned earlier. If RPs accumulate in a slowly decaying exciplex (i.e. $r \ll k_S$) then quantum beats will be hardly observable. Moreover, there are solid state systems which could be used for the purpose of the proposed experiment. For example, in the P^+I^- RP found in photosynthetic reaction centers [REF 24,25 from paper], the triplet recombination results in the formation of ^3P molecules which can absorb 870nm photons. The absorption (and thus at latter times the emission) statistics of these photons carry information similar to what is considered here. A final point has to do with spin relaxation. The difference between the predictions of the various theories will fade away if other spin-relaxation mechanisms are dominant beyond the fundamental S–T decoherence process inherent in the recombination process of RPs. The physical origin of this decoherence process has been exhaustively explained in [30, 33, 34]. Additional relaxation mechanisms can in principle be suppressed, e.g. by performing the measurement at low enough temperatures. There exist several experiments where such relaxation channels appear to be slower than the recombination rates, as for example the ones reported in [54, 36].

Other relaxation mechanisms which will minimize the difference between the predictions can be suppressed by performing the measurement at low temperatures

7.4 CONCLUSIONS

We stress that the particular measurement we propose is model-independent, in the following sense. Clearly the time evolution of observables like $\langle Q_S \rangle$ or the magnetic-
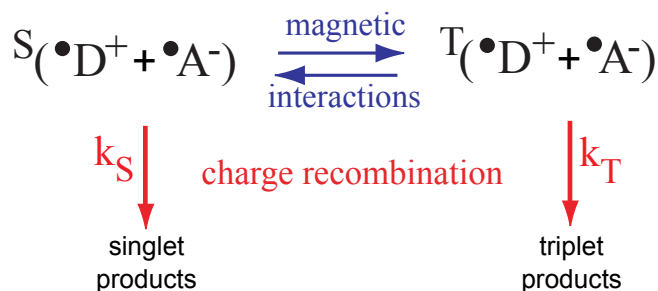
field effect (MFE) are predicted to be different by the three theories. However, in practice it would be difficult for the measurement to discern absolute differences in $\langle Q_S \rangle$ or the MFE signal, since it would be possible to attribute those to an imperfect understanding of e.g. the RP's magnetic interactions. In contrast, in the measurement we propose, normalizing the photon count difference by N_t and measuring at high enough magnetic fields where the S–T mixing is dominated by Δg, largely alleviates this problem, and the three theories predict clearly distinguishable trends, no matter what the details of the molecular interactions are.

THE BENEFITS OF QUANTUM ZENO EFFECT IN MAGNETIC AND ANGULAR SENSITIVITY OF THE AVIAN COMPASS

INTRODUCTION

It has been already mentioned that the chemical fate of the RP reactions is strongly determined by the external magnetic fields. A schematic of the reaction is shown in Fig.8.0.1 Recently it has been suggested and shown by theoretical simulations

$$^S(\bullet D^+ + \bullet A^-) \xrightleftharpoons[\text{interactions}]{\text{magnetic}} \ ^T(\bullet D^+ + \bullet A^-)$$

$$k_S \downarrow \quad \text{charge recombination} \quad \downarrow k_T$$

singlet   triplet
products   products

Figure 8.0.1: Radical-ion-pair reaction dynamics: Photoexcitation of a donor-acceptor molecule DA followed by charge-transfer creates a radical-ion-pair, i.e. two molecular ions and two unpaired electrons (two dots). The Zeeman interaction of the two unpaired electrons with the external magnetic field and hyperfine interactions with the molecule's magnetic nuclei induce a coherent singlet-triplet conversion, ceased by the spin-selective charge recombination, which transforms singlet (triplet) radical-ion pairs into singlet (triplet) neutral products at a rate k_S (k_T).

by[44] that magnetic fields of geomagnetic field strength or even weaker can produce changes in the reaction yields of the singlet and triplet state. In the same study cryptochrome was proposed as a candidate molecule for magneto-reception. Several other studies came to uphold this suggestion and there are evidences that photosensitive chemical reactions take place in the retina of some avian species. An indispensable requirement for the RPs to fuctions as magnetic sensor and in general for any system to act as a magnetic compass is to respond not only to the magnitude of the detected magnetic field but also to its direction. This is accomplised only if the RPs are immobilized and ordered. Magnetic field effects on chemical reactions have been well studied and documented since the origin of spin chemistry. Although in nature the real systems are very complicated and difficult to study, several assumpltions can be made, depending on the conditions and the effects one needs to study in oder to simplify the system. Usually, in RP reactions the hyperfine coupling tensor is taken to have only diagonal elements, the recombination rates are considered to be equal and no spin spin interactions between the radicals are considered. This last assumption was the subject of a thorough study by [12] and led to a proposal about the conditions that spin exchange and dipolar coupling have to fulfill in order to function as a compass.
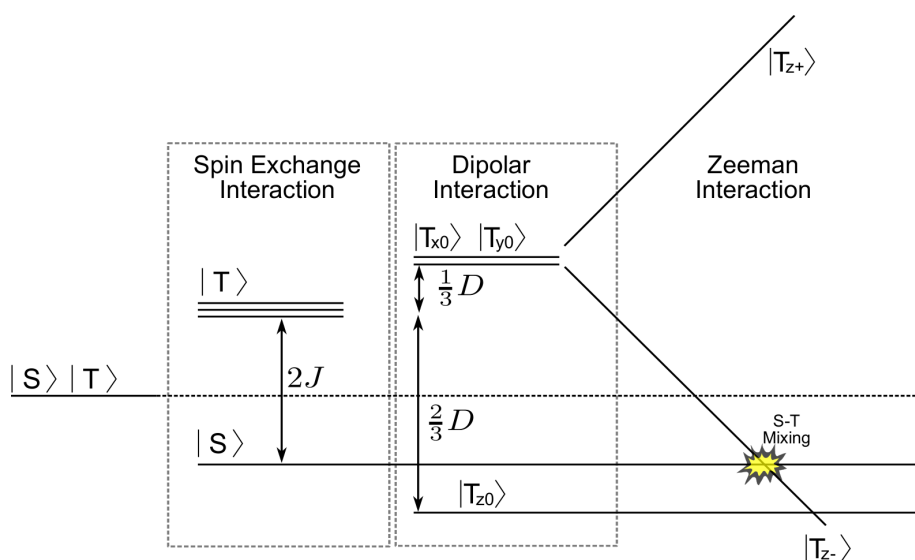
Photosensitive chemical reactions taking place in the retina of some avian species may lead to the creation of molecules responsible for avian magnetoreception

8.1 SPIN EXCHANGE INTERACTIONS

The mixing of Singlet Triplet states depends on spin exchange (and dipolar) interactions. This can be understood by looking at Fig.8.1.1 describing the separation of the Singlet and Triplet state due to spin - spin interactions and due to magnetic fields. In the absence of any interactions the energy of the Singlet and Triplet states are

The effect of the spin
exchange interaction
is to split the singlet
and triplet states. In
addition the effect of
dipolar interaction is
to remove the energy
degeneracy among
the triplet sublevels

degenerated. The effect of the spin exchange interaction is to split these states by 2J. In addition the effect of dipolar interaction is to remove the energy of the $|T_{z,0}\rangle$ from the $|T_{x,0}\rangle$ and $|T_{y,0}\rangle$. Moreoven if an external magnetic field is applied the energies of the $|T_{z,+}\rangle$ and $|T_{z,-}\rangle$ are further splitted. The spin exhange interaction Hamiltonian

Figure 8.1.1: The effect of spin - spin interactions and the effect of the externally applied magnetic field on the energy structure of the RP. Although Spin exchange and Dipolar Interaction may inhibit Singlet Triplet mixing if they are too large, the application of a magnetic field may initiate again the coherent mixing proceedure.

is given by Eq.73. The term J determines the strength of the interaction. This parameter depends on the electronic properties of the the radical. Usually it is taken to have an exponential decay dependence on the inter-radical distance ($J = J_0 e^{-r/r_0}$)[1]. It is thus possible that if the spin exchange and dipolar interactions are too large the coherent Singlet Triplet mixing procedure will be blocked. Nevertheless it is possible that the application of a magnetic field can counterbalance the effect of spin - spin interactions and thus to allow the Singlet Triplet mixing to initiate. In order for the RP to act as magneto-receptors the energy split shown in Fig.8.1.1 much be of specific size in order for the Zeeman effect to counter balance it. As stated in [12] it is difficult for this requirement to hold and other possibilities should be considered.

8.2 MUTUAL CANCELLATION OF SPIN EXCHANGE AND DIPOLAR INTERACTION

Mutual cancellation
of the Dipolar &
Spin Exchange
interaction allows
Singlet Triplet
oscillations

A possible solution for the blocking of Singlet Triplet interconversion was suggest by Efimova and Hore [12]. In their study these author noted that spin exchange and dipolar interaction may have similar amplitudes but opposite signs. This could cause these interactions to counterbalance each other. Even if the cancellation is not exact the presence of a magnetic field, such as the geomagnetic field could bring the Singlet and one of the Triplet states on the same energy level and the RP could evolve as in the absence of spin exchange and dipolar interactions.

8.3 THE BENEFITS OF THE QUANTUM ZENO EFFECTS IN THE AVIAN COMPASS

Mutual cancellation is possible and Nature may have developed such a mechanism . One the other hand the strength of spin exchange and dipolar interaction depend

---

1 the Dipolar interaction is inversely proporional to the inter-radical distance

sensitively on parameters such as the inter-radical distance and this fact makes this assumptions questionable. Moreover simulations done in this study were based on the TME which as already discussed is known to mask the quantum mechanical effects of the RP dynamics. In this section we will propose another mechanism which is independent of molecular paremeters and thus renders the avian compass a robust sensor. Additionally the proposed mechanism is valid independently on which ME is used, the results are qualitatively the same in all theories used, and only quantitative differences exist. We will show that when the quantum Zeno effect is manifested (i.e. when the recombination rates are asymmetric), the reaction's magnetic and angular sensitivity is practically independent of the presence or not of exchange and dipolar interactions. This suggestion means that a quantum effect such as the Quantum Zeno Effect renders the biological sensor insensitive to molecular parameters such as inter-molecular distance, electronic structure and the inter-molecular medium which affect the spin exchange and dipolar interaction.

8.3.1 *Toy system under study*

The time evolution of the RP and the recombination process is governed by the ME of the form

$$\frac{d\rho}{dt} = -i\,[H,\rho] - \mathcal{L}\,[\rho]$$

H is the Hamiltonian describing the unitary evolution of the two unpaired electrons and the second term $\mathcal{L}$ denotes a super-operator that takes into account the reaction dynamics. It is in this last term that all the proposed theories differ. The basic parameters that determine the reaction dynamics are the recombination rates k_S and k_T. The Hamiltonian comprises of three terms.

$$H = H_Z + H_{HFC} + H_{SE}$$

the Zeeman interaction of the two unpaired electrons with the external magnetic field (H_Z, Eq.71), the hyperfine couplings of the electron with the surrounding nuclear spins (H_{HFC}, Eq.67) and the finally the spin exchange interaction (H_{EX}, Eq.73). In the following we are going to consider the simplest physically realizable RP. It will contain only one nucleous of spin $1/2$ at the site of the one unpaired electron and the other electron will not be surrounded by nuclear spins (in this case the dimensions of all the operators of the ME will be $\dim\,[\mathcal{O}] = 8$). Hence the Hamiltonian for the hyperfine interaction will be simplified to give

$$H_{HFC} = (\mathbf{I} \cdot \alpha \cdot \mathbf{S_1})$$

as usual α is the hyperfine coupling tensor of the single nuclear spin $\mathbf{I}$ with the unpaired electron of e.g the Donor. In the simplest case the hyperfine tensor α is diagonal with only one non zero component. For out model $\alpha_{xx} = \alpha \neq 0$ and $\alpha_{yy} = \alpha_{zz} = 0$. This assumption provides for the angular sensitivity of the avian compass, i.e the sensor can distinguish the direction of the external field. Due to the form of the hyperfine interaction the hyperfine coupling Hamiltonian is further simplified to

$$H_{HFC} = (\alpha I_x \cdot S_{1,x})$$

The simplification of considering just one nuclear spin is common in all such considerations, and although it does not exhaust all the richness of phenomena that can be observed by the realistic inclusion of more nuclear spins (as is the case in Nature), it does provide an idea of what is in principle feasible, and this is exactly the goal of this work. The form of the spin exchange Hamilotnian is given by Eq.73 but it can be simplified in order to omit the constant term $J/2$ and thus can be written in the form

$$H_{EX} = 2J\mathbf{S_1} \cdot \mathbf{S_2}$$

Finally the Zeeman term of the Hamiltonian will have two different forms depending on which case is studied. For the study of magnetic sensitivity the magnetic field is

assumed to be along the z-axis and the gyromagnetic ratios of the two electrons are assumed to be equal. Then the Hamiltonian will be

$$H_{Z,MAG} = \omega \cdot (S_{1,z} + S_{2,z}) \tag{97}$$

where $\omega = \gamma B$ and γ is the gyromagnetic ratio $\gamma = 2\pi\, 2.8\,\text{MHz/G}$. For the study of the angular sensitivity we take the magnetic field, again of magnitude B, to be in the x-y plane, hence the Zeeman interaction term will be[2]

$$H_{Z,ANG} = \omega \cos\phi\,(S_{1,x} + S_{2,x}) + \omega \sin\phi\,(S_{1,y} + S_{2,y}) \tag{98}$$

For the study of the magnetic sensitivity we vary B, whereas for studying angular sensitivity we keep B constant and vary the angle φ.

8.3.2 *Magnetic Sensitivity*

The sensitivity of the sensor is defined as the smallest change in the detected signal that can be discriminate. If the sensor measures the quantity Q and the parameter P of the system is changed, then the sensitivity of the system to the parameter P is defined as

$$\delta P = \delta Q \left(\frac{dQ}{dP}\right)^{-1} \tag{99}$$

A magnetic sensor, such as the RP responsible for the orientation and navigation of avians, is characterized by the magnetic sensitivity, that is the smallest change in the amplitude of the magnetic field it can detect. It is obvious that the smaller the detectable change is, the more accurate the sensor will be. In the case of RP reactions the measured quantity is always the reaction's product yields (singlet or triplet). Since the reaction strongly depends on the magnitude (and the orientation) of the magnetic fields, a change in the amplitude of the field would cause a change in the measured yields. Thus the magnetic sensitivity is defined as

$$\delta B = \delta Y_T \left(\frac{dY_T}{dB}\right)^{-1}_{B=0.5G} \tag{100}$$

and depends on δY_T which is the smallest detectable change in the Triplet Yield. The value of the parameter δY_T should be known or at least should be estimated in order to determine the magnetic sensitivity δB. Obviously δY_T depends on the particular realization of the biochemical mechanism transducing the RP reaction yield to a physiological signal. On rather general grounds it has been shown [59] that δY_T is connected to N_R, the number of neuronal receptors sensitive to the radical-ion-pair reaction product molecules, by $(\delta Y_T)^2 = 4/N_R$. We choose $N_R = 1.6 \times 10^7$, in order to set δY_T at the value $\delta Y_T = 0.05\%$. The chosen value of N_R and hence δY_T is realistic and has the consequence that it sets the magnetic sensitivity at zero exchange coupling at the value of $\delta B = 0.01G$, i.e. at 2% of earth's field. This level of magnetic sensitivity is understood [61] to be actually realized in several avian species. It is stressed, however, that the following considerations are qualitatively independent of the particular value of δY_T, which just sets the absolute scale of the derived magnetic and angular sensitivity.

In Fig.8.3.1 we plot the an example of the Triplet yield as a function of the magnetic field calculated form Eq.88 for two different values of the spin exchange interaction. The magnetic sensitivity δB is proportional to the slope of Y_T vs B calculated at B = 0.5G From plots like the one shown in Fig.8.3.1 for many different values of the spin exchange coupling J we can obtain the sensitivity δB according to Eq.100. We did this calculation for two different parameter regimes for the recombination rates:

---

2 In both expressions for the Zeeman interaction the Larmor frequencies for the electronic spins were considered equal. This is a reasonable assumption since small differences in the $g-$factors would not produce detectable changes in the Larmor frequencies at geomagnetic field strengths.
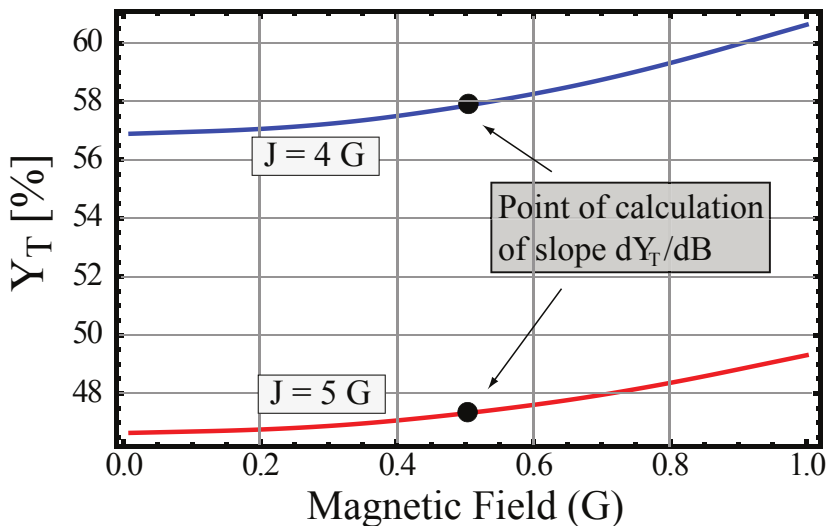
Figure 8.3.1: The magnetic sensitivity of the triplet reaction yield is proportional of the slope of Y_T vs B. In this figure the triplet yield as a function of the magnetic field is shown for two different values of spin exchange coupling J. The calculations were done for $k_S = 0.5\,\text{MHz}$, $k_T = 40\,\text{MHz}$, hyperfine coupling $\alpha = 1.75\,\text{G}$.

- equal recombination rates $k_S = k_T$ for both recombination channels. This regime will be called "Traditional Regime" from now on and it is the regime widely used so far and also considered in [12].

- asymmetric recombination rates and especially $k_S \ll k_T$. This one is the "Quantum Zeno" regime and k_T is larger or on the same order of the hyperfine coupling α. To elaborate on this, we note that if the initial state of the molecule is the singlet (which is usually the case) and there exist asymmetric recombination rates then the spin state of the radical-pair is strongly projected to the singlet state by the triplet reservoir.

In Fig.8.3.2 the result of the simulation is shown It is clearly seen that in the traditional regime the magnetic precision plunges to $\delta B = 0.5G$ already at $J = 6G$,. In contrast, in the quantum Zeno regime the magnetic sensitivity is $\delta B = 0.04G$ i.e one order of magnitude smaller than geomagnetic field. As noted before, all three theories produce qualitatively similar results.

In the "Quantum Zeno" regime δB is on the order of the geomagnetic field. Contrary in the "Traditional" regime the sensor is totally disoriented.
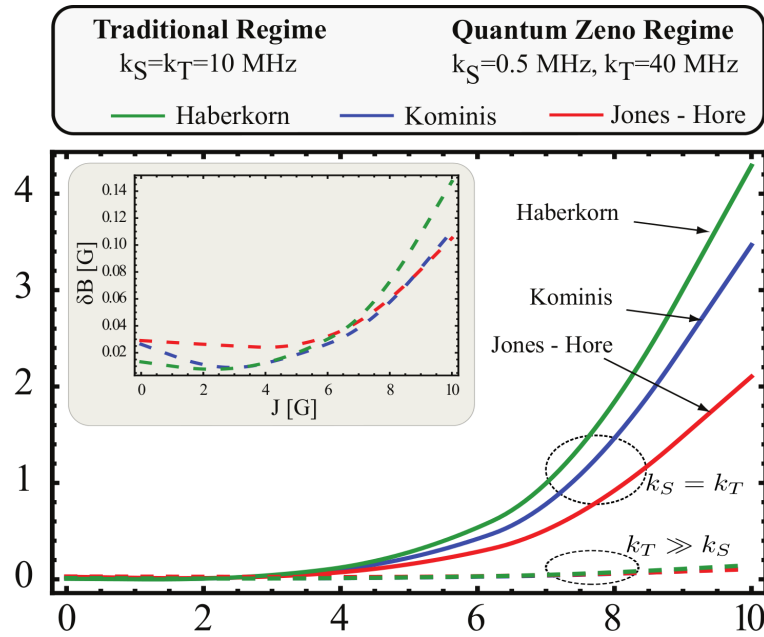
8.3.3 *Angular Sensitivity*

Besides the sensitivity to the changes of the amplitude of the magnetic fields, the sensor should be sensitive to the changes of the direction of the magnetic field vector. The angular sensitivity i.e the smallest rotation angle of the magnetic field vector producing a detectable change in the product yield is defined as

$$\delta\phi = \delta Y_T \left(\frac{dY_T}{d\phi} \right)^{-1}_{B=0.5G} = \delta Y_T \left(\frac{\Delta\phi}{Y_{T,max} - Y_{T,min}} \right) \tag{101}$$

$\delta\phi$ is the smallest change in the magnetic field's direction that produces a detectable change in the yield

$Y_{T,max}$ and $Y_{T,min}$ are the maximum and minimum values of the yield $Y_T(\varphi)$ and $\Delta\varphi = 90°$ is the angular width of the full swing between $Y_{T,max}$ and $Y_{T,min}$. In accordance with magnetic sensitivity, δY_T was chosen to be 0.05%, i.e setting the magnetic sensitivity to be at a level of 2% of the geomagnetic field in the absence of spin exchange interaction. $\delta\varphi$ represents the error in the chosen navigation path and alternative is called heading error. A typical plot of the Triplet Yield as a function of the fields angle is shown in Fig.8.3.3 Once more in order to calculate the dependence

Figure 8.3.2: Magnetic sensitivity of the reaction as a function of the exchange coupling J for the two different regimes of (i) equal recombination rates (solid lines) and (ii) asymmetric recombination rates (dashed lines) and for all three theories. Inset zooms into low δB values in order to make the predictions of all three theories in regime (ii) distinguishable. For all calculations $k_S = k_T = 10\,\mathrm{MHz}$ for the traditional regime, $k_S = 0.5\,\mathrm{MHz}$ and $k_T = 40\,\mathrm{MHz}$, for the Zeno regime and $\alpha = 1.75\,\mathrm{G}$. For the angular sensitivity calculation the magnitude of the magnetic field was $B = 0.5\,\mathrm{G}$. It is obvious that both the magnetic and the angular sensitivity depend on J much less sensitively in regime (ii), where the strong projective measurement induced by a large k_S (quantum Zeno effect) dominates the dynamics.

of the heading error from the spin exchange coupling we consider two parameter regimes for the recombination rates: the traditional regime ($k_S = k_T$) and the quantum Zeno regime ($k_S \ll k_T$). In Fig.8.3.4 the angular sensitivity of the avian compass *that the angular* as a function of the exchange coupling is depicted. It is clearly shown that the an- *sensitivity drops* gular sensitivity drops (i.e $\delta\varphi$ is increased) dramatically in the traditional regime, *dramatically in the* when the exchange interaction J is increased. Particularly at the value $J = 6\,\mathrm{G}$ the *traditional regime,* avian is totally disoriented. Contrary to the traditional regime, in the quantum Zeno *when the exchange* regime, the heading error remains in the level of the experimental observations, that *interaction J is* is $\delta\varphi = 40°$ at the highest value of J. *increased*

8.3.4 *Explanation of the Effect*

The evolution of the un-recombined RPs is given by the ME

$$\frac{d\rho}{dt} = -i\left[H_{mag}, \rho\right] - \frac{k_S + k_T}{2}\left(Q_s^\dagger Q_S \rho + \rho Q_s^\dagger Q_S - 2Q_S \rho Q_s^\dagger\right) \tag{102}$$

The RPs that are still in the Singlet Triplet subspace are continuously subjected to quantum measurement proceedure. As is known from Quantum Information Theory the effect of a continuous measurement is the loss of coherence. In the specific case of RP reaction the continuous interrogation of the pairs state by the Singlet and Triplet reservoirs and the subsequent quantum jumps result in Singlet Triplet decoherence.
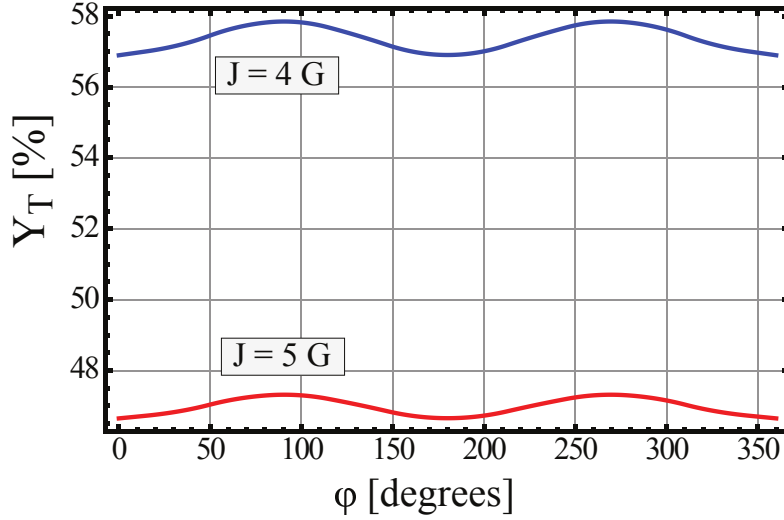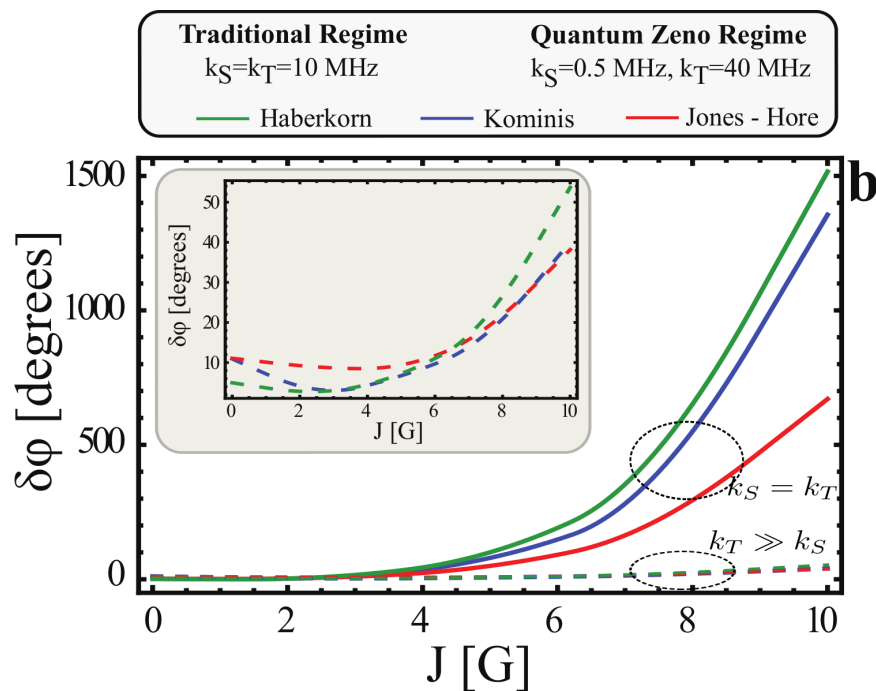
Figure 8.3.3: The angular sensitivity of the triplet reaction yield is proportional of the slope of Y_T vs φ. In this figure the triplet yield as a function of the magnetic field is shown for two different values of spin exchange coupling J. The calculations were done for $k_S = 0.5\,\text{MHz}$, $k_T = 40\,\text{MHz}$, hyperfine coupling $\alpha = 1.75\,\text{G}$.

A more detailed insight into the dynamics is gained by rewriting the previous ME in the form

$$\frac{d\tilde{\rho}}{dt} = \mathcal{M}\tilde{\rho} \qquad (103)$$

where $\tilde{\rho}$ is the column vector containing all the elements of ρ and $\mathcal{M}$ is a column matrix containing all the elements of the right part of Eq.102. The eigenvalues of the matrix $\mathcal{M}$ are of the form $m = -\lambda + i\Omega$ whith λ being the decay rate and Ω being the oscillation frequency. In the case of asymmetric recombination rates, i.e in the quantum Zeno regime some eigenvalues have decay rated that are proportional with the recombination rate ($\lambda_N \sim {}^{(k_S+k_T)}/_2$) and some other eigenvalues are inversely proportional to the recombination rate ($\lambda_{QZ} \sim {}^1/_{(k_S+k_T)/2}$). In the parameters' regime studied here, $k_S \ll k_T$ and thus $k = {}^{(k_S+k_T)}/_2 \simeq {}^{k_T}/_2$. It is well known known from Quantum Measurement theory [6] that the evolution of the of the of the quantum state due to unitary evolution caused by the Hamiltonian and due to the measurement procedure, which in our case is the measurement of Q_S at rate k is generated by the non-Hermitian operator $\mathcal{K} = H_{mag} - ikQ_S$. In the case that the spin exchange interaction is considered $\mathcal{K} = H_{mag}^{J=0} - i(k - iJ)Q_S$. Thus instead of including the exchange term in the Hamilotnian it is equivalent to replace $k \to k - iJ$. The eigenvalues m of the matrix $\mathcal{M}$ will be $m_N = -{}^{k_T}/_2 + i(\Omega - J)$ and for this eigenvalue the decay rate is still equal $\lambda_N = {}^{k_T}/_2$. The second set of eigenvalues will become $m_{QZ} = -1/(k_T - iJ) + i\Omega$. In this case the decay rate becomes $\lambda_{QZ} \sim k_T/(k_T^2 + J^2)$. It is thus obvious that when J is increased the decay rate decreases and hence the spin state evolution is slowed down. This argument is depicted in Fig.8.3.5 which shows the time evolution of the normalization of the density matrix, $Tr\{\rho\}$, i.e. the number of existing radical-ion pairs. The reaction is considered to be terminated when $Tr\{\rho\} = 5 \times 10^{-4}$, i.e. when the reaction yield is known to within δY_T. It is clearly seen that in the quantum Zeno regime, the reaction time depends on J in the way outlined before. On the contrary, when $k_S = k_T = k$, the change of $Tr\{\rho\}$ during the time interval dt is $dTr\{\rho\} = -dt(k_S\langle Q_S\rangle + k_T\langle Q_T\rangle) = -kdtTr\{\rho\}$, since $Q_S + Q_T = 1$. Hence the reaction time is proportional to $1/k$ and independent of J. The result is that during the short reaction time in the traditional regime, the triplet probability QT has not increased appreciably (Fig.8.3.6a), and the triplet yield is small, as shown in (Fig.8.3.6b). In contrast, in the quantum Zeno regime the reaction

*J decreases the decay rate and hence the spin state evolution is slowed down*

Figure 8.3.4: Angular sensitivity of the reaction as a function of the exchange coupling J for the two different regimes of (i) equal recombination rates (solid lines) and (ii) asymmetric recombination rates (dashed lines) and for all three theories. Inset zooms into low δB values in order to make the predictions of all three theories in regime (ii) distinguishable. For all calculations $k_S = k_T = 10\,\text{MHz}$ for the traditional regime, $k_S = 0.5\,\text{MHz}$ and $k_T = 40\,\text{MHz}$, for the Zeno regime and $\alpha = 1.75\,\text{G}$. For the angular sensitivity calculation the magnitude of the magnetic field was $B = 0.5\,\text{G}$. It is obvious that both the magnetic and the angular sensitivity depend on J much less sensitively in regime (ii), where the strong projective measurement induced by a large k_S (quantum Zeno effect) dominates the dynamics.

has enough time to "sample" large values of Q_T and lead to a triplet yield about an order of magnitude higher, hence the higher sensitivity in this regime. In other words, as seen in Fig.8.3.6b, the relative change $\delta Y_T / Y_T$ of the triplet yield with the magnetic field is roughly the same in both cases, but the absolute value of Y_T differs by a factor of 20, leading to respectively high slopes dY_T/dB and $dY_T/d\phi$. To summarize, the quantum measurement dynamics inherent in the recombination process of radical-ion pairs result in "delocalization" of the electron spin state at long times, as evidenced in Fig.8.3.6a. The asymmetric recombination rates result in the J-dependence of the reaction time. The interplay of these two effects provides for the robust magnetic and angular sensitivity in the presence of the exchange interaction

8.4 CONCLUSIONS

Coincidentally or not, it turns out [9] that the radical-ion pairs participating in the last stages of the electron-transfer processes taking place in bacterial photosynthetic reaction centers operate at the quantum Zeno regime, i.e. the triplet recombination rate k_T is about 20 times larger than k_S, the singlet recombination rate. It is noted that the manifestation of the quantum Zeno effect does not require any parameter fine tuning, but just the presence of asymmetric recombination rates. This regime seems to offer an operational advantage and hence the possibility that it is Nature's.

66
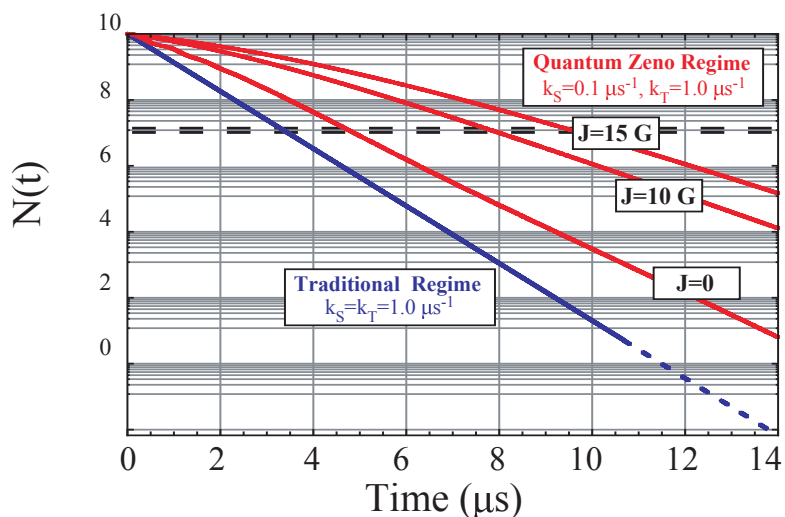
Figure 8.3.5: Time evolution of the normalization of ρ. The dashed line at $N = 5 \times 10^{-4}$ signifies the "termination" of the reaction, i.e. the point when the remaining radical-ion pairs are 0.05% of the initial number. It is seen that in the quantum Zeno regime, the reaction lasts longer for increasing J, as explained in the text. In contrast, in the traditional regime of equal recombination rates the duration of the reaction is independent of J.
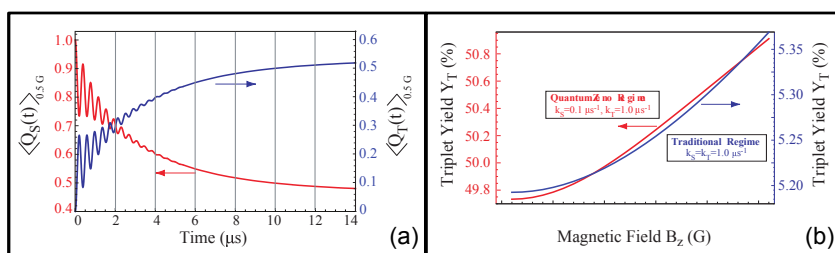
Figure 8.3.6: (a) Time evolution of the singlet and triplet probability, $\langle Q_S \rangle$ and $\langle Q_T \rangle$, respectively for the unrecombined radical-pairs, calculated for $B = 0.5$G and $J = 10$G. The measurement dynamics inherent in the charge recombination process of RPs "delocalize" the electron spin state at long times. (b) Triplet yield as a function of the magnetic field for $J = 10$G, plotted in the two regimes for the recombination rates.

In conclusion, we have identified a concrete biological process in which fundamental quantum effects have a profound effect on the system's performance, alluding to the possibility that this biological quantum sensor has evolved to a robust device by taking advantage of nontrivial aspects of quantum physics.

Part III

APPENDIX

APPENDIX OF PART I

A.1 RUBIDIUM ENERGY STRUCTURE

Hyperfine structure of ^{85}Rb and ^{87}Rb. The values of the energy splitting were taken from Steck [52, 53].

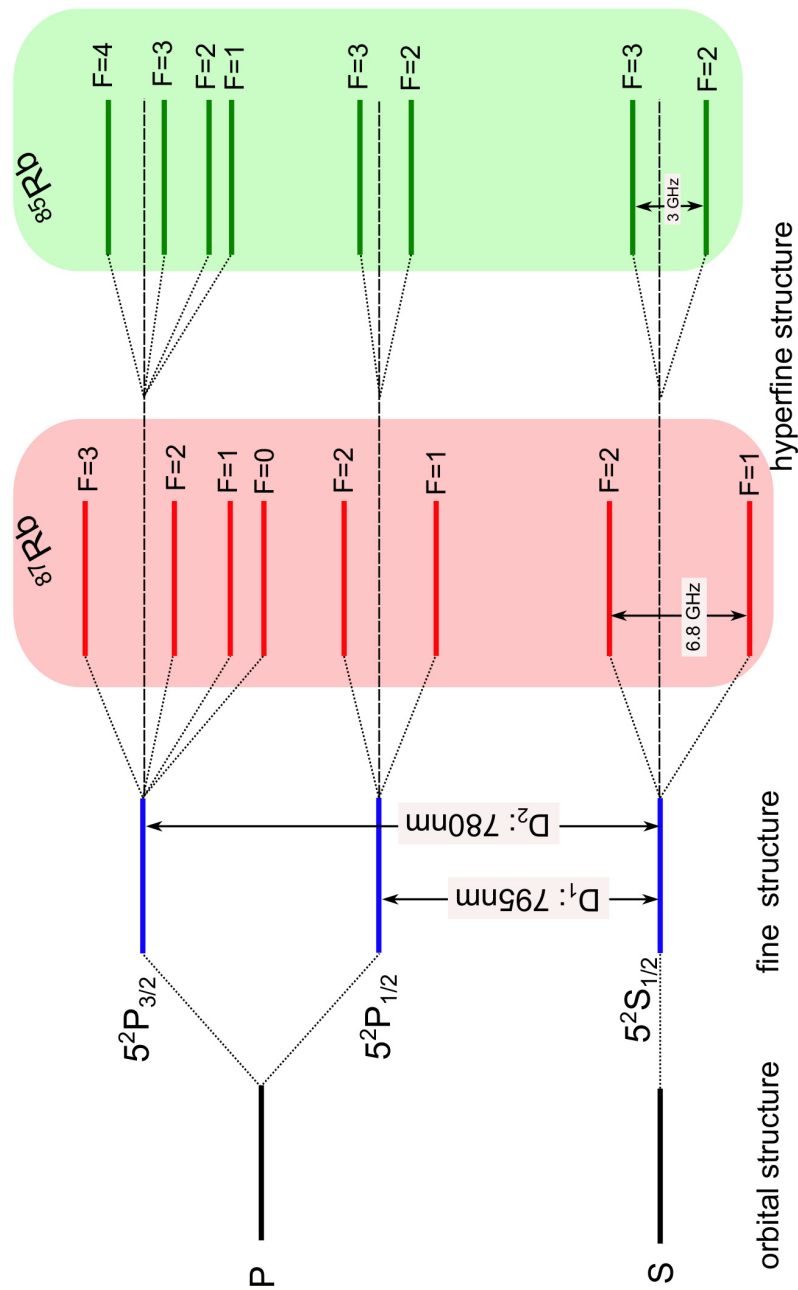Figure A.1.1: Energy structure of ^{85}Rb and ^{87}Rb.

Absorption profile of Rubidium atoms. For the red (dashed) trace rubidium atoms of natural abundance are contained in the same cell without adding buffer-gas. Due to the thermal motion of the atoms (Doppler broadening) closely spaced spectral lines arising from hyperfine structure are often not resolved. For the blue (solid) trace the atoms of both isotopes (at natural abundance) were also in the same cell, but contrary to the last case the cell was filled with 100 Torr of Nitrogen. This absorption spectrum was taken at $T = 50\,°C$. The rubidium atoms collide with the buffer gas atoms and the emission process is interrupted. The shortening of the emission process results ii increasing the energy uncertainty of the emitted photons.
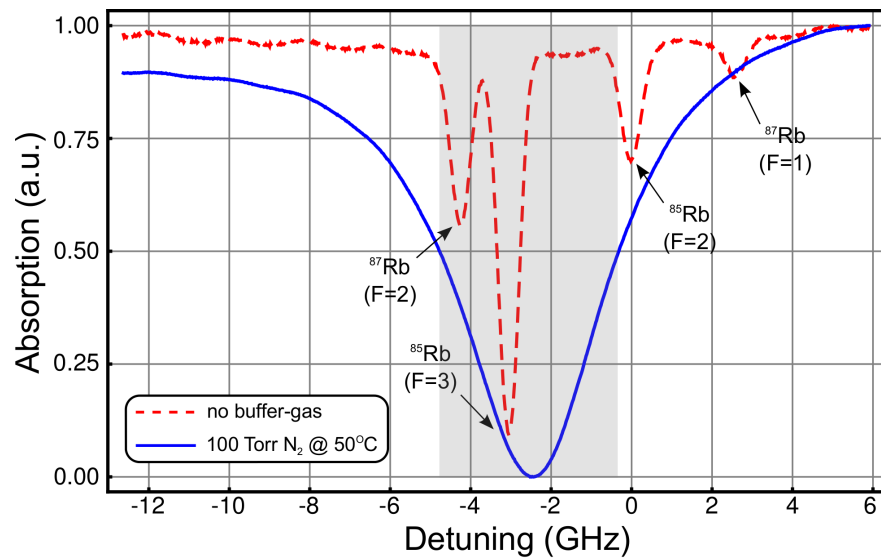
Figure A.2.1: D2 absorption profile of Rubidium atoms. Red (dashed) line is for Rb atoms at natural abundance, in the absence of buffer gas. Blue (solid) line is for Rb atoms at natural abundance in the presence of 100 Torr of Nitrogen.

In this appendix we will show the acquired power spectra after having subtracted the background signal from the Spin Noise Signal as discussed in Sec.5.2.
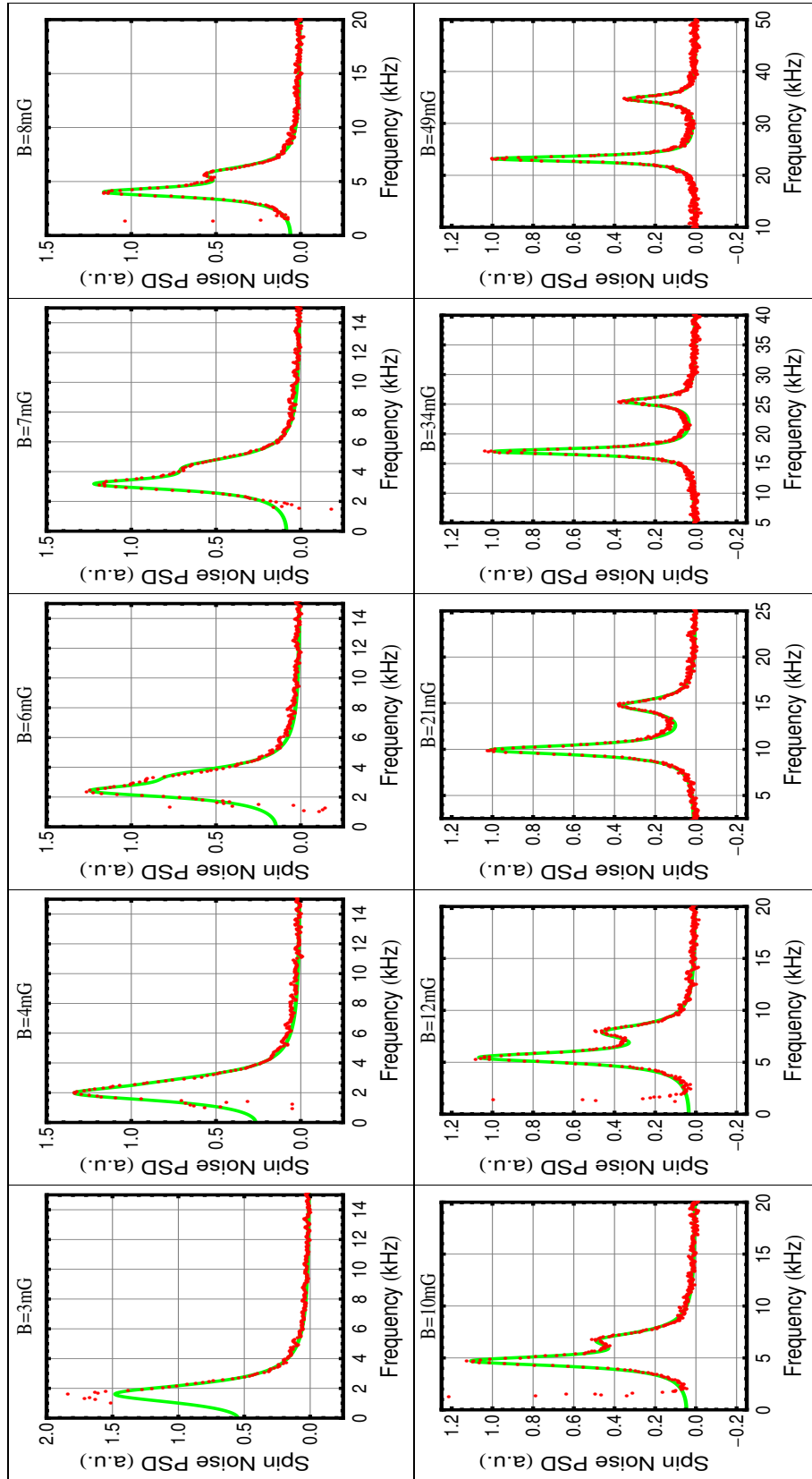
Figure A.3.1: One cell containing both Rb isotopes. 1st set of measurements
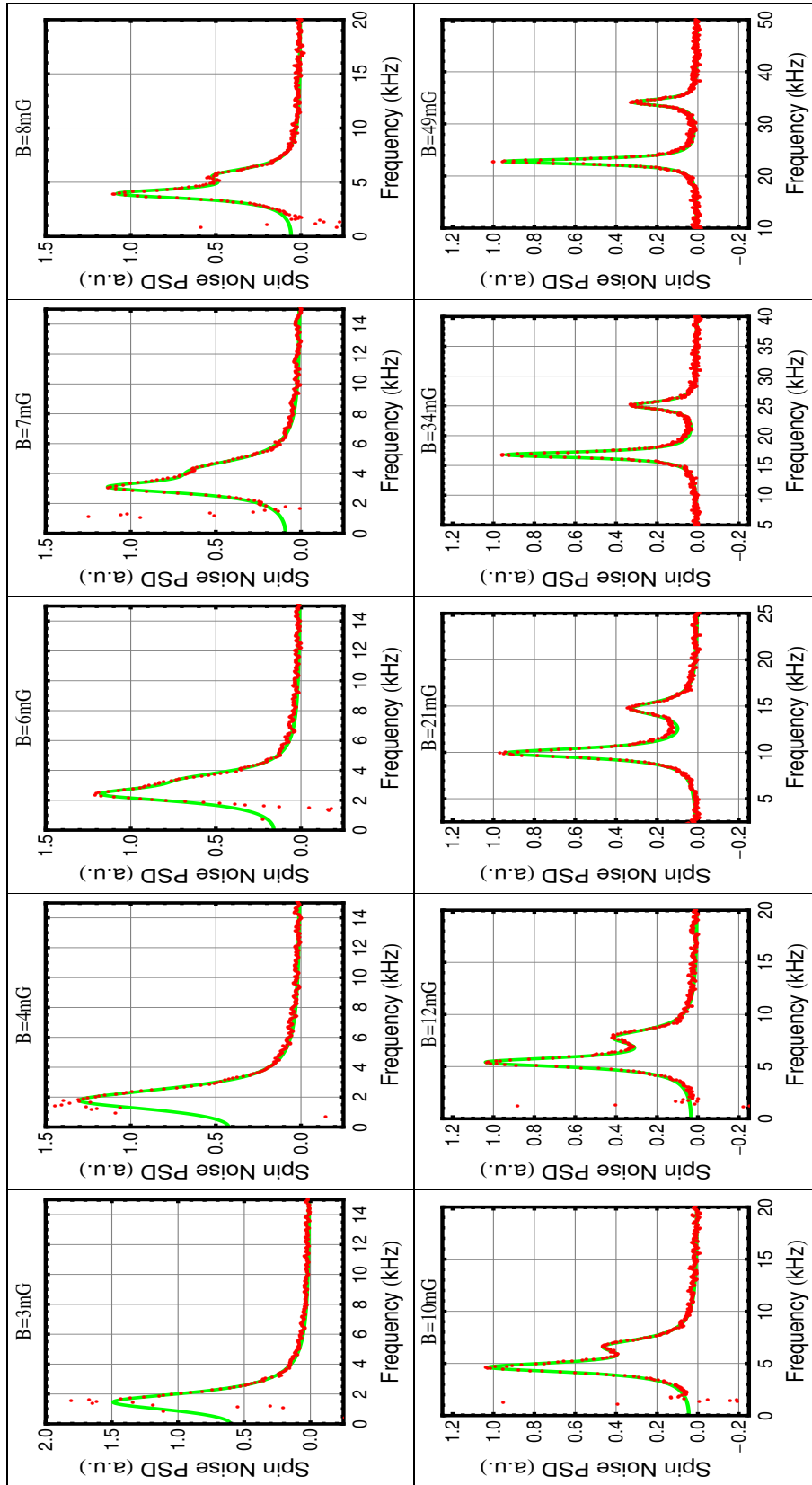
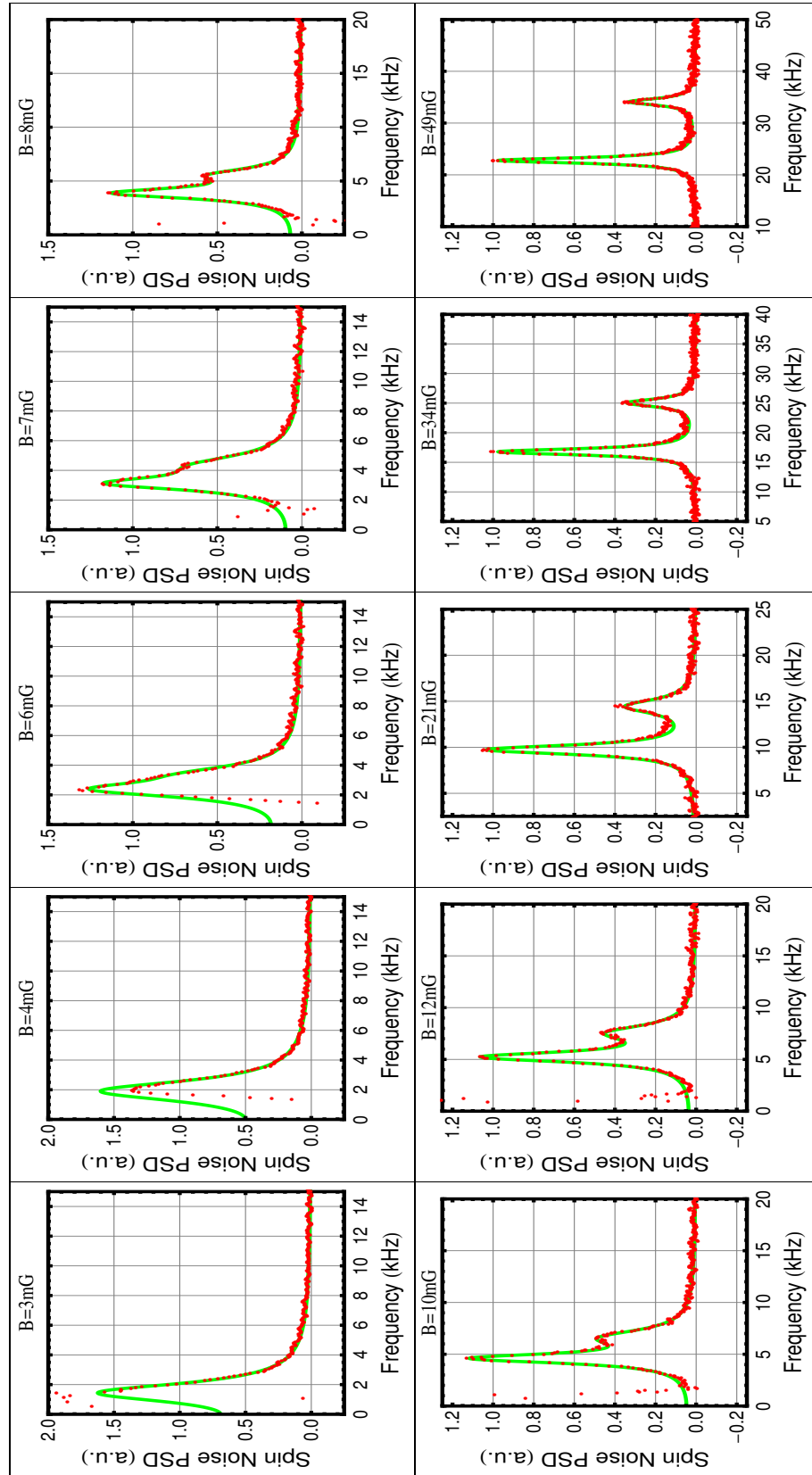**Figure A.3.2:** One cell containing both Rb isotopes. 2nd set of measurements

Figure A.3.3: One cell containing both Rb isotopes. 3rd set of measurements
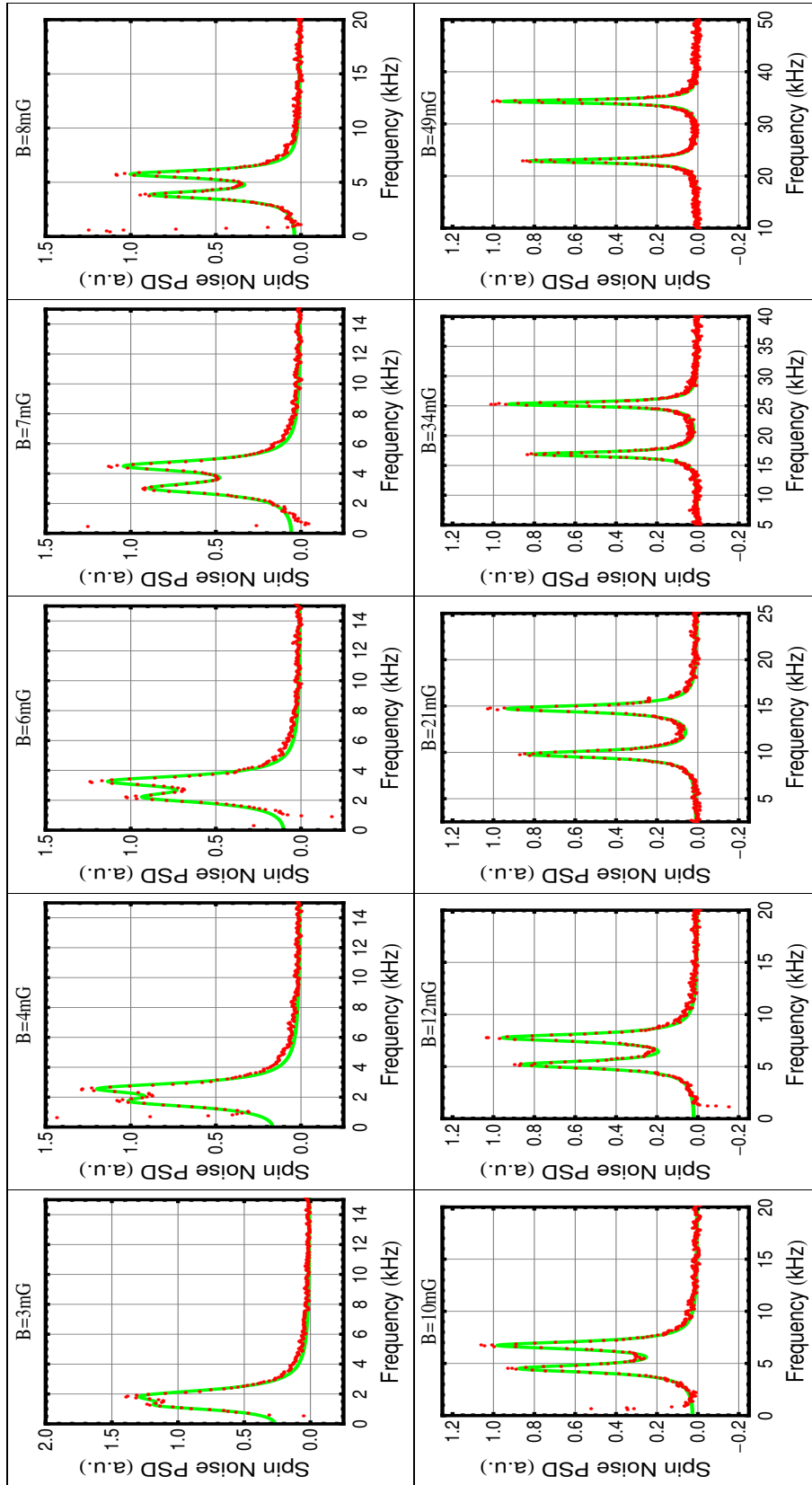
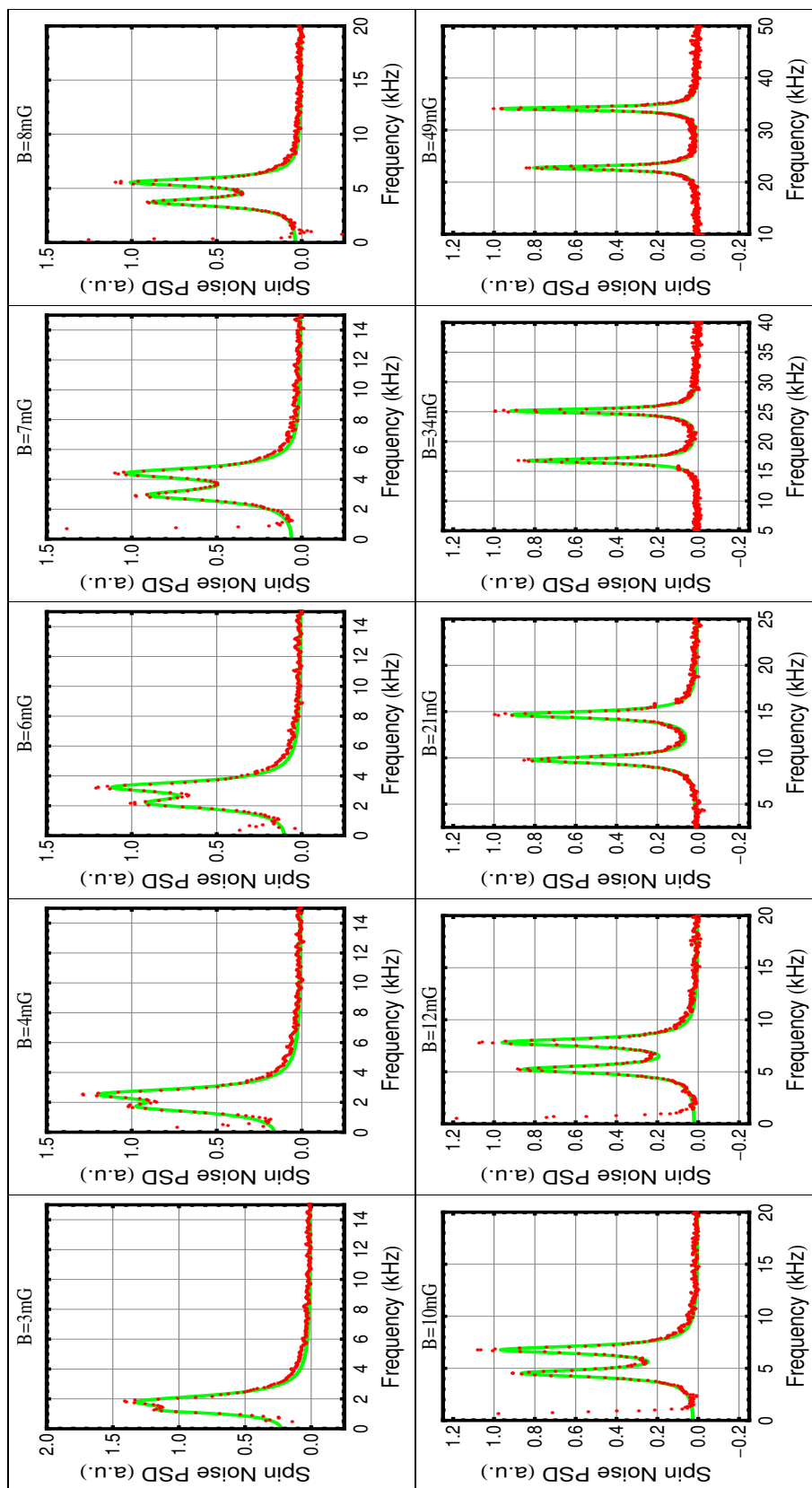**Figure A.3.4:** Each isotope is contained in a different cell. 1st set of measurements

77

Figure A.3.5: Each isotope is contained in a different cell. 1st set of measurements
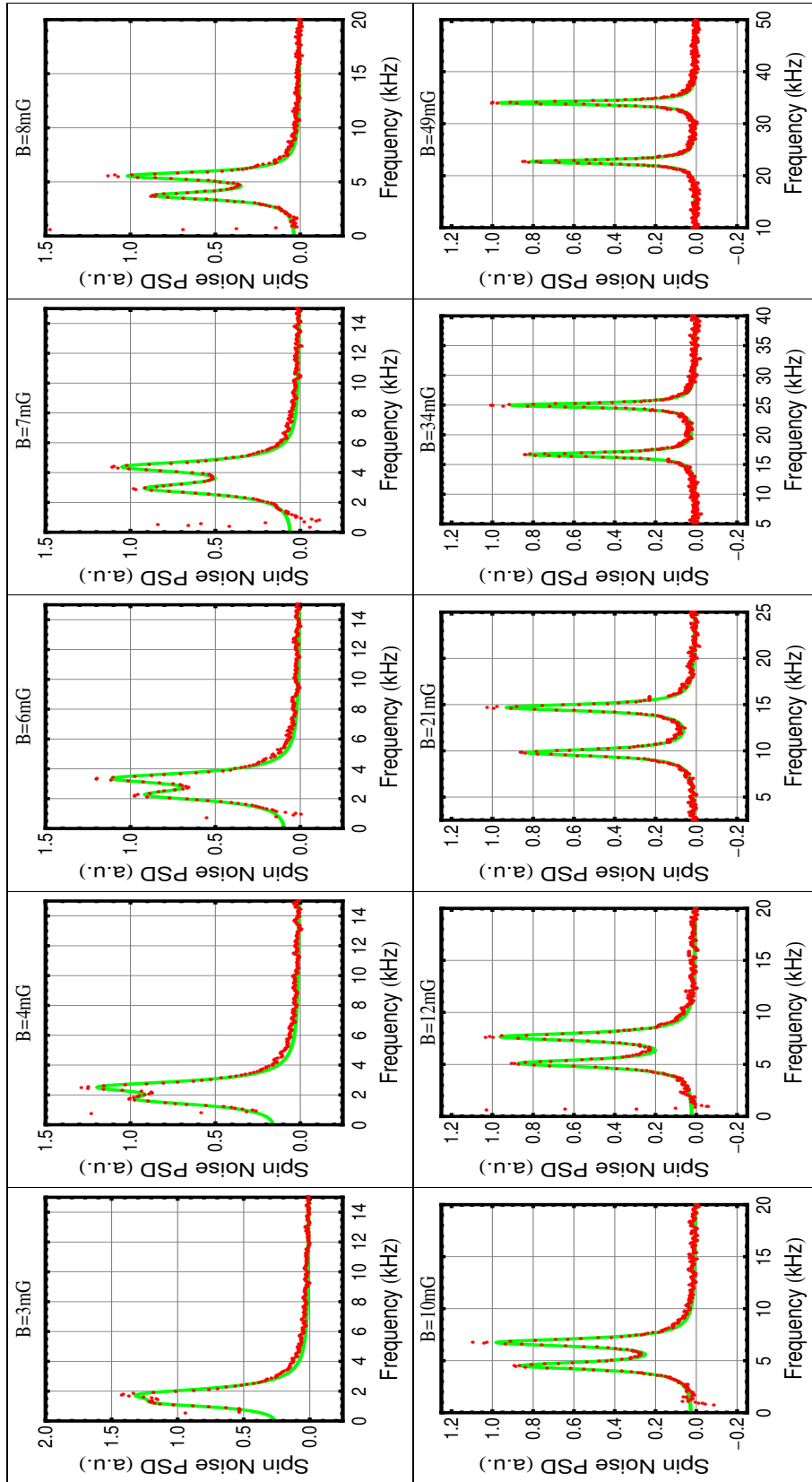
Figure A.3.6: Each isotope is contained in a different cell. 1st set of measurements

79

[1] J. Allred, R. Lyman, T. Kornack, and M. Romalis. High-Sensitivity Atomic Magnetometer Unaffected by Spin-Exchange Relaxation. *Physical Review Letters*, 89(13):130801, September 2002. ISSN 0031-9007. doi: 10.1103/PhysRevLett. 89.130801. URL http://link.aps.org/doi/10.1103/PhysRevLett.89.130801. (Cited on page 15.)

[2] S Appelt, A Ben-Amar Baranga, C J Erickson, M V Romalis, A R Young, and W Happer. Theory of spin-exchange optical pumping of ˆ{3}He and ˆ{129}Xe. *Physical Review A*, 58(2):1412–1439, August 1998. URL http://link.aps.org/doi/10.1103/PhysRevA.58.1412. (Cited on page 11.)

[3] A S Arnold, J S Wilson, and M G Boshier. A simple extended-cavity diode laser. *Review of Scientific Instruments*, 69(3):1236–1239, March 1998. URL http://dx.doi.org/10.1063/1.1148756. (Cited on page 19.)

[4] Dora Biro, Robin Freeman, Jessica Meade, Stephen Roberts, and Tim Guilford. Pigeons combine compass and landmark guidance in familiar route navigation. *Proceedings of the National Academy of Sciences of the United States of America*, 104(18):7471–6, May 2007. ISSN 0027-8424. doi: 10.1073/pnas. 0701575104. URL http://www.pubmedcentral.nih.gov/articlerender.fcgi?artid=1863466&tool=pmcentrez&rendertype=abstract. (Cited on page 41.)

[5] F. Bloch. Nuclear Induction. *Physical Review*, 70(7):460–474, 1946. (Cited on pages 3 and 11.)

[6] Vladimir B. Braginsky and Farid Ya Khalili. *Quantum Measurement*. Cambridge University Press, 1992. (Cited on page 65.)

[7] G Breit and I I Rabi. Measurement of Nuclear Spin. *Physical Review*, 38(11): 2082–2083, December 1931. URL http://link.aps.org/doi/10.1103/PhysRev.38.2082.2. (Cited on page 6.)

[8] S a Crooker, D G Rickel, a V Balatsky, and D L Smith. Spectroscopy of spontaneous spin noise as a probe of spin dynamics and magnetic resonance. *Nature*, 431(7004):49–52, September 2004. ISSN 1476-4687. doi: 10.1038/nature02804. URL http://www.ncbi.nlm.nih.gov/pubmed/15343328. (Cited on page 3.)

[9] Eugenio Daviso, Shipra Prakash, A Alia, Peter Gast, Johannes Neugebauer, Gunnar Jeschke, and Jörg Matysik. The electronic structure of the primary electron donor of reaction centers of purple bacteria at atomic resolution as observed by photo-CIDNP 13C NMR. *Proceedings of the National Academy of Sciences*, 106(52):22281–22286, December 2009. URL http://www.pnas.org/content/106/52/22281.abstract. (Cited on page 66.)

[10] A.T. Dellis. *Design and Development of Weak Magnetic Field and First Order Gradient Coils*. Senior, Crete, 2005. URL http://www.quantum-technology.gr/pdf_files/Senior_Thesis_Dellis.pdf. (Cited on page 22.)

[11] E A Donley, E Hodby, L Hollberg, and J Kitching. Demonstration of high-performance compact magnetic shields for chip-scale atomic devices. *Review of Scientific Instruments*, 78(8):83102–83107, August 2007. URL http://dx.doi.org/10.1063/1.2767533. (Cited on page 21.)

[12] Olga Efimova and P J Hore. Role of Exchange and Dipolar Interactions in the Radical Pair Model of the Avian Magnetic Compass. *Biophysical journal*, 94 (5):1565–1574, March 2008. URL http://linkinghub.elsevier.com/retrieve/pii/S0006349508705952. (Cited on pages 59, 60, and 63.)

[13] Crispin W Gardiner. *Stochastic Methods A Handbook for the Natural and Social Sciences*. Springer, Berlin, second edition, 2010. (Cited on page 11.)

[14] Crispin W Gardiner and Zoller Peter. *Quantum Noise: A Handbook of Markovian and Non-Markovian Quantum Stochastic Methods with Applications to Quantum Optics*. Springer, Berlin, third edition. (Cited on page 13.)

[15] F. Grossetete. Relaxation par collisions d'echange de spin. *J. Phys. France*, 25: 383 – 396, 1964. (Cited on page 9.)

[16] R. Haberkorn. Density matrix description of spin-selective radical pair reactions. *Molecular Physics*, 32(5):1491–1493, November 1976. ISSN 0026-8976. doi: 10.1080/00268977600102851. URL http://www.tandfonline.com/doi/abs/10.1080/00268977600102851. (Cited on page 46.)

[17] Jonathan T Hagstrum, U S Geological Survey, Menlo Park, and Middlefield Road. PERSPECTIVE INFRASOUND AND THE AVIAN NAVIGATIONAL MAP. *The Journal of Experimental Biology*, 203:1103–1111, 2000. (Cited on page 41.)

[18] W Happer and B S Mathur. Effective Operator Formalism in Optical Pumping. *Physical Review*, 163(1):12–25, November 1967. URL http://link.aps.org/doi/10.1103/PhysRev.163.12. (Cited on page 16.)

[19] W Happer and H Tang. Spin-Exchange Shift and Narrowing of Magnetic Resonance Lines in Optically Pumped Alkali Vapors. *Physical Review Letters*, 31(5): 273–276, July 1973. URL http://link.aps.org/doi/10.1103/PhysRevLett.31.273. (Cited on page 15.)

[20] William Happer. Optical Pumping. *REVIEWS OF MODERN PHYSICS*, 44(2), 1972. (Cited on pages 7 and 16.)

[21] William Happer, Yuan-Yu Jau, and Thad Walker. *Optically Pumped Atoms*. Willey-VCH, 2010. (Cited on page 16.)

[22] J E M Haverkort, H G C Werij, and J P Woerdman. Numerical study of light-induced drift of Na in noble gases. *Physical Review A*, 38(8):4054–4063, October 1988. URL http://link.aps.org/doi/10.1103/PhysRevA.38.4054. (Cited on page 8.)

[23] Ifan Hughes and Thomas Hase. *Uncertainties in single-variable*. Oxford University Press, 2010. (Cited on page 34.)

[24] Konstantin L. Ivanov, Marina V. Petrova, Nikita N. Lukzen, and Kiminori Maeda. Consistent Treatment of Spin-Selective Recombination of a Radical Pair Confirms the Haberkorn Approach. *The Journal of Physical Chemistry A*, 114(35): 9447–9455, 2010. doi: doi:10.1021/jp1048265. (Cited on pages 49, 51, and 52.)

[25] R C Johnson, R E Merrifield, P Avakian, and R B Flippen. Effects of Magnetic Fields on the Mutual Annihilation of Triplet Excitons in Molecular Crystals. *Physical Review Letters*, 19(6):285–287, August 1967. URL http://link.aps.org/doi/10.1103/PhysRevLett.19.285. (Cited on page 43.)

[26] J.a. Jones and P.J. Hore. Spin-selective reactions of radical pairs act as quantum measurements. *Chemical Physics Letters*, 488(1-3):90–93, March 2010. ISSN 00092614. doi: 10.1016/j.cplett.2010.01.063. URL http://linkinghub.elsevier.com/retrieve/pii/S000926141000120X. (Cited on pages 48 and 51.)

[27] J.A. Jones, Kiminori Maeda, U.E. Steiner, and P.J. Hore. Reply to Comment on Spin-selective reactions of radical pairs act as quantum measurements. *Chemical Physics Letters*, 508(1):184–185, May 2011. ISSN 00092614. doi: 10.1016/j.cplett.2011.04.022. URL http://dx.doi.org/10.1016/j.cplett.2011.04.022http://linkinghub.elsevier.com/retrieve/pii/S0009261411004167. (Cited on page 51.)

[28] G. Katsoprinakis, A.T. Dellis, and I. Kominis. Measurement of transverse spin-relaxation rates in a rubidium vapor by use of spin-noise spectroscopy. *Physical Review A*, 75(4):042502, April 2007. ISSN 1050-2947. doi: 10.1103/PhysRevA.75.042502. URL http://link.aps.org/doi/10.1103/PhysRevA.75.042502. (Cited on page 3.)

[29] G E Katsoprinakis. *Spin Noise , Decoherence and Magnetic effects in Alkali Atoms and Biomolecules*. PhD thesis, University of Crete, 2010. (Cited on page 23.)

[30] I K Kominis. Quantum Zeno effect explains magnetic-sensitive radical-ion-pair reactions. *Physical Review E*, 80(5):56115, November 2009. URL http://link.aps.org/doi/10.1103/PhysRevE.80.056115. (Cited on pages 47, 48, 51, and 56.)

[31] I K Kominis. Magnetic sensitivity and entanglement dynamics of the chemical compass. *Chemical Physics Letters*, 542(0):143–146, July 2012. ISSN 0009-2614. doi: http://dx.doi.org/10.1016/j.cplett.2012.06.014. URL http://www.sciencedirect.com/science/article/pii/S0009261412006847. (Cited on page 51.)

[32] I K Kominis, T W Kornack, J C Allred, and M V Romalis. A subfemtotesla multichannel atomic magnetometer. *Nature*, 422(6932):596–599, April 2003. ISSN 0028-0836. URL http://dx.doi.org/10.1038/nature01484. (Cited on page 15.)

[33] Iannis K Kominis. Radical-ion-pair reactions are the biochemical equivalent of the optical double-slit experiment. *Physical Review E*, 83(5):56118, May 2011. URL http://link.aps.org/doi/10.1103/PhysRevE.83.056118. (Cited on pages 47, 48, 51, and 56.)

[34] Iannis K Kominis. Comment on Spin-selective reactions of radical pairs act as quantum measurements. *Chemical Physics Letters*, 508(1):182–183, May 2011. ISSN 0009-2614. doi: http://dx.doi.org/10.1016/j.cplett.2011.04.026. URL http://www.sciencedirect.com/science/article/pii/S0009261411004209. (Cited on pages 51 and 56.)

[35] Gerd Kothe, Stefan Weber, Robert Bittl, Ernst Ohmes, Marion C Thurnauer, and James R Norris. Transient EPR of light induced radical pairs in plant photosystem I observation of quantum beats. *Chemical Physics Letters*, 186 (6):474–480, November 1991. ISSN 0009-2614. doi: http://dx.doi.org/10.1016/0009-2614(91)90454-H. URL http://www.sciencedirect.com/science/article/pii/000926149190454H. (Cited on page 56.)

[36] Kiminori Maeda, Christopher J Wedge, Jonathan G Storey, Kevin B Henbest, Paul A Liddell, Gerdenis Kodis, Devens Gust, P J Hore, and Christiane R Timmel. Spin-selective recombination kinetics of a model chemical magnetoreceptor. *Chemical Communications*, 47(23):6563–6565, 2011. ISSN 1359-7345. doi: 10.1039/C1CC11625H. URL http://dx.doi.org/10.1039/C1CC11625H. (Cited on page 56.)

[37] Yu. N. Molin. Quantum Beats in Recombination of Spin correlated Radical Pairs. *Bull. Korean Chem. Soc*, 20:6, 1999. (Cited on page 56.)

[38] Rachel Muheim, John B Phillips, and Susanne Akesson. Polarized light cues underlie compass calibration in migratory songbirds. *Science (New York, N.Y.)*,

313(5788):837–9, August 2006. ISSN 1095-9203. doi: 10.1126/science.1129709. URL http://www.ncbi.nlm.nih.gov/pubmed/16902138. (Cited on page 41.)

[39] Georg M Müller, Michael Oestreich, Michael Römer, and Jens Hübner. Semiconductor spin noise spectroscopy: Fundamentals, accomplishments, and challenges. *Physica E: Low-dimensional Systems and Nanostructures*, 43(2):569–587, December 2010. ISSN 1386-9477. doi: http://dx.doi.org/10.1016/j.physe.2010.08.010. URL http://www.sciencedirect.com/science/article/pii/S1386947710004716. (Cited on page 3.)

[40] Norbert Müller and Alexej Jerschow. Nuclear spin noise imaging. *Proceedings of the National Academy of Sciences of the United States of America*, 103(18):6790–2, May 2006. ISSN 0027-8424. doi: 10.1073/pnas.0601743103. URL http://www.ncbi.nlm.nih.gov/pubmed/20886922. (Cited on page 3.)

[41] U Munro, J A Munro, J B Phillips, F B Biologie, and J W Goethe Universita. Evidence for a Magnetite-Based Navigational Map in Birds. *Naturwissenschaften*, 84:26–28, 1997. (Cited on page 41.)

[42] P.A. Purtov. To the theory of Zeno chemical effect The exactly solvable model. *Chemical Physics Letters*, 496:335–338, 2010. URL http://www.sciencedirect.com/science/article/pii/S0009261410009231. (Cited on pages 49, 51, and 52.)

[43] Norman F Ramsey. A Molecular Beam Resonance Method with Separated Oscillating Fields. *Physical Review*, 78(6):695–699, June 1950. URL http://link.aps.org/doi/10.1103/PhysRev.78.695. (Cited on page 5.)

[44] T Ritz, S Adem, and K Schulten. A model for photoreceptor-based magnetoreception in birds. *Biophysical journal*, 78(2):707–18, February 2000. ISSN 0006-3495. doi: 10.1016/S0006-3495(00)76629-X. URL http://www.pubmedcentral.nih.gov/articlerender.fcgi?artid=1300674&tool=pmcentrez&rendertype=abstract. (Cited on page 59.)

[45] Christopher T Rodgers and P J Hore. Chemical magnetoreception in birds: the radical pair mechanism. *Proceedings of the National Academy of Sciences of the United States of America*, 106(2):353–60, January 2009. ISSN 1091-6490. doi: 10.1073/pnas.0711968106. URL http://www.pubmedcentral.nih.gov/articlerender.fcgi?artid=2626707&tool=pmcentrez&rendertype=abstract. (Cited on page 43.)

[46] C Schori, B Julsgaard, J L Sø rensen, and E S Polzik. Recording Quantum Properties of Light in a Long-Lived Atomic Spin State: TowardsQuantum Memory. *Physical Review Letters*, 89(5):57903, July 2002. URL http://link.aps.org/doi/10.1103/PhysRevLett.89.057903. (Cited on page 38.)

[47] K Schulten and P.G. Wolynes. Semiclasisical description of electron spin motion is radicals including the effect of electron hoping. *j chem phys*, 68(7):3292–3297, 1978. (Cited on pages 41 and 44.)

[48] Klaus Schulten and Robert Bittl. Probing the dynamics of a polymer with paramagnetic end groups by magnetic fields. *The Journal of Chemical Physics*, 84(9):5155, 1986. ISSN 00219606. doi: 10.1063/1.450668. URL http://link.aip.org/link/JCPSA6/v84/i9/p5155/s1&Agg=doi. (Cited on page 45.)

[49] A. I. Shushin. Effect of state-selective reactive decay on the evolution of quantum systems. *The Journal of Chemical Physics*, 133(4):044505, 2010. URL http://dx.doi.org/10.1063/1.3461133. (Cited on pages 48 and 51.)

[50] Tucho Sleator, Erwin L Hahn, Claude Hilbert, and John Clarke. Nuclear Spin Noise. *Physical review letters*, 55(1742-1745), 1985. doi: 10.1103/PhysRevLett.55.1742. URL http://prl.aps.org/abstract/PRL/v55/i17/p1742_1. (Cited on page 3.)

[51] T J Sumner Smith, J M Pendlebury, and K F. Convectional magnetic shielding. *Journal of Physics D: Applied Physics*, 20(9):1095, 1987. ISSN 0022-3727. URL http://stacks.iop.org/0022-3727/20/i=9/a=001. (Cited on pages 21 and 22.)

[52] Daniel Adam Steck. Rubidium 85 D Line Data Author contact information :, . URL http://steck.us/alkalidata/rubidium85numbers.pdf. (Cited on page 71.)

[53] Daniel Adam Steck. Rubidium 87 D Line Data Author contact information :, . URL http://steck.us/alkalidata/rubidium87numbers.pdf. (Cited on page 71.)

[54] B van Dijk, J K H Carpenter, A J Hoff, and P J Hore. Magnetic Field Effects on the Recombination Kinetics of Radical Pairs. *The Journal of Physical Chemistry B*, 102(2):464–472, January 1998. ISSN 1520-6106. doi: 10.1021/jp9721816. URL http://dx.doi.org/10.1021/jp9721816. (Cited on page 56.)

[55] Georgios Vasilakis. *Precision measurements of spin interactions with high density atomic vapors*. PhD thesis, Preinceton, 2011. (Cited on pages 16 and 17.)

[56] Von Middendorf A. Die Isepipetsen Russlands, Grundlagen zur Erforschung der Zugzeiten und Zugrichtungen der Vogel. *Russlands. Mem. Acad. Sci. St. Petersbourg*, 8:1–143, 1859. (Cited on page 41.)

[57] Thad G Walker and William Happer. Spin-exchange optical pumping of noble-gas nuclei. *Reviews of Modern Physics*, 69(2):629–642, April 1997. URL http://link.aps.org/doi/10.1103/RevModPhys.69.629. (Cited on page 9.)

[58] Hans G Wallraff. Avian olfactory navigation : its empirical foundation and conceptual state. *Animal Behaviour*, 62(2):189–204, 2004. doi: 10.1016/j.anbehav.2003.06.007. (Cited on page 41.)

[59] James C Weaver, Timothy E Vaughan, and R Dean Astumian. Biological sensing of small field differences by magnetically sensitive chemical reactions. *Nature*, 405(6787):707–709, June 2000. ISSN 0028-0836. URL http://dx.doi.org/10.1038/35015128. (Cited on page 62.)

[60] Carl E. Wieman and Leo Hollberg. Using diode lasers for atomic physics. *Review of Scientific Instruments*, 62(1), 1991. doi: http://link.aip.org/link/doi/10.1063/1.1142305. (Cited on page 19.)

[61] W. Wiltschko and R. Wiltschko. Migratory orientation of European Robins is affected by the wavelength of light as well as by a magnetic pulse. *Journal of Comparative Physiology A*, 177(3):363–369, September 1995. ISSN 0340-7594. doi: 10.1007/BF00192425. URL http://link.springer.com/10.1007/BF00192425. (Cited on page 62.)

[62] V. S. Zapasskii. HIGHLY SENSITIVE POLARIMETRIC TECHNIQUES. *Zhurnal Prikladnoi Spektroskopii*, 37(2):188–196, 1983. (Cited on page 3.)

[63] V. S. Zapasskii, a. Greilich, S. a. Crooker, Yan Li, G. G. Kozlov, D. R. Yakovlev, D. Reuter, a. D. Wieck, and M. Bayer. Optical Spectroscopy of Spin Noise. *Physical Review Letters*, 110(17):176601, April 2013. ISSN 0031-9007. doi: 10.1103/PhysRevLett.110.176601. URL http://link.aps.org/doi/10.1103/PhysRevLett.110.176601. (Cited on page 3.)